Università degli Studi di Roma “Tor Vergata”
Università degli Studi di Roma “La Sapienza”
Universidad de La Laguna

DEPARTMENT OF PHYSICS

PhD in Astronomy, Astrophysics and Space Sciences
Cycle XXVIII

The star formation history in the Local Group

Supervisors:
Prof. Roberto Buonanno
Prof. Antonio Aparicio
Coordinators:
Prof. Roberto Capuzzo Dolcetta
Prof. Pasquale Mazzotta

PhD Candidate:
Federica Fusco

Contents

Abstract

In this thesis, I focused on the study of the dwarf galaxies in the Local Group (LG). Since they can be resolved into stars, this group of galaxies offers a perfect laboratory in addressing the problems still open in galaxy formation and evolution. In addition, the LG is composed of a unique mixture of all the morphological types of dwarfs, namely dwarf irregulars (dIrr), spheroidals (dSph), and the recently discovered ultra faints (UFD). The star formation histories (SFH) of these systems are fundamental to obtain deeper insights into their stellar populations, and especially on the presence of radial gradients.

The sample of galaxies analysed in the present study is composed of a dIrr, two dSphs, and a UFD. These are NGC 6822, Draco, Ursa Minor (UMi), and Hercules, respectively.

In all the cases the photometry was obtained using DAOPHOT/ ALLSTAR/ ALLFRAME (Stetson 1987, 1994), which resulted in the derivation of very accurate colour-magnitude diagrams (CMD). The study of NGC 6822 is based on HST data, whereas in all the other cases Subaru data have been used. In addition, in the case of NGC 6822 and Draco the accurate star formation history was derived using the IAC method composed of IAC-star/ IAC-pop/ MinnIAC (Aparicio & Gallart 2004; Aparicio & Hidalgo 2009; Hidalgo et al. 2011).

The data sample of NGC 6822 is divided into six fields, which cover the whole bar of this dwarf galaxy. The SFH solutions we derived show an enhanced star formation rate (SFR) in Fields 1 and 3 during the past 500 Myr, whereas the SFRs in the other fields are almost extinguished at very recent

epochs. In addition, I studied the radial gradients of the populations by considering the total mass converted into stars in two time intervals (between 0 and 0.5 Gyr ago and between 0.5 and 13.5 Gyr ago). The scale lengths of the young and intermediate-to-old populations result perfectly compatible, with the exception of the young populations in Fields 1 and 3. The recent SFR in these two fields is greater than in the other ones. This might be an indication that in these two fields we are sampling incipient spiral arms. In addition, the age-metallicity relations were derived. As expected, the metallicity increases with time for all of the fields. No radial gradient in the metallicity is observed.

The data available for the dSph Draco are composed of five fields, which cover as far out as 3 core radii. The SFH of Draco is characterized by a unique burst which took place $\sim$ 12.9 Gyr ago, with a width of $\sim$ 0.5 Gyr. This is compatible with a quenching of the SF activity due to the effect of reionization, even though a signature in the spectroscopic measurement of the metallicity rises doubts about this interpretation. In addition, I studied the presence of radial gradients in Draco. I calculated the scale lengths of different evolutionary features of this galaxy. All the scale lengths are compatible, hence there is evidence that Draco is composed of a unique stellar population.

For UMi the SFH was not obtained, because of a significant difference between the predictions of the evolutionary models and the observed CMD. A real peculiarity in this galaxy is excluded if archival HST photometry is considered, since it agrees with the models. Hence I requested two additional sets of data, obtained with the IAC80 and NOT telescopes. The first dataset was used in order to verify the calibration equations obtained. The second one was used to investigate if a non linearity between the NOT and Subaru photometries was present. None of the two data sets were useful in solving the discrepancy, hence I performed a study of the populations in this galaxy based on star counts. In particular, I compared the width of the observed sub-giant branch with that predicted by stellar evolutionary models. This comparison sheds light on the duration of the SF burst in UMi, which results to be between 0.15 and 2 Gyr. Moreover, I investigated the radial gradients in this dSph. As in the previous cases I derived the scale lengths for different evolutionary features in this galaxy, which result compatible. Hence, UMi appears to be dominated by only one stellar population.

The photometry of Hercules resulted to be too shallow to derive the accurate SFH, therefore, I compared it to a set of GGC and isochrones belonging to the BaSTI library (Pietrinferni et al. 2004). This comparison discloses that this galaxy hosts a population of age ≥ 12 Gyr and of very low metal content.

Riassunto

La mia tesi è focalizzata sullo studio delle galassie nane del Gruppo Locale. Tale gruppo è un laboratorio perfetto dove studiare la formazione e l'evoluzione di questi sistemi, in quanto è composto da tutti i tipi morfologici noti di galassie nane. Le galassie nane possono essere divise in tre gruppi principali: le irregolari, le sferoidali e le estremamente deboli (Ultra Faint Dwarfs, UFD). Lo studio delle storie di formazione stellare (SFH) di queste galassie è fondamentale per avere informazioni sulle popolazioni stellari che le compongono.

Il campione di galassie studiato è composto da una galassia nana irregolare, NGC 6822, due nane sferoidali, Draco e Ursa Minor (UMi), e una UFD, Hercules.

Per tutte e quattro queste galassie ho eseguito la fotometria usando il programma DAOPHOT/ ALLSTAR/ ALLFRAME (Stetson 1987, 1994). In questo modo ho ottenuto i diagrammi colore-magnitudine (Colour Magnitude Diagram, CMD) per ognuna. I dati di NGC 6822 sono stati osservati con l'Hubble (Hubble Space Telescope, HST), mentre le altre tre galassie sono state osservate con il telescopio Subaru. Per NGC 6822 e Draco ho ottenuto la SFH usando lo specifico codice composto da IAC-star/ IAC-pop/ MinnIAC (Aparicio & Gallart 2004; Aparicio & Hidalgo 2009; Hidalgo et al. 2011).

I dati di NGC 6822 sono suddivisi in sei campi, che coprono la barra di questa galassia. La SFH è caratterizzata da un innalzamento del *rate* nei campi 1 e 3 negli ultimi 500 Myr, mentre in tutti gli altri campi la SF tende a zero in epoche recenti. Una volta analizzata la SF dei singoli campi, ho studiato la possibile presenza di gradienti radiali nelle popolazioni di NGC

6822. A tale scopo ho considerato due intervalli temporali, uno tra 0 e 0.5 Gyr e un altro tra 0.5 e 13.5 Gyr. Tutte mostrano degli andamenti esponenziali, le cui lunghezze di scala della popolazione giovane e di quella intermedia-vecchia sono perfettamente compatibili, con l'eccezione delle popolazioni giovani nei campi 1 e 3: l'attività di formazione stellare recente in questi due campi è più alta che negli altri. Questo potrebbe indicare che i due campi sono associati a bracci a spirale di recente formazione. Ho ricavato quindi la relazione età-metallicità per i sei campi studiati. Come atteso la metallicità cresce con il tempo, ma non sembra essere caratterizzata dalla presenza di gradienti radiali.

Le osservazioni di Draco sono composte da cinque campi, che coprono questa galassie fino a tre volte il raggio di *core*, $r_c = 9$ arcmin. La SFH di Draco è caratterizzata da un unico episodio di formazione stellare, avvenuto circa 12.9 Gyr fa, con un'ampiezza di 0.5 Gyr. Questo risultato è compatibile con un *quenching* dell'attività di formazione stellare da parte della reionizzazione cosmica, anche se lo studio spettroscopico delle metallicità in Draco sembra escludere che questo effetto possa aver avuto conseguenze. Infine ho studiato la presenza di gradienti radiali in Draco. Per tutte le sequenze evolutive si trovano dei profili esponenziali, di cui ho calcolato la lunghezza di scala. Queste sono tutte compatibili entro 3σ. Questo può essere interpretato come un'assenza di gradienti nelle popolazioni di questa galassia, che risulta quindi composta da un'unica popolazione.

Nel caso di UMi non ho ottenuto la SFH a causa di una forte discrepanza tra i modelli evolutivi e il CMD ossevato. Questa discrepanza non esiste considerando dati HST d'archivio. Per questo motivo ho richiesto due *set* di dati aggiuntivi utilizzando i telescopi IAC80 e NOT. Il primo è stato usato per verificare la calibrazione ottenuta, mentre il secondo per studiare la presenza di un'eventuale non linearità dei dati Subaru per stelle deboli. I dati così ottenuti hanno confermato la precedente calibrazione e non hanno permesso di identificare nessuna non linearità: di conseguenza ho effettuato uno studio usando i conteggi stellari nel CMD di UMi, in particolare ho studiato l'ampiezza del ramo delle sub giganti, confrontandola con i modelli di evoluzione stellare. Da questo confronto appare che UMi ha formato stelle per un intervallo che va tra i 0.15 e i 2 Gyr. Per concludere l'analisi di UMi ho studiato la presenza di gradienti radiali, come fatto per Draco, calcolando i parametri di scala per diverse sequenze evolutive. Anche in questo caso le lunghezze di scala risultano tutte compatibili entro 3σ, quindi anche UMi sembra essere composta da un'unica popolazione stellare.

La fotometria dei dati di Hercules risulta non abbastanza profonda per ottenere la SFH. Per questo motivo mi sono limitata a confrontare il CMD di questa galassia con alcuni ammassi globulari e alcune isocrone della libreria BaSTI (Pietrinferni et al. 2004). Da questo confronto appare che Hercules è composta da una popolazione stellare molto antica, con età superiore a 12 Gyr e basso contenuto di metalli.

Resumen

Mi tesis está focalizada en el estudio de las galaxias enanas del Grupo Local (GL). Ya que las galaxias del GL se pueden resolver en estrellas, este grupo ofrece un laboratorio perfecto para estudiar la formación y la evolución estelar y galáctica. Las galaxias enanas del GL son principalmente de tres tipos morfológicos, irregulares, esferoidales, y ultra debiles (UFD). Además, las historias de formación estelar (HFE) son fundamentales para obtener información sobre las poblaciones estelares de que están compuestas.

Las galaxias que he estudiado en mi tesis son una irregular, NGC 6822, dos esferoidales, Draco y Ursa Minor (UMi), y una ultra débil, Hercules.

Para todas las galaxias hice la fotometría aplicando el paquete DAOPHOT/ ALLSTAR/ ALLFRAME (Stetson 1987, 1994). De esta manera obtuve el diagramas color-magnitud (DCM) de cada galaxia. Los datos de NGC 6822 han sido obtenidos con el HST; los demás, con el telescopio Subaru. Para NGC 6822 y Draco derivé las HFEs usando el paquete desarrollado en el IAC específicamente para estudiar las poblaciones resueltas de las galaxias cercanas. Este paquete incluye IAC-star/ IAC-pop/ MinnIAC (Aparicio & Gallart 2004; Aparicio & Hidalgo 2009; Hidalgo et al. 2011).

Los datos de NGC 6822 están divididos en seis campos, que cubren todo el cuerpo principal de esta galaxia. La HFE de NGC 6822 está caracterizada por una subida de la tasa de formación estelar en los ultimos 500 Maños en los campos 1 y 3, mientras los demás campos tienen un tasa aproximadamente cero en épocas más recientes. Para NGC 6822 he estudiado también los gradientes de poblaciones estelares en dos intervalos temporales, uno joven entre 0 y 0.5 Gaños y otro entre 0.5 y 13.5 Gaños. Las escalas de longitud

en los dos intervalos temporales resultan perfectamente compatibles, con la excepción de las poblaciones jóvenes en los campos 1 y 3. Este resultado podría indicar que en estos dos campos hay brazos espirales en formación. Las relaciones edad-metalicidad muestran que la metalicidad crece con el tiempo y que no hay dependencia con la distancia desde el centro de la galaxia.

Draco ha sido observada en cinco campos, que cubren hasta tres veces su radio del núcleo. La HFE está caracterizada por un episodio de formación estelar, con edad de $\sim$ 12.9 Gyr y anchura de 0.5 Gyr. Este resultado es compatible con la extinción de la tasa de formació estelar por la reionización cosmica. No obstante, los estudios espectroscópicos arrojan dudas sobre esta interpretación. Para concluir el estudio de Draco me focalicé en los gradientes radiales de las poblaciones en esta galaxia. Calculé las escalas de longitud características de distintas fases evolutivas y los valores obtenidos son todos compatibles, dentro de los errores. Esto es una evidencia de que no hay gradientes radiales en las poblaciones de esta galaxia y por lo tanto se puede considerar compuesta de una sola población estelar muy antigua.

En el caso de UMi no he derivado la HFE, porque se ha encontrado una fuerte discrepancia entre los datos observados y los modelos de evolución estelar. Se excluye una peculiaridad real en esta galaxia, ya que los datos del HST son compatibles con los modelos evolutivos. Por esta razón he pedido dos observaciones adicionales, que se han realizado una con el IAC80 y otra con el NOT. Los datos del IAC80 han sido usados para comprobar los coeficientes derivados en la calibración fotométrica. En cambio, los datos del NOT, que llegan a magnitudes más profundas, fueron usados para excluir la posibilidad de que los datos del Subaru no sean lineales a magnitudes débiles. Ninguno de los dos grupos de datos ha ayudado a solucionar la discrepancia encontrada. Por esta razón comparé la anchura de la rama de las sub-gigantes observada con la de la rama de las sub-gigantes de los modelos, considerando distintos intervalos de muestreo de edad. Usando esta comparación se obtiene que el brote de formación estelar en UMi ha durado entre 0.15 y 2 Gaños. He seleccionado distintas fases evolutivas y, para estas he calculado las escalas de longitud. También en este caso todos resultan compatibles dentro de los errores. Lo mismo que Draco, UMi posee una población estelar única.

Para Hercules no derivé la HFE porque la fotometría no es bastante profunda. De todas formas, para obtener informaciones sobre las poblaciones estelares en esta galaxia, hice una comparación con cúmulos globulares e isócronas de la libreria BaSTI (Pietrinferni et al. 2004). Hercules está dominada por una población estelar muy antigua y de baja metalicidad.

Chapter 1

Introduction

1.1 The Local Group

Galaxy formation and evolution are still open problems. According to the most updated cosmological models, the so-called Λ cold dark matter (ΛCDM), smaller systems are the first to form (Governato et al. 2012). This is the so-called *bottom-up scenario*.

Searle & Zinn (1978) found that the metallicity in the Galactic Globular Clusters (GGC) is not correlated with their galactocentric distance. From this evidence they suggested that the clusters formed in the Galactic outer halo continued to fall into it for some time after the central regions had completed their formation. This can be considered the first observational confirmation of the *bottom-up scenario*.

Thus, the study of the smallest stellar systems in the Universe and, in particular, those which can be resolved into stars, play a major role in understanding how galaxies form and evolve. In this framework, the analysis of the dwarf galaxies of the Local Group (LG) can provide fundamental insights into this subject.

Dwarf galaxies are rich in dark matter (DM). This is the main difference between dwarf galaxies and GGC, which are believed not to contain any DM.

The Local Group (LG) has been defined by Hubble (1936) as *a typical small group of nebulae which is isolated in the general field.* The structure of the LG is shown in Fig. 1.1. The first historical census of the LG galaxies (Hubble 1936) was limited to the most luminous and nearby systems: the Milky Way (MW), M31 (Andromeda), the Large Magellanic Cloud (LMC), the Small Magellanic Cloud (SMC), M32, NGC 6822, NGC205, NGC185, IC1613, IC10, NGC147. At present, it is believed that the LG is constituted by two giant galaxies (the MW and M31) and a number of dwarf galaxies. According to the most recent catalogue (McConnachie 2012) there are about 100 dwarf galaxies which could belong to the LG. Out of these, 73 are members at a high confidence level, Tab. 1.1. Due to their very low luminosity dwarf galaxies are really arduous to detect. However, with the advent of new techniques of deep field imaging recently it has been possible to identify an increasingly large number of dwarfs (McConnachie 2012; Belokurov et al. 2007). On the other hand, it remains a challenge to detect dwarf members of external groups of galaxies. The census of dwarf galaxies belonging to the LG is still growing as new instruments are developed, and, consequently, extremely faint objects are continuously identified (Koposov et al. 2015).

ΛCDM scenario predicts a number of dwarf galaxies much larger than that observed. This is the so-called *missing satellite problem* which, despite the continuous discovery of very faint satellites, remains an open issue. However, recently, Sawala et al. (2014) showed that the discrepancy between the number of expected and observed dwarf galaxies could be alleviated on the basis of hydrodynamical simulations.

The LG includes all the morphological types of galaxies: spirals (as for the two giants), ellipticals, irregulars, and spheroidals. Hence, Tolstoy et al. (2009) suggest that the term *dwarf galaxy* should be used to refer to low luminosity galaxies, typically fainter than $M_V \approx -16$ or -17, which can be resolved into stars and studied as a unique sample. This is not a strict division, as in many cases the physical properties of giant and dwarf galaxies overlap (Fig. 1.2),

According to VandenBerg et al. (2000), dwarfs in the LG can be divided in three sub-groups:

- the MW sub-group;

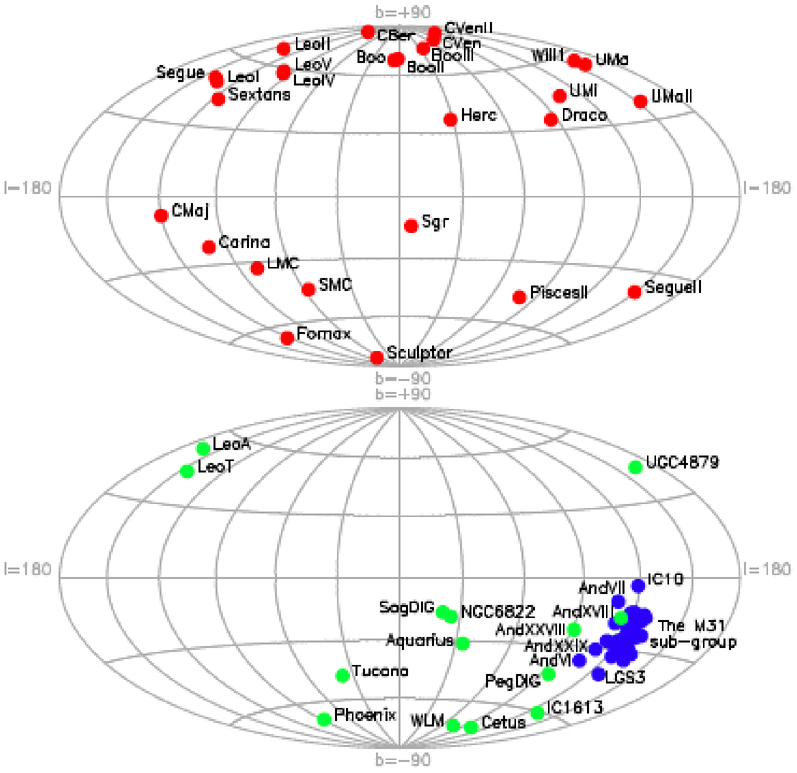

Figure 1.1: Galaxies in the LG. The red, blue, and green dots identify the galaxies belonging to the MW sub-group, Andromeda sub-group, and LGC. See text for a full description. Figure from McConnachie (2012).

- the Andromeda sub-group;
- a third group of dwarf galaxies of mainly irregulars, which appears rather isolated. This last group is called Local Group Cloud (LGC).

Dwarfs are not as simple as they pretend to be. Their star formation and chemical enrichment histories are very complex and varied. Therefore, dwarf galaxies constitute unique laboratories to test and constrain the theory of stellar evolution and star formation history. Moreover these systems are rich in DM, therefore, the study of the internal kinematics provides a substantial tool to constrain the characteristics of this still elusive constituent of the Universe (Governato et al. 2012).

Dwarf galaxies can be classified in two major categories: dwarf spheroidals/

Table 1.1: Census of the galaxies of the LG (McConnachie 2012 and references therein).

Galaxy	Subroup	Class	R.A. (J2000)	Dec. (J2000)	Galaxy	Subgroup	Class	R.A. (J2000)	Dec. (J2000)
The Galaxy	G	S(B)bc	17h45m40.0s	-29d00m28s	Andromeda XI	A	dSph	00h46m20.0s	+33d48m05s
Canis Major	G	????	07h12m35.0s	-27d40m00s	Andromeda V	A	dSph	01h10m17.1s	+47d37m41s
Sagittarius dSph	G	dSph	18h55m19.5s	-30d32m43s	Andromeda X	A	dSph	01h06m33.7s	+44d48m16s
Segue (I)	G	dSph	10h07m04.0s	+16d04m55s	Andromeda XXIII	A	dSph	01h29m21.8s	+38d43m08s
Ursa Major II	G	dSph	08h51m30.0s	+63d07m48s	Andromeda XX	A	dSph	00h07m30.7s	+35d07m56s
Bootes II	G	dSph	13h58m00.0s	+12d51m00s	Andromeda XII	A/L	dSph	00h47m27.0s	+34d22m29s
Segue II	G	dSph	02h19m16.0s	+20d10m31s	NGC 147	A	dE/dSph	00h33m12.1s	+48d30m32s
Willman 1	G	dSph	10h49m21.0s	+51d03m00s	Andromeda XXI	A	dSph	23h54m47.7s	+42d28m15s
Coma Berenices	G	dSph	12h26m59.0s	+23d54m15s	Andromeda XIV	A/L	dSph	00h51m35.0s	+29d41m49s
Bootes III	G	dSph?	13h57m12.0s	+26d48m00s	Andromeda XV	A	dSph	01h14m18.7s	+38d07m03s
LMC	G	Irr	05h23m34.5s	-69d45m22s	Andromeda XIII	A	dSph	00h51m51.0s	+33d00m16s
SMC	G	dIrr	00h52m44.8s	-72d49m43s	Andromeda II	A	dSph	01h16m29.8s	+33d25m09s
Bootes (I)	G	dSph	14h00m06.0s	+14d30m00s	NGC 185	A	dE/dSph	00h38m58.0s	+48d20m15s
Draco	G	dSph	17h20m12.4s	+57d54m55s	Andromeda XXIX	A	dSph	23h58m55.6s	+30d45m20s
Ursa Minor	G	dSph	15h09m08.5s	+67d13m21s	Andromeda XIX	A	dSph	00h19m32.1s	+35d02m37s
Sculptor	G	dSph	01h00m09.4s	-33d42m33s	Triangulum	A	Sc	01h33m50.9s	+30d39m37s
Sextans (I)	G	dSph	10h13m03.0s	-01d36m53s	Andromeda XXIV	A	dSph	01h18m30.0s	+46d21m58s
Ursa Major (I)	G	dSph	10h34m52.8s	+51d55m12s	Andromeda VII	A	dSph	23h26m31.7s	+50d40m33s
Carina	G	dSph	06h41m36.7s	-50d57m58s	Andromeda XXII	A	dSph	01h27m40.0s	+28d05m25s
Hercules	G	dSph	16h31m02.0s	+12d47m30s	IC 10	A	dIrr	00h20m17.3s	+59d18m14s
Fornax	G	dSph	02h39m59.3s	-34d26m57s	LGS 3	A	dIrr/dSph	01h03m55.0s	+21d53m14s
Leo IV	G	dSph	11h32m57.0s	-00d32m00s	Andromeda VI	A	dSph	23h51m46.3s	+24d34m57s
Canes Venatici II	G	dSph	12h57m10.0s	+34d19m15s	Andromeda XVI	A/L	dSph	00h59m29.8s	+32d22m36s
Leo V	G	dSph	11h31m09.6s	+02d13m12s	Andromeda XXVIII	A/L	dSph?	22h32m41.2s	+31d12m58s
Pisces II	G	dSph	22h58m31.0s	+05d57m09s	IC 1613	L	dIrr	01h04m47.8s	+02d07m04s
Canes Venatici (I)	G	dSph	13h28m03.5s	+33d33m21s	Phoenix	L/G	dIrr/dSph	01h51m06.3s	-44d26m41s
Leo II	G	dSph	11h13m28.8s	+22d09m06s	NGC 6822	L/G	dIrr	19h44m56.6s	-14d47m21s
Leo I	G/L	dSph	10h08m28.1s	+12d18m23s	Cetus	L	dSph	00h26m11.0s	-11d02m40s
Andromeda	A	Sb	00h42m44.3s	+41d16m09s	Pegasus dIrr	L/A	dIrr/dSph	23h28m36.3s	+14d44m35s
M32	A	cE	00h42m41.8s	+40d51m55s	Leo T	L/G	dIrr/dSph	09h34m53.4s	+17d03m05s
Andromeda IX	A	dSph	00h52m53.0s	+43d11m45s	WLM	L	dIrr	00h01m58.2s	-15d27m39s
NGC 205	A	dE/dSph	00h40m22.1s	+41d41m07s	Leo A	L	dIrr	09h59m26.5s	+30d44m47s
Andromeda XVII	A	dSph	00h37m07.0s	+44d19m20s	Andromeda XVIII	L	dSph	00h02m14.5s	+45d05m20s
Andromeda I	A	dSph	00h45m39.8s	+38d02m28s	Aquarius	L	dIrr/dSph	20h46m51.8s	-12d50m53s
Andromeda XXVII	A	dSph	00h37m27.1s	+45d23m13s	Tucana	L	dSph	22h41m49.6s	-64d25m10s
Andromeda III	A	dSph	00h35m33.8s	+36d29m52s	Sagittarius dIrr	L	dIrr	19h29m59.0s	-17d40m41s
Andromeda XXV	A	dSph	00h30m08.9s	+46d51m07s	UGC 4879	L	dIrr/dSph	09h16m02.2s	+52d50m24s
Andromeda XXVI	A	dSph	00h23m45.6s	+47d54m58s					

dwarf ellipticals (dSph/dE) and dwarf irregulars (dIrr). The LG contains a unique mixture of dSphs and dIrrs. Since that the relationship between these two classes of galaxies is still unknown, the LG offers a natural laboratory to address the problem. A new class, the ultra-faint dwarf galaxies (UFD), has been recently introduced. With this term we refer to the extremely faint dwarf galaxies which are continuously discovered and which apparently share the main properties of dSphs.

Observations reveal striking differences: dIrr are rich in HI and show still ongoing star formation activity, at odds with dSphs whose star formation history appears much more episodic and quiescent during the last Gyrs (Tolstoy 2010). Thus, dIrrs ans dSphs are often called late- and early-type galaxies. It is noticeable that dSphs are generally found near (¡130 kpc) the two giant galaxies and constitute a system of satellites for these. This is not true for dIrrs whose location appears sparse and at distances larger than 400 kpc from the MW and M31. An exception to the rule are the two irregulars SMC and LMC, which are located at a distance less than 100 kpc from the MW.

Fig. 1.2 shows where different stellar systems in the LG lie if we consider the central surface brightness and the half-light radius as a function of the absolute V magnitude. When the central surface brightness is considered as a function of the absolute V magnitude, it is clear that all dwarf galaxies, despite of their morphological type, lie in a well defined sequence. This sequence is separated from those of the GGC. These two sequences overlap where the so-called UFDs lie. From this plot it appears that UFDs are the natural extension of the sequence associated to dwarf galaxies. Hence, they should belong to the same class of objects. On the contrary, when we consider the half-light radius as a function of the absolute V magnitude, dwarf galaxies and GGC sequences are well separated. At a first view the UFD sequence appears separated from that of the dwarf galaxies. However, this might be due to the errors in the measurement of the size of these systems, which is particularly difficult because of their low luminosity.

As already stated, from Fig. 1.2 it appears that despite the morphological type, both dSphs and dIrrs exhibit the same structural properties. A detailed comparison between the galaxies of different morphological type is needed in order to understand the relation, if there is any, between them.

In my thesis I studied four dwarf galaxies of the LG. These are NGC 6822, Draco, Ursa Minor, Hercules, put in order from the largest to the smallest. These four galaxies cover a wide variety of types as they are respectively a dwarf irregular galaxy, two dwarf spheroidals, and an ultra-faint dwarf.

1.2 Dwarf Irregular Galaxies

The term *irregulars* refers to the optical appearance of these galaxies: unlike the smooth, structureless aspect of dE/dSphs, dIrrs show distinct structures on different scales. In addition, there is general evidence that star formation is not uniformly distributed across the dIrrs (Da Costa 1998). As many galaxies of the LG, dIrrs generally show hints of the presence of significative amounts of DM, which seems to form an extended halo around the dwarfs (Donato et al. 2009).

Because of their still ongoing star formation, dIrrs are very interesting systems to address many open questions of modern astrophysics related to galaxy formation and stellar evolution.

As already noted, dIrrs are generally bluer, smaller, less luminous and richer in gas than dSph. The latter is strictly correlated to the of star formation activity so that one could expect to find a significative abundance of young stars. All these features indicate that dIrrs are either recently formed galaxies or slowly evolving galaxies (Yin et al. 2011). However the former appears to be at odds with the frequent presence of old populations. A deep study of the nearest star-forming dIrr galaxies, may not only give us answers on all these issues, but it could also shed light on the possible relation between dIrrs and dSphs. On the other hand, Grebel et al. (2003) confirm that dSphs and dIrrs constitute two separate classes, as previously stated by Binggeli (1994) and Skillman & Bender (1995), since the transition from dIrrs to dSphs through gas loss seems to be unlikely.

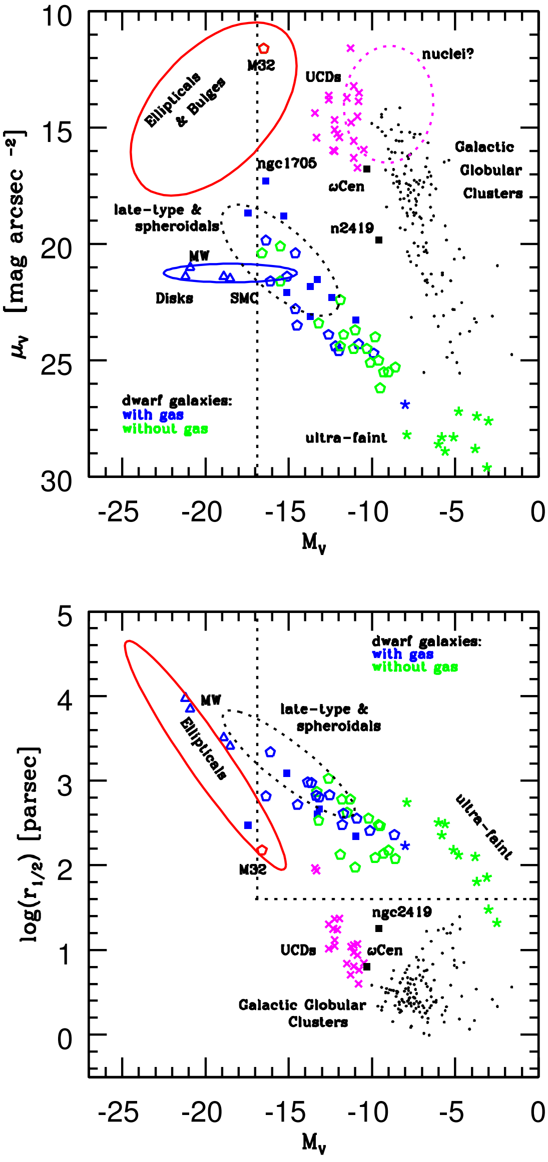

Figure 1.2: Figure from Tolstoy et al. (2009). Dotted lines indicate the classical limits of the dwarf galaxy class as defined by Tammann (1994). The central surface brightness, μ_V as a function of the absolute magnitude, M_V, and the half light radius, $r_{1/2}$, as a function of the absolute magnitude, M_V are shown respectively in the *upper* and *lower panel*. Marked with coloured ellipses are the typical locations of Elliptical galaxies & bulges (red), spiral galaxy disks (blue), galactic nuclei (dashed magenta) and large early (spheroidals) and late-type systems (dashed black). GGCs are plotted individually as small black points. M 31, the Milky Way (MW), M 33 and LMC are shown as blue open triangles. LG dwarf galaxies are plotted as open pentagons, blue for systems with gas and green for systems without gas. The recently discovered UFDs are given star symbols, and the same colour code. Blue- and ultra-compact dwarfs are marked respectively as blue solid squares and as magenta crosses. For references and a complete discussion see Tolstoy et al. (2009).

Table 1.2: NGC 6822 structural parameters

Structural Parameter	Value	Reference^a
R.A., α (J2000)	$19^h44^m56.6^s$	(1)
DEC., δ (J2000)	$-14^d47^m21^s$	(1)
Galactic longitude, l (°)	25.4	(1)
Galactic latitude, b (°)	-18.4	(1)
Ellipticity, e	0.24 ± 0.05	(2)
Core radius, r_c ($'$)	2.5 ± 1.0	(2)
Tidal radius, r_t ($'$)	40 ± 10	(2)
Half light radius, r_h ($'$)	2.65 ± 1.0	(2)
Luminosity, L_V ($L_\odot$)	10^8	(3)
Baryonic mass, M_* ($M_\odot$)	8.3×10^7	(3)
Central surface brightness, μ_V (mag arcsec^{-2})	19.7	(1)
Absolute V magnitude, M_V	-15.2 ± 0.2	(1)

[a] (1) (McConnachie 2012); (2) (Mateo 1998); (3) (Kirby et al. 2013a).

1.2.1 NGC 6822

NGC 6822, discovered by Barnard (1884), is a barred dwarf galaxy of type Ir IV-V (van den Bergh 1998). This galaxy is one of the nearest dIrr to the MW and, according to Cannon et al. (2012) it is rich in gas and it is still active in forming stars.

This Local Group dwarf galaxy is similar in size, structure and metallicity to the Small Magellanic Cloud (SMC). Therefore, this LG galaxy can play a fundamental role both in the study of stellar evolution and in understanding the star formation history in complex stellar systems. In addition NGC 6822 is dark matter dominated (de Blok & Walter 2000).

The first detailed study of NGC 6822 was carried out by Hubble who discovered 11 Cepheid variables. He noticed that *"Cepheid variables, diffuse nebulae, dimensions, density, and distribution of stellar luminosity, all converge in defining NGC 6822 as a curiously faithful copy of the Magellanic Clouds, shifted to a vastly greater distance. NGC 6822 lies far outside the limits of the Galactic system, even as outlined by the globular clusters, and hence may serve as a stepping-stone for speculation concerning the habitants of space beyond"*.

Tab. 1.2 reports the structural parameters of NGC 6822.

NGC 6822 is located at a distance of $459 \pm 17 kpc$ (McConnachie 2012) and it is a true member of the LGC (Mateo 1998). Due to its relative proximity, NGC 6822 has been the focus of numerous investigations of its stellar content. The distance modulus of this dwarf irregular has been estimated by several authors with consistent results. Lee et al. (1993) using the magnitude level of red giant branch (RGB) tip, give $(m - M)_0 = 23.46 \pm 0.08$; Gallart et al. (1996c) used UBVRI photometry of eight Cepheids, estimate $(m - M)_0 = 23.49 \pm 0.08$; Cioni & Habing (2005) estimate $(m - M)_0 = 23.34 \pm 0.12$ using near-IR photometry of asymptotic giant branch (AGB) stars; Gieren et al. (2006) obtained $(m - M)_0 = 23.312 \pm 0.021$ through near IR photometry of Cepheids in the innermost region of NGC 6822, and finally Feast et al. (2012) found $(m - M)_0 = 23.40 \pm 0.05$ through JHK photometry of classical Cepheids. Because of its low galactic latitude NGC 6822 is affected by moderate foreground extinction (Schlegel et al. 1998). Massey et al. (1995) estimated the reddening as $E(B - V) = 0.26$ in the outer region and $E(B - V) = 0.45$ near the center. Gallart et al. (1996c) obtained $E(B - V) = 0.24 \pm 0.03$, and Gieren et al. (2006) $E(B - V) = 0.356 \pm 0.013$.

According to a recent study based on *HST* photometric data Fusco et al. (2012) find a distance to this galaxy of $(\mathrm{m - M})_0 = 23.54 \pm 0.05$ using the method of the tip of the RGB. In addition, they find a difference in the extinction between the central and outer regions, which result in $E(B - V) = 0.37 \pm 0.02$ and $E(B - V) = 0.30 \pm 0.03$, respectively. The most recent distance modulus for this galaxy has been given by Rich et al. (2014), who give $(\mathrm{m - M})_0 = 23.38 \pm 0.04$ and $E(B - V) = 0.35 \pm 0.04$.

The galaxy contains an intermediate-age stellar population covering an area $14' \times 11'$and a small optical bar of $6' \times 11'$ (Cioni & Habing 2005). de Blok & Walter (2000, 2006) found that NGC 6822 neutral interstellar medium is characterized by the presence of a giant HI hole, and a super giant HI shell. They suggest that the hole could be originated by a supernova explosion, while the shell could be the hint of a strong interaction with a hypothetical galaxy-companion.

The star formation history and the stellar content of this galaxy has been studied by several authors (e.g. Gallart et al. 1996b; Komiyama et al. 2003; Letarte et al. 2002; Wyder 2001; de Blok & Walter 2003; Cannon et al. 2012. According to these studies NGC 6822 has probably started forming stars at a constant rate between 12 and 15 Gyr ago. After this period of intense star formation, in the last few Gyr there has been a decrease in the rate of star formation. However the star production rate began to increase again with a new burst about 3 Gyr ago (Tolstoy et al. 2001). Apparently this increase continued up to the last 100- 200 Myr (Gallart et al. 1996b; Hutchings et al. 1999). According to Cannon et al. (2012) the star formation history is constant throughout the galaxy. Many variable stars have been found at the tip of the RGB. These are probably of very long period (Baldacci et al. 2003), and age between 1 and 10 Gyr.

Estimates of metallicity of NGC 6822 are listed in Tab. 1.3 together with the reference and technique used. Cioni & Habing (2005), investigating the ratio between carbon-rich and oxygen-rich giant branch stars, conclude that the spread in metallicity is around 1.56 dex. Pagel et al. (1980) estimate the gaseous oxygen abundance as $12+\log(O/H) = 8.2\pm0.2$ studying H II regions; subsequent spectroscopical analysis by Peimbert et al. (2005) and Hernández-Martínez et al. (2009) give, respectively, $12 + \log(O/H) = 8.42 \pm 0.06$ and $12 + \log(O/H) = 8.06 \pm 0.04$ compatible with Pagel's result. Peimbert et al. (2005) studied the abundance of other elements and gave: $12 + \log(He/H) = 10.909\pm0.011$, $\log(C/O) = -0.31\pm0.13$, $\log(N/O) = -1.37\pm 0.17$, $\log(Ne/O) = -0.79 \pm 0.09$, $\log(S/O) = -1.62 \pm 0.09$, $\log(Cl/O) = -3.71 \pm 0.10$, $\log(Ar/O) = -2.36 \pm 0.08$, and $\log(Fe/O) = -1.41 \pm 0.10$.

1.3 Dwarf Spheroidal Galaxies

Contrary to dIrrs, dSphs, as the name says, appear to have a spheroidal/ elliptical shape and a relatively smooth distribution of stars (Grebel et al. 2003). They are very extended in the sky, so a wide-field imaging is needed in order to have a complete view of these systems, especially on the population

Table 1.3: NGC 6822 [Fe/H] abundance with associated reference and method of detection.

[Fe/H]	Method	Reference[a]
-1.20 ± 0.30	optical spectrophotometry	(1)
-1.50 ± 0.30	optical photometry	(2)
-1.00 ± 0.30	CaII triplet absorption lines in RGB stars	(3)
-0.49 ± 0.22	Optical spectroscopy of A-type stars	(4)
-1.92 ± 0.35	RR Lyrae average period	(5)
-1.30 ± 0.20	C/M ratio in AGB stars	(6)
-1.29 ± 0.07	C/M ratio in AGB stars	(7)
-1.00 ± 0.50	Spectroscopy of RGB stars	(8)

[a] (1) Skillman et al. (1989); (2) Gallart et al. (1996c); (3) Tolstoy et al. (2001); (4) Venn et al. (2001); (5) Clementini et al. (2003); (6) Kacharov et al. (2012); (7) Sibbons et al. (2012); (8) Kirby et al. (2013b).

gradients they often show.

At first it was thought that these systems were similar to GGC. The study by Faber & Lin (1983) showed that the profiles are much more like those of disk galaxies. Therefore the mass-to-light ratio is higher than previously thought. In general they show $M/L \geq 30 M_{\odot}/L_{\odot}$.

dSphs have no gas left, which means they have a typical red colour and they are mainly dominated by an old population. The CMD analysis of dSph immediately reveals that they exhibit prominent horizontal branches (HB), typically associated to extremely old populations. On the contrary they do not show any feature of the presence of intermediate-young populations, such as red clump (RC) or bright blue main sequences (MS; Grebel & Gallagher 2004; Weisz et al. 2014).

It is not clear which is the physical mechanism which could cause the loss of gas and hence the stop of SF activity. According to Grebel et al. (2003) the most plausible mechanism is gas removal via ram-pressure stripping. This conclusion, together with tidal effects, is compatible with the proximity of these systems to larger galaxies, such as the MW.

All old dSphs show a significant metallicity dispersion (Kirby et al. 2013b), which means that the SF activity should have lasted longer than 1-2 Gyr.

1.3.1 Ursa Minor

UMi is one of the faintest dSph of the LG. It is known as one of the dwarf galaxies companions of the MW (Mateo 1998; McConnachie 2012). The main structural parameters of this galaxy are listed in 1.4.

Several authors studied the distance to this galaxy through photometric studies. Mighell & Burke (1999) find $(\mathrm{m}-\mathrm{M})_0 = 19.18 \pm 0.12$ using the galactic globular cluster M92, while Carrera et al. (2002) find $(\mathrm{m}-\mathrm{M})_0 = 19.4 \pm 0.1$, corresponding to 74 ± 4 kpc, and Bellazzini et al. (2002) obtain $(\mathrm{m}-\mathrm{M})_0 = 19.41 \pm 0.12$. Its reddening is estimated to be $\mathrm{E(B-V)} = 0.03$ (Schlegel et al. 1998; Schlafly & Finkbeiner 2011).

In addition, the metallicity of this galaxy has been widely studied both photometrically and spectroscopically. Mighell & Burke (1999), using *Hubble Space Telescope* (HST) data, obtain $[\mathrm{Fe/H}]_{\mathrm{UMi}} = -2.2$. Furthermore Bellazzini et al. (2002) estimate an average value of the metallicity $\langle[\mathrm{Fe/H}]\rangle = -1.8 \pm 0.1$ based on *Telescopio Nazionale Galileo* (TNG) data. From data observed with the *Isaac Newton Telescope* (INT) Carrera et al. (2002) give $[\mathrm{Fe/H}] = -1.9 \pm 0.2$. A spectroscopical study using HIRES on the Keck I telescope was carried out by Shetrone et al. (2001). From these data they estimated a mean value $\langle[\mathrm{Fe/H}]\rangle = -1.9 \pm 0.1$ and an unambiguous internal dispersion $\Delta[\mathrm{Fe/H}] = 0.73$. Kirby et al. (2013a) performed a spectroscopic survey on several dwarf galaxies of the LG using the Keck DEIMOS spectrograph. In the case of UMi the mean metallicity they obtain is $[\mathrm{Fe/H}] = -2.13 \pm 0.01$, with a dispersion of 0.43 dex.

The star formation history shows that UMi formed stars until 10 Gyr ago in a unique episode of SF (Mighell & Burke 1999; Carrera et al. 2002; Dolphin 2002; Orban et al. 2008), and therefore the mean stellar age is $\sim$12 Gyr (Carrera et al. 2002; Orban et al. 2008). The time scale of the main SF episode is controversial. Ikuta & Arimoto (2002) suggest this took place on a time scale of several Gyr with a very low star formation rate (SFR), while Kirby et al. (2013a) find that the burst lasted 0.4 Gyr.

Carrera et al. (2002) and Dolphin (2002) identify the presence of many blue stars, brighter than the old population turn off (TO). These stars might be either young main sequence (MS) stars, which would mean UMi has formed stars until 2 Gyr ago, or blue stragglers (BSS) formed by the old population (Carrera et al. 2002). The second option is more probable according to the authors. Mapelli et al. (2007) performed a specific analysis on the BSS in UMi. The radial distribution of BSS throughout the galaxy is almost flat, with a slight decrease toward the centre. This distribution is expected if the progenitors of the BSS are mass transfer binaries (Mapelli et al. 2006; Santana et al. 2013).

UMi is one of the best candidates for being in the terminal phase of its complete tidal disruption caused by the MW. The first hint comes from Armandroff et al. (1995), who find a very high velocity dispersion – 8.5 ± 0.7 km s^{-1}. In addition, Kleyna et al. (1998) find a statistically significant asymmetry in the stellar distribution along the UMi major axis. Martínez-Delgado et al. (2001) detect many MS and HB stars beyond its tidal radius. The low SFR during its main burst of SF (Ikuta & Arimoto 2002) would mean that plenty of gas should remain at the end of the SF episode. However Young (2000) shows that UMi does not contain a significant fraction of H I atomic gas. To explain this absence of gas neither the SFR detected nor a possible supernova explosion are enough. The only explanation for this observational effect is tidal stripping by the MW, which pulls out H I atomic gas and consequently stops the SF activity (Ikuta & Arimoto 2002).

1.3.2 Draco

This galaxy, together with UMi, is one of the faintest dSph of the LG. At odds of UMi, Draco does not show any sign of tidal disruption, no presence of tidal tails, and no apparent rotation, but a very high mass-to-light ratio (M/L, e.g. Armandroff et al. 1995; Odenkirchen et al. 2001). The M/L in Draco ranges between 350 and 1000 $M_{\odot}/L_{\odot}$, which makes this system one of the most DM dominated known (Kleyna et al. 2001). The main structural properties of this dSph are listed in Table 1.5.

The distance to Draco is in good approximation similar to that of UMi (Fattahi et al. 2013). Using photometric data both Aparicio et al. (2001)

Table 1.4: UMi structural parameters

Structural Parameter	Value	Reference[a]
R.A., α (J2000)	$15^h09^m08^s.5$	(1)
DEC, δ (J2000)	$+67^d13^m21^s$	(1)
Galactic longitude, l (°)	105.0	(1)
Galactic latitude, b (°)	+44.8	(1)
Ellipticity, e	0.56 ± 0.05	(2)
Core radius, r_c ($'$)	15.8 ± 1.2	(2)
Tidal radius, r_t ($'$)	50.6 ± 3.6	(2)
Half light radius, r_h ($'$)	8.20 ± 1.2	(1)
Luminosity, L_V ($L_\odot$)	2.8×10^5	(3)
Baryonic mass, M_* ($M_\odot$)	5.4×10^5	(3)
Dynamical mass, $M_{dyn}(\leq r_h)$ ($M_\odot$)	9.5×10^6	(1)
Central surface brightness, μ_V (mag arcsec^{-2})	26 ± 0.5	(1)
Absolute V magnitude, M_V	-0.8 ± 0.5	(1)

[a] (1) McConnachie (2012); (2) Irwin & Hatzidimitriou (1995); (3) Kirby et al. (2013a)

and Bellazzini et al. (2002), estimate the distance to this galaxy to be $(\mathrm{m}-\mathrm{M})_0 = 19.5$, or $d = 80 \pm 7$ kpc. The most recent estimate of the distance to this galaxy using RR Lyrae variable stars given by Bonanos et al. (2004) is $(\mathrm{m}-\mathrm{M})_0 = 19.40 \pm 0.15$. The galactic extinction in Draco's direction is $\mathrm{E(B-V)} = 0.024$ (Schlegel et al. 1998; Schlafly & Finkbeiner 2011).

Several authors studied the mean metallicity of Draco. The metallicity resulting from the photometric studies by Aparicio et al. (2001) and Bellazzini et al. (2002) are $[\mathrm{Fe/H}] = -1.8 \pm 0.2$ and $[\mathrm{Fe/H}] = -1.7 \pm 0.1$, respectively. The high resolution spectroscopic analysis by Shetrone et al. (2001) gives a mean metallicity of $[\mathrm{Fe/H}] = -2.0 \pm 0.2$. Moreover, they identify an unambiguous internal dispersion of $\Delta[\mathrm{Fe/H}] = 1.53$. In the most updated study of the metallicity in Draco Kirby et al. (2013a) obtain a mean value of $[\mathrm{Fe/H}] = -1.98$ with an internal dispersion of $\Delta[\mathrm{Fe/H}] = 0.42$.

Aparicio et al. (2001) carried out a complete study of the SFH of this galaxy. They find that the bulk of the SF took place before 10 Gyr ago. In the last ~ 2 Gyr they do not detect any significant SF activity, which finds the perfect counter part in the low content of HI (Gallagher et al. 2003).

Table 1.5: Draco structural parameters

Structural Parameter	Value	Reference[a]
R.A., α (J2000)	$17^h20^m12^s.4$	(1)
DEC, δ (J2000)	$+57^d54^m55^s$	(1)
Galactic longitude, l (°)	86.4	(1)
Galactic latitude, b (°)	+34.7	(1)
Ellipticity, e	0.31 ± 0.02	(1)
Core radius, r_c (′)	9.0 ± 0.7	(2)
Tidal radius, r_t (′)	28.3 ± 2.4	(2)
Half light radius, r_h (′)	8.20 ± 1.2	(1)
Luminosity, L_V ($L_\odot$)	2.7×10^5	(3)
Baryonic mass, M_* ($M_\odot$)	3.2×10^5	(3)
Dynamical mass, $M_{dyn}(\leq r_h)$ ($M_\odot$)	11×10^6	(1)
Central surface brightness, μ_V (mag arcsec^{-2})	25 ± 0.5	(1)
Absolute V magnitude, M_V	-8.8 ± 0.3	(1)

[a] (1) McConnachie (2012); (2) Irwin & Hatzidimitriou (1995); (3) Kirby et al. (2013a)

Ikuta & Arimoto (2002) suggest that the SF timescale in Draco was longer than for UMi. Orban et al. (2008) use HST photometric data to study the SFH in Draco. They find that Draco formed ~ 50% of its stars before 10 Gyr ago, and the mean stellar age is 10.9 Gyr. In addition, Aparicio et al. (2001) find many blue stars, brighter than the old population TO. As in the case of UMi, these are BSS, whose progenitors are mass transfer binaries (Mapelli et al. 2007; Santana et al. 2013).

1.4 Ultra Faint Dwarf Galaxies

In literature, the the newly, extremely dim dwarf galaxies which are being discovered in the last decade are called ultra faint dwarf galaxies (UFD). The major contribution was given by the SDSS survey. UFDs have the same properties of dSphs, but with magnitude $M_V \leq -7$ (Tolstoy et al. 2009).

As shown in Fig. 1.2, UFDs appear to be the natural extension of the dSph, but for the faintest of them the properties are very similar to that of GGC.

As the dSph these systems are mainly dominated by an old population and they do not show any sign of ongoing SF. The CMD analysis of UFDs is particularly arduous, because of Galactic contamination.

Many UFDs show a high ellipticity, which can be possibly ascribed to tidal disruption by the MW. Fundamental evidence comes from stellar kinematics of the single stars in UFDs (Tolstoy et al. 2009).

Simon & Geha (2007) showed that these systems are more DM dominated than all the other systems known, with mass-to-light ratio between 140 and 1700 $M_\odot/L_\odot$. Their metallicities are lower than those found in classical dSphs, with a scatter higher than that of GGC (Kirby et al. 2013b).

Their origin is still not clear. Probably there is a range of origins for these systems. The existence of such systems reduces the minumum mass of objects in which stars can form (Bovill & Ricotti 2011).

1.4.1 Hercules

Hercules is an UFD and a satellite of the MW. It was discovered in 2007 using the SDSS survey (Belokurov et al. 2007). Table 1.6 lists the structural parameters of this galaxy.

The distance to this galaxy has been studied by several authors. Belokurov et al. (2007) give $(m - M)_0 = 20.7 \pm 0.2$, which corresponds to 140 ± 13kpc; Coleman et al. (2007) using wide field photometry give 20.6 ± 0.2kpc; Adén et al. (2009) obtained 20.84 ± 0.11kpc, combining photometric and spectroscopic observations of the Ca II IR triplet, and Musella et al. (2012) using RRLyrae estimated $(m - M)_0 = 20.6 \pm 0.1$, corresponding to 132 ± 6kpc. The reddening has been estimated between $E(B - V) = 0.055 \pm 0.005$ and $E(B - V) = 0.09 \pm 0.02$ (Coleman et al. 2007; Musella et al. 2012). According to Schegel's maps the reddening in the direction of Hercules is $E(B - V) = 0.063$ (Schlegel et al. 1998; Schlafly & Finkbeiner 2011).

As all the UFDs, Hercules shows a very low metal content. Several spectroscopical studies lead to comparable results. Simon & Geha (2007) estimate $[Fe/H] = -2.27$ with a dispersion of $\sigma_{[Fe/H]} = 0.31$; Adén et al. (2011) find that the metallicity in Hercules ranges between -3.2 and -2.0; Kirby

Table 1.6: Hercules structural parameters

Structural Parameter	Value	Reference[a]
R.A., α (J2000)	$16h31^m02^s.0$	(1)
DEC, δ (J2000)	$+12^d31^m0^s$	(1)
Galactic longitude, l (°)	28.7	(1)
Galactic latitude, b (°)	+36.9	(1)
Ellipticity, e	0.68 ± 0.08	(2)
Core radius, r_c ($'$)	4.74 ± 0.57	(3)
Tidal radius, r_t ($'$)	25.9 ± 11.1	(3)
Half light radius, r_h ($'$)	8.6 ± 1.5	(2)
Luminosity, L_V ($L_\odot$)	3.6×10^4	(4)
Baryonic mass, M_* ($M_\odot$)	3.7×10^4	(4)
Dynamical mass, $M_{dyn}(\leq r_h)$ ($M_\odot$)	2.6×10^6	(5)
Central surface brightness, μ_V (mag arcsec^{-2})	27.2 ± 0.6	(5)
Absolute V magnitude, M_V	-6.6 ± 0.4	(5)

[a] (1) Belokurov et al. (2007); (2) Martin et al. (2008); (3) (Coleman et al. 2007); (4) Kirby et al. (2013b); (5) McConnachie (2012)

et al. (2013b) [Fe/H] $= -2.39$ with a dispersion of 0.51 using 19 RGB stars estimated. Very similar results are obtained by photometric studies, as for example Musella et al. (2012) who obtained [Fe/H] $= -2.30 \pm 0.15$ and Fabrizio et al. (2014) who derived that the metallicity ranges between -3.3 and -1.8.

The SFH of Hercules shows that it is dominated by an old population. All authors (e.g. Sand et al. 2009; Brown et al. 2012; Fabrizio et al. 2014) agree that no significant SF activity took place after 12 Gyr ago. Adén et al. (2011) and Vargas et al. (2013) note that the SFR has been very low and of very short duration of at least ~ 100 Myr. As Draco and UMi, Her shows stars bluer than the MS TO. As in the previous cases this are BSS, whose progenitors result to be mass-transfer binaries (Santana et al. 2013).

Using wide field photometry it has been found that this UFD is highly elliptical (Belokurov et al. 2007; Martin et al. 2008), more than all the other dwarf satellites of the MW, with the exception of the Sagittarius dwarf. According to Coleman et al. (2007) the ellipticity increases from the inner to the outer regions, rising from ~ 0.3 to 0.65 and there are signs for a clumpy substructure. Recently Roderick et al. (2015) studied in detail the substructures in this system, using DECam data. Thanks to the dimension of this camera it has been possible to detect many substructures in this galaxy, which confirm the hypothesis that Hercules is tidally disrupted. In addition, they detected two free-floating debris, probably meaning that Hercules did more than one peri-galactic pass, with an infall timescale of 2-5 Gyr.

1.5 The Star Formation History in the Local Group

The study of the SFH of resolved stellar populations was first initiated by Baade in the 1940s. Since then the astronomical community recognized the importance of this method of analysis and a number of developments have been made. The derivations of the SFH is based on the study of colour-magnitude diagrams (CMD), accompanied by highly reliable stellar evolutionary models (e.g. Pietrinferni et al. 2004; Girardi et al. 2000). Stars at different evolutionary stages occupy different regions of the diagram.

A fundamental assumption in this method is that all the stars belonging to the same system have within the errors the same distance and the same reddening. The CMDs of stellar systems allow the detailed study of stellar populations, which means collecting details about the age, metal content, and initial mass function (IMF) of a given system.

In the last decades the introduction of new technologies, as CCDs, and space-based telescopes, as the HST, have significantly improved the power of the study of resolved stellar populations using CMDs (e.g. Hidalgo et al. 2013; Weisz et al. 2014).

Moreover, due to the improvement in computational power, the comparison of an observed CMD to a synthetic CMD has been introduced. A number of codes able to perform this comparison have been developed in the last years (Tolstoy et al. 2009; Hidalgo et al. 2011). The advantage of this technique, compared to the simple isochrone comparison, is that we can *easily* disentangle composite stellar populations in stellar systems (e.g. Tolstoy et al. 2009; Hidalgo et al. 2013).

The synthetic CMD is created by selecting a library of evolutionary models, and assuming an IMF, a binary fraction, and a distribution in age and metallicity. Then the accurate simulation of photometric errors, through artificial star tests, is used to reproduce the observational effects on the synthetic CMD. A full description of the method is given in Section 4.

The SFH of the dwarf galaxies of the LG is fundamental. Their proximity and small dimension make it possible to resolve them into stars and to obtain an overview on the evolution and formation of the whole system (e.g. Hidalgo et al. 2013; del Pino et al. 2013).

As mentioned above, according to cosmological model dwarfs are the first systems to form. They were shaped during their journey to present day by a number of both internal (e.g. star formation, stellar feedback from supernovae) and external (e.g. tidal effects, intense ultra-violet radiation from the time of cosmic reionization) processes, of which they still maintain a record (e.g. Weisz et al. 2014). Thus, the study of the SFHs give a panoramic view on how these effects acted, shedding light on the astrophysical processes involved.

In particular, ΛCDM predicts the early collapse of low-mass halos, massive enough to host galaxies. The number of dwarf galaxies predicted by this approach exceeds by orders of magnitude those observed. This can be explained by cosmic reionization, which prevents the formation of galaxies in low-mass halos (Moore et al. 1999).

When gas began to settle in the interiors of pre-existing DM halos the first stars, galaxies and groups and clusters of galaxies started to form (Pagel 2009). At that time the newly formed massive stars and/or compact objects, as quasars, reionized the intergalactic medium (IGM). Cosmic reionization heats the gas very quickly to temperatures close to the ionization of hydrogen. The energy necessary to ionize neutral hydrogen is 13.6 eV or more, corresponding to 91.2 nm, in the ultraviolet (UV). Since then an accumulation of UV radiation remained, which controls the ionized state of the IGM (Gnedin 2010).

The emission of high frequency photoionising photons into the surrounding neutral gas can stop ongoing star formation (MacLachlan et al. 2015). This effect is stronger on halos with masses $\sim 1.2 \times 10^8 M_\odot$ at $z_{reioniz} = 6$. Masses larger than this value are expected to be less affected be reionization effects. Hence, the study of small systems is essential in order to understand the role of reionization in their SFHs. *True fossils* of reionization are considered those galaxies which produced the bulk of stars prior to the reionization epoch, before the suppression of the SF activity (Bovill & Ricotti 2011).

In order to consider a system *affected by reionization* the bulk of SF should be before the reionization epoch. The effect of cosmic reionization is still controversial. Up to now no real trace of reionization has been identified in the SFH of dwarf galaxies (Grebel & Gallagher 2004). An abrupt stop of the star formation would cause a truncation in the metallicity, which is not observed spectroscopically.

Dwarf galaxies of the LG cover a huge variety of characteristics. For this reason a uniform analysis of the SFH of these systems is required in order to on one hand examine all the possible cases, and on the other hand, to understand the relationship between the different galaxies.

The different morphological types of galaxies present in the LG disclose some average characteristic. On average SFH of dSph result exponentially declining, which means that the bulk of SF took place before ∼ 10 Gyr ago. In contrast, dIrrs show a more complex SFH, as they still retain HI . The general trend is an exponential decline prior to 10 Gyr ago, followed by either a constant or a rising SF activity at more recent epochs. UFDs show a behaviour similar to that of dSphs (Tolstoy et al. 2009; Weisz et al. 2014).

1.6 My thesis

In my thesis work, I carried out a photometric study of the four LG dwarf galaxies described in the previous paragraphs, namely NGC 6822, UMi, Draco, and Hercules.

The major aim of my study was to analyse the stellar populations in these four galaxies. In particular, I focused on the presence of radial gradients.

The data were space-based (HST) in the case of NGC 6822 and ground-based (Subaru) in the case of the other three dwarfs. As already stated, these four galaxies cover all the types of galaxies in the LG, as they are respectively a dIrr, two dSphs, and an UFD.

The combination of space- and ground-based photometry applied to galaxies of different morphological types render this study particularly relevant.

The data available are the most complete for these systems. NGC 6822 is located at a relative high distance from the MW, therefore space-based photometry allows to reach deeper magnitudes in its CMD. On the contrary, ground-based telescopes have larger fields of view, which make them particularly suitable for the study of nearby dSphs.

In this manner, I was able to compare and discuss the characteristics of these four dwarf galaxies, to obtain not only details of the single systems but also a general picture of the evolution and formation of the LG.

The thesis is structured as follows. In chapters 2 and 3 a detailed description of the instruments applied, of the datasets used, and of the data analysis techniques is given. In the four upcoming chapters, 5, 7, 6, 8 the stellar population analysis of each dwarf is described. Finally, in chapter 9 the conclusions are given.

Chapter 2

Instruments and Data Sets

In this thesis I have used a set of images acquired by the Advanced Camera for Surveys onboard the Hubble Space Telescope and by the Suprime-Cam at the Subaru telescope. The telescope are presented in Sections 2.1 and 2.2, whereas the data sets are presented in Section 2.3.

2.1 The Hubble Space Telescope

The Hubble Space Telescope (HST) is based on a cooperative program between the European Space Agency (ESA) and the American National Aeronautics and Space Administration (NASA). The HST is a space-based telescope which was located in low-Earth orbit (600 kilometers) on April 25, 1990. Since that date, NASA has planned on regular servicing missions to accomplish the goal of maintaining the HST a long-term mission.

Clearly HST is not limited by the atmosphere of the Earth. Thus, it can produce high resolution images and spectra of astronomical objects. Even though new-generation ground-based telescopes equipped with systems of adaptive optics have largely increased their capabilities in terms of spatial resolution, HST and space telescopes in general, still show unsurpassed characteristics. In addition, space-based telescopes remain unique in the detection of ultraviolet and infrared radiation, in the opaque windows of the Earth's atmosphere.

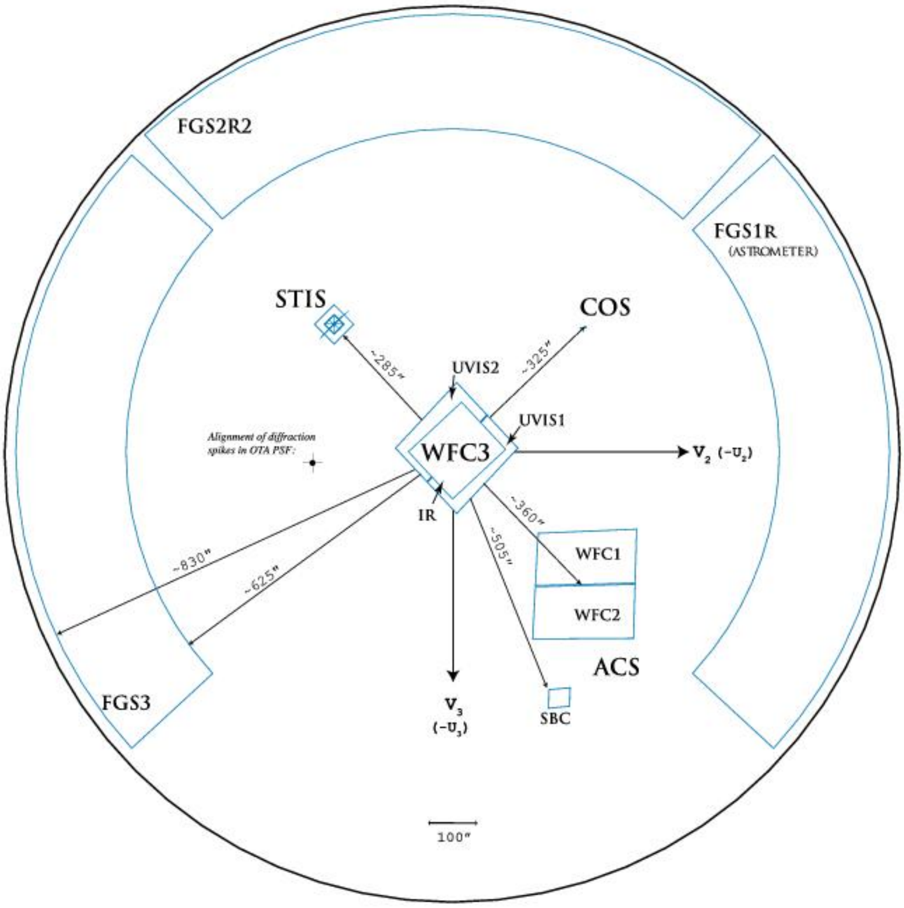

Figure 2.1: Hubble Space Telescope field of view with the onboard instruments indicated.

HST is a Ritchey-Chretien Cassegrain telescope whose aperture is $2.4m$ with a focal ratio of $f/24$. The wavelengths coverage is from $110nm$ to $3\mu m$.

The Field of View (FoV) of the the telescope is shown in Fig. 2.1. At present there are three cameras, two spectrographs, and fine guidance sensors on board of the spacecraft (Ubeda et al. 2011):

- ACS: Advanced Camera for Surveys; it will be analyzed in Section 2.1.1.

- COS: Cosmic Origins Spectrograph. COS is a fourth-generation instrument that was installed on HST during the 2009 servicing mission. COS is designed to perform high sensitivity, moderate- and low-resolution spectroscopy of astronomical objects in the $115 - 320nm$ wavelength range;

- FGS: The Fine Guidance Sensors. FGS provide HST observers with the capability of precision astrometry and milliarcsecond resolution over a wide range of magnitudes (3 ¡ V ¡ 16.8);
- NICMOS: Near Infrared Camera and Multi Object Spectrometer. NICMOS is an HST instrument providing the capability for infrared imaging and spectroscopic observations of astronomical targets. NICMOS detects light with wavelengths between 0.8 and $2.5\mu m$
- STIS: Space Telescope Imaging Spectrograph. STIS can study these objects across a spectral range from $115nm$ to $1000nm$ (from UV to visible and near-IR);
- WFC3: Wide Field Camera 3. WFC3 is a fourth generation instrument that was installed during the 2009 servicing mission. WFC3 provides wide-field imaging with continuous spectral coverage from the ultraviolet to the infrared. WFC3 has two camera channels: the UVIS channel that operates in the ultraviolet and visible bands (from about 200 to $1000nm$), and the IR channel that operates in the infrared (from 900 to $1700nm$). The performance of the two channels was designed to complement the performance of the ACS.

2.1.1 The Advanced Camera for Surveys

The Advanced Camera for Surveys (ACS) is a third generation instrument, installed in March 2002. Its primary purpose was to increase HST imaging discovery efficiency. ACS has three independent cameras (Ubeda & et al. 2011):

- HRC: High Resolution Channel. The HRC has a 1024×1024 CCD, with $21 \times 21 \mu\ mpixels$ that provided $0.028 \times 0.025 arcsec/pixel$ spatial

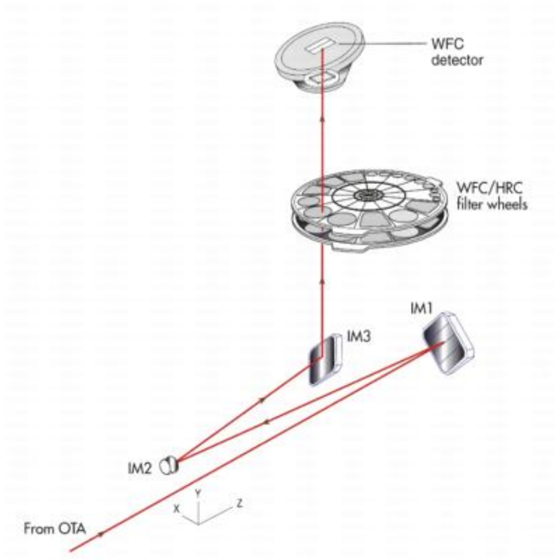

Figure 2.2: ACS Wide Field Channel optical design.

resolution with critical sampling at 6300 Å. This gave the HRC a $29 \times 26 arcsec$ FoV. The spectral response of the HRC ranged from 1700 Å to 11000 Å, and it has a peak efficiency of 29% at 6500 Å. HRC is no longer operational.

- SBC: Solar Blind Channel. The SBC detector is a solar-blind CsI microchannel plate with Multi-Anode Microchannel Array (MAMA) readout. It has $1024 \times 1024 pixels$, each 25×25 μm in size. This provides a spatial resolution of 0.034×0.030 $arcsec/pixel$, producing a FoV of 34.6×30.1 arcseconds. The SBC UV spectral response ranges from 1150 Å to 1700 Å with a peak efficiency of 7.5% at 1250 Å.

- WFC: Wide Field Channel. The WFC employs a mosaic of two 4096×2048 CCDs (WFC1 & WFC2). The 15×15 μm CCDs provide 0.05 $arcsec/pixel$ spatial resolution, with critical sampling at 11600 Å, resulting in a $202 \times 202 arcsec$ FoV. The spectral sensitivity of the WFC ranges from 3500 Å to 11000 Å, with a peak efficiency of 48% at 7000 Å.

I have used data coming from the WFC of the ACS, whose design is shown in Fig. 2.2. The optical design of the camera introduces a two-

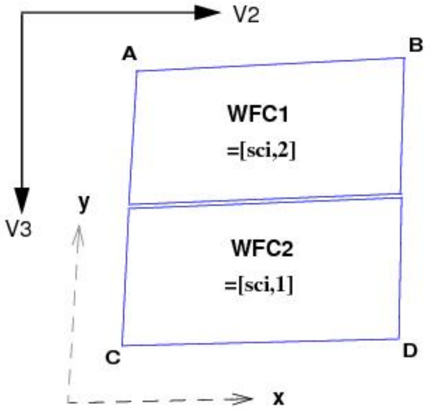

Figure 2.3: WFC splitting in WFC1 and WFC2. Comparison between the axis (V2,V3) and (X,Y) of the WFC1 and WFC2. The readout amplifiers (A,B,C,D) are indicated.

component geometric distortion (Ubeda & et al. 2011). The first geometrical distortion component is due to the angle at which the detector is placed with respect to the optical axis. This produces an 8% stretching of one pixel diagonal compared to the other. As a result, WFC pixels project on the sky as rhombuses rather than squares. These effects are purely geometrical and are routinely corrected in the ACS data reduction pipeline. The second component of geometric distortion is more complex. This distortion causes up to ±9% variation in the effective pixel area and needs to be taken into account when doing accurate photometry or astrometry as the effective area of the detector pixels varies nonlinearly with field position.

The characteristics of WFC are listed in Tab. 2.1. The detector is a mosaic of two chips (Fig. 2.3 of 4096 × 2048 $pixels^2$, each with its own full well capacity and dark current. The values in the table are the average for WFC1 and WFC2. Each chip has two amplifiers; the values of gain and read noise in Tab. 2.1 is the average between the amplifiers.

WFC filter (F435W, F475W, F555W, F606W, and F814W) spectral sensitivity is shown in the top panel of Fig. 2.4, where the wavelength is in Å. In the bottom panel of the same figure the standard Johnson filters as function of the wavelength are plotted in order to show the difference between WFC

Table 2.1: Instrumental characteristics of the WFC HST, of the Suprime-Cam Subaru, CAMELOT IAC80, and ALFOSC NOT.

	WFC	Suprime-Cam
Telescope	HST	Subaru
FoV	202” × 202”	$34' \times 27'$
Pixel Scale	0.05”/pixel	0.2”/pixel
Pixel Size	$15 \times 15\mu$m	$15 \times 15\mu$m
Number of CCDs	2	5 × 2
Image Format	4096 × 2048pixels	2048 × 4096pixels
Spectral Response	3500 Å to 11000 Å	3500 Å to 10500
Detector Efficiency	83% at 6000 Å	95% at 6500 Å
Gain	$1.953 - 2.014e^-$/DN	$2.5 - 3.7e^-$/DN
Read Noise	$4.24e^-$	$10e^-$
Dark Current	$0.0062e^-$/s/pixel	$2 - 3e^-$/pixel/hr
Full Well	$84\ 700e^-$	$150\ 000e^-$
Operating Temperature	−81°C	−110°C
	CAMELOT	ALFOSC
Telescope	IAC80	NOT
FoV	$10.4' \times 10.4'$	$6.4' \times 6.4'$
Pixel Scale		0.19”/pixel
Pixel Size	$13.5 \times 13.5\mu$m	$13.5 \times 13.5\mu$m
Number of CCDs	1	1
Image Format	2148 × 2048pixels	2148 × 2048pixels
Spectral Response	3500 Å to 10500 Å	3340 Å to 10600 Å
Detector Efficiency	83% at 5000 Å	88% at 5500 Å
Gain	$1.25e^-$/DN	$0.33e^-$/DN
Read Noise	$3.71e^-$	$4.2e^-$
Dark Current	$0.0003e^-$/s/pixel	$0.4e^-$/pixel/hr
Full Well	$65\ 000e^-$	$60\ 000e^-$
Operating Temperature	−105°C	−120°C

wide filters and the standard ones. In particular, the Subaru data analyzed here are in the latter photometric system.

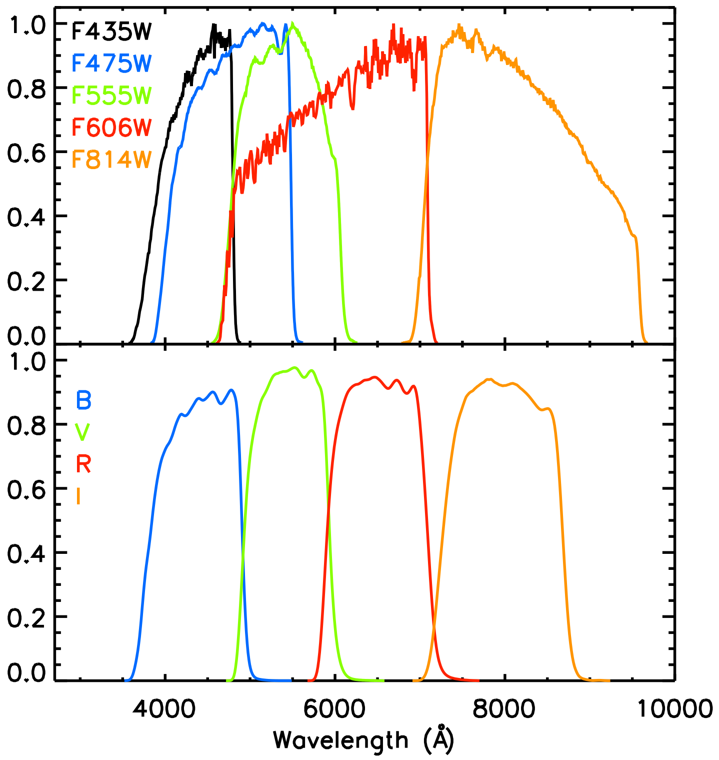

Figure 2.4: Comparison between the transmission curves between WFC filters (*top panel*) and standard Johnson-Cousins filters (*bottom panel*), as those of the Subaru.

2.2 The Subaru Telescope

The Subaru telescope is located at the summit of Mauna Kea, Hawaii, USA and it is operated by the National Astronomical Observatory of Japan (NOAJ).

Ground-based telescopes, like Subaru, are limited by the presence of the Earth's atmosphere, which absorbs and scatters incident electromagnetic radiation. The atmosphere is opaque at all the wavelengths with the exception of windows in the visible, near-infrared, and radio. In addition, the atmosphere disturbs the incoming waves through turbulent air motion, which in turn limits the angular resolution of the telescope (McLean 2008).

When the waves emitted from a distant, point-like source arrive at the

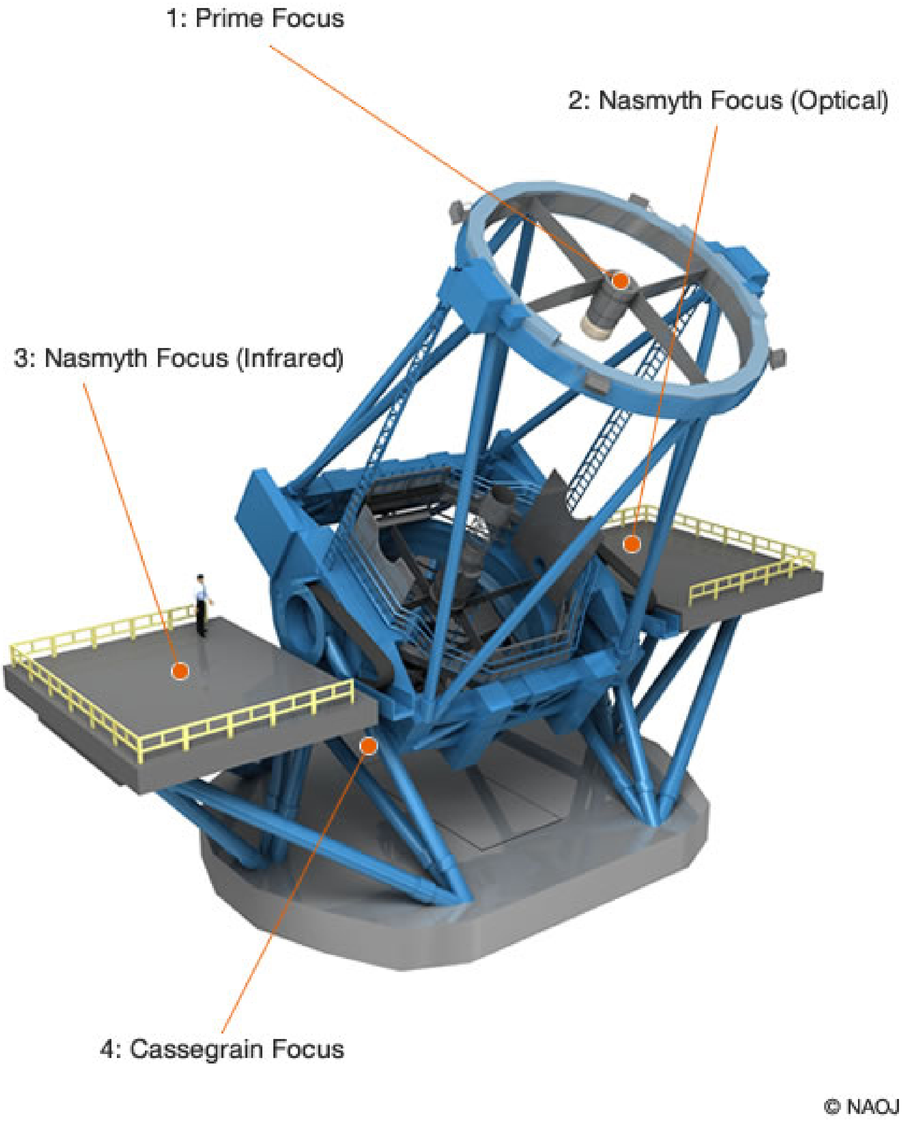

Figure 2.5: Subaru Telescope. The four foci are indicated.

Earth, they are essentially flat and parallel to each other. The moving cells of air in the atmosphere distort the incident wavefront. Each patch of air has a different refraction index, which acts like a lens. Because of diffraction through these lenses the rays are no longer parallel and the wavefront no longer flat. As a consequence, the point-like source results in an extended source when observed from ground. This effect is called *seeing* (McLean 2008).

The best *seeing* conditions are found at the top of mountains on islands, such as Mauna Kea. In order to minimize the effect of atmospheric seeing, adaptive optics systems were developed in the 1990s. An adaptive optics (AO) system is designed to compensate for the random wandering of the centre of the seeing disk by using a deformable mirror. In particular it detects the wavefront distortions very rapidly and it is able to modify the figure of the deformable mirror to compensate for the distortion. The deformable mirror is placed between the telescope focal plane and the instrument. The efficiency of AO is so high that it performs ground-based observations whose photometric limit approaches that of space-based ones (McLean 2008).

The construction of the Subaru telescope ended in 1998 and its First Light for scientific observations took place in January 1999. It represents a new generation in telescope design thanks both to the dimension of the primary mirror and to the various revolutionary technologies used. An AO system that maintains an unprecedentedly high mirror surface accuracy, a new enclosure design to suppress local atmospheric turbulence, an extremely accurate tracking mechanism using magnetic driving systems, seven observational instruments installed at the four foci are just some of the unique features associated with this telescope (Miyazaki et al. 2002).

The Subaru telescope is a Ritchey-Chretien Cassegrain telescope with a primary mirror of 8.2 m with a focal ratio of f/1.83. It has four foci, one for each mirror, as shown in Fig. 2.5.

A wide variety of instruments are available for this telescope:

- AO188: Subaru 188-elements Adaptive Optics system, which delivers diffraction-limited images in the near-infrared.
- COMICS: Cooled Mid-Infrared Camera and Spectrograph provides imaging and spectroscopy from 8-25 microns.
- FMOS: Fiber Multi Object Spectrograph provides fiber-fed multi-object

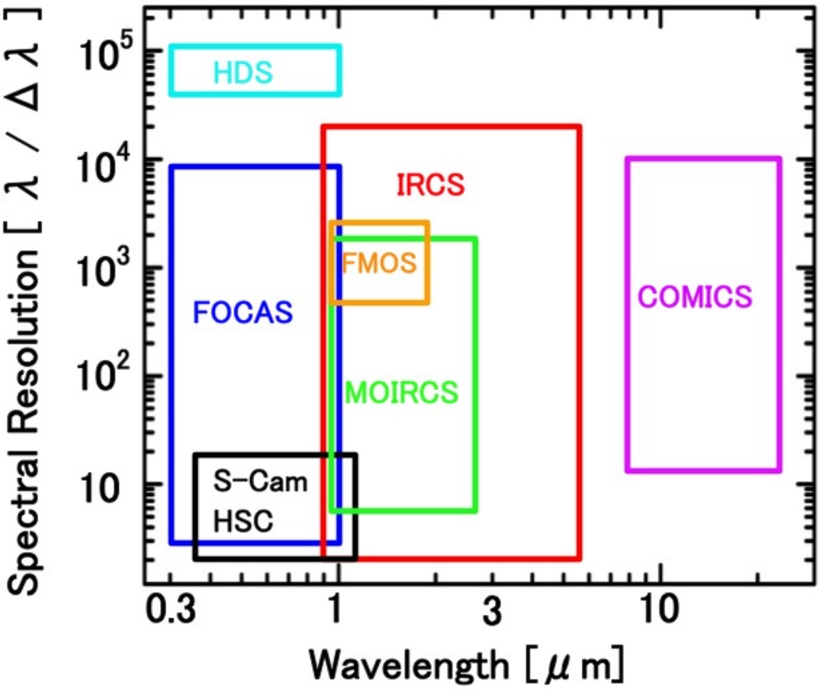

Figure 2.6: Schematic plot of the instruments at the Subaru telescope.

spectroscopy from 0.9-1.8 microns over a 30 arcmin field of view.

- FOCAS: Faint Object Camera And Spectrograph provides optical imaging and long-slit and multi-slit spectroscopy over a 6 arcmin field of view.

- HDS: High Dispersion Spectrograph provides extremely high-resolution optical spectroscopy.

- IRCS: Infrared Camera and Spectrograph provides imaging from 0.9-5.5 microns, and low-resolution and echelle spectroscopy over the same range.

- MOIRCS: Multi-Object Infrared Camera and Spectrograph provides imaging and low-resolution spectroscopy from 0.9-2.5 microns over a 4 arcmin× 7 arcmin field of view.

- Suprime-Cam: Subaru Prime Focus Camera provides optical imaging over a large field of view with a mosaic of CCDs. This instrument is going to be thoroughly discussed in Section 2.2.1.

- HSC: Hyper Suprime-Cam provides optical imaging over a very large field of view (1.5 degree diameter) with a mosaic of CCDs.

These are placed in a plane spectral resolution vs. wavelength in Fig. 2.6. As already mentioned, I used data acquired with the Suprime-Cam in my thesis.

2.2.1 Suprime-Cam

The **Su**baru **Prime** Focus **Cam**era (Suprime-Cam, (Miyazaki et al. 2002) is a mosaic of ten 2048×4096 $pixels^2$ CCDs (Fig. 2.7), located at the prime focus of the Subaru Telescope, which covers a $34' \times 27'$ field of view with a pixel scale of 0.20".

In 2008 the CCDs of the camera were changed. The new CCDs maintained the same dimension and a 5×2 disposition. The new CCDs allow twice the sensitivity at a wavelength of 1 micron.

A list of the specifications of this instrument can be found in Table 2.1. It is clear that compared to the WFC the Suprime-Cam has a much wider f.o.v. Thanks to this feature it is particularly suitable for the study of very extended objects, such as nearby dwarf galaxies.

The ACS on board of the HST has indeed a much higher image quality (0.05"), which cannot be obtained from the ground. However, computations and simulations show that the Suprime-Cam with a higher integration time can reach the same photometric limit as the ACS, but with a lower spatial resolution (Miyazaki et al. 2002).

Two filter sets are adopted for this camera, the Johnson-Cousin (Johnson & Morgan 1953; Cousins 1978; Bessell 1990) and the SDSS system. In Fig. 2.4, bottom panel, the filter transmittance curves are shown.

Generally a science exposure consists in one image, which is obtained by stacking several images. This is not a trivial operation because of the large

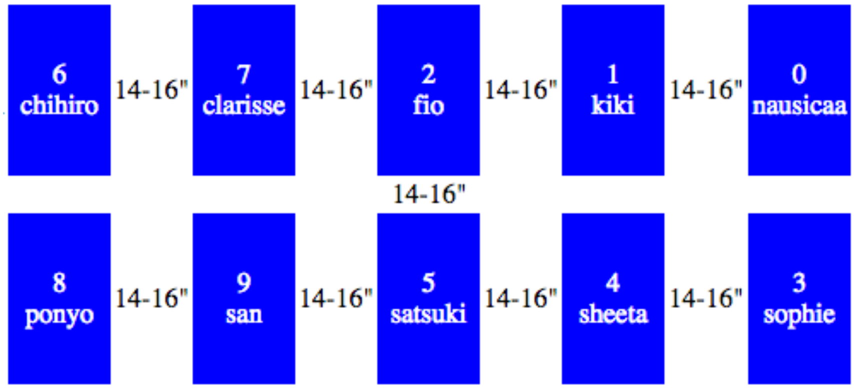

Figure 2.7: Schematic plot of the 10 CCDs of the Suprime-Cam. The total field of view covered by the 10 CCDs is $34' \times 27'$.

distortion of the optics. To take into account the distortion a 4-th grade polynomial function is needed. The distortion is accurately determined in the stacking procedure.

Three of the galaxies studied here were observed with the Suprime-Cam.

2.3 Data Sets

2.3.1 HST dataset

The HST data I used for my thesis are for the dIrr NGC 6822. They consist of two exposures, in the F475W and in the F814W HST filters respectively, in six areas which cover the whole main body of this galaxy, as shown in Fig. 2.8. Name, filter, exposure time in seconds, coordinates α (h) and δ (deg), and date of each exposure are listed in Tab. 2.2.

The images were fully calibrated and flat-fielded, but they were not *drizzled*, therefore they were not corrected for the geometric distortion effect. Thus, applying the required correction for distortion was the first step of my data analysis (Section 3.1).

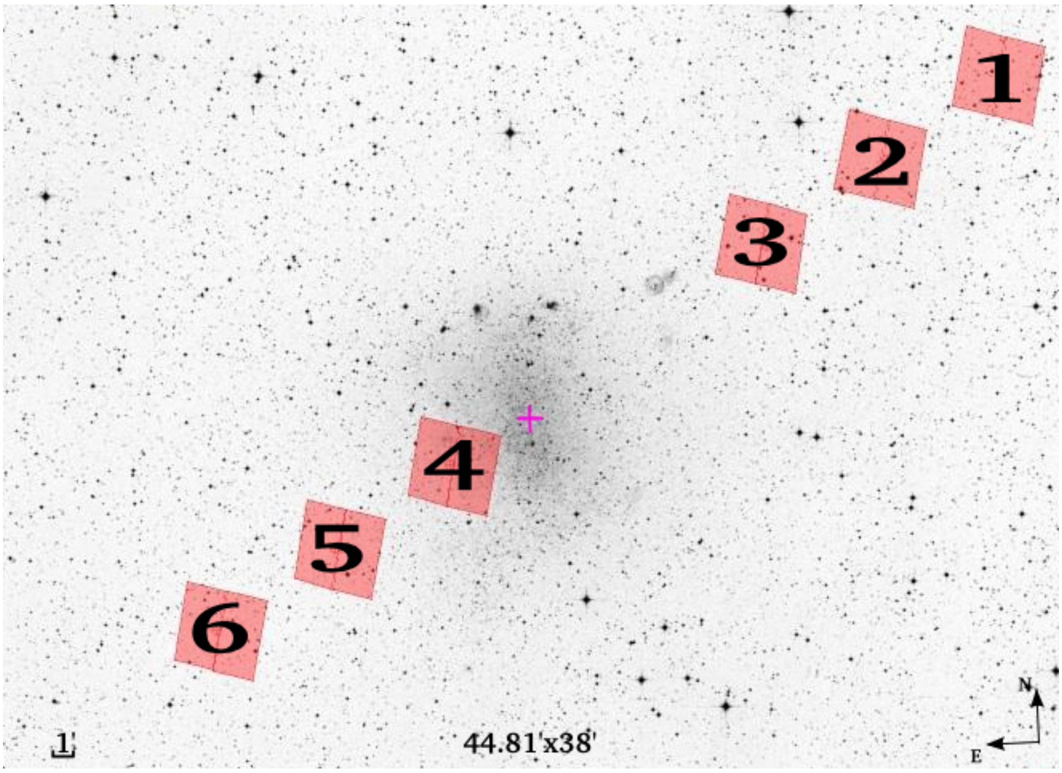

Figure 2.8: In red ACS footprints of the fields in NGC 6822. The violet cross indicates the center of the galaxy.

2.3.2 Subaru dataset

The Subaru data I used in my thesis are for UMi, Draco, and Hercules dwarf galaxies. They consist of a different number of fields for each galaxy , which were observed in two photometric bands: V and I.

The field of view of all the Subaru images is $34' \times 27'$, which allows to cover a significant fraction of the galaxies studied.

Tables 2.3 and 2.4 summarise the details of the observations. In the tables the names of the galaxy, the number of the fields, the photometric bands, the exposure time, the number of images, the seeing, the airmass, the coordinates and date of observation are indicated. The exposure time is a total exposure time of the number of stacked images. This is indicated in the fifth column of the table. For example, if the total exposure time is 2400 s and the number of images is 10, this means that 10 images of 240 s were

Table 2.2: List of the images in the three fields, with filter, exposure time (s), α (h), δ (deg).

Field	Filter	Exp. time (s)	α (h)	δ (deg)	Date (yy-mm-dd)
Field 1	F475W	423.0	19.726	-14.561	2011-03-28
Field 1	F475W	463.0	19.726	-14.561	2011-03-28
Field 1	F814W	883.0	19.726	-14.561	2011-03-28
Field 1	F814W	463.0	19.726	-14.561	2011-03-28
Field 2	F475W	559.5	19.732	-14.619	2011-03-28
Field 2	F475W	559.5	19.732	-14.619	2011-03-28
Field 2	F814W	559.0	19.732	-14.619	2011-03-28
Field 2	F814W	559.0	19.732	-14.619	2011-03-28
Field 3	F475W	559.5	19.738	-14.678	2011-03-29
Field 3	F475W	559.5	19.738	-14.678	2011-03-29
Field 3	F814W	559.0	19.738	-14.678	2011-03-29
Field 3	F814W	559.0	19.738	-14.678	2011-03-29
Field 4	F475W	559.5	19.753	-14.829	2010-10-22
Field 4	F475W	559.5	19.753	-14.829	2010-10-22
Field 4	F814W	559.0	19.753	-14.829	2010-10-22
Field 4	F814W	559.0	19.753	-14.829	2010-10-22
Field 5	F475W	559.5	19.758	-14.887	2010-10-22
Field 5	F475W	559.5	19.758	-14.887	2010-10-22
Field 5	F814W	559.0	19.758	-14.887	2010-10-22
Field 5	F814W	559.0	19.758	-14.887	2010-10-22
Field 6	F475W	423.0	19.764	-14.943	2010-10-22
Field 6	F475W	463.0	19.764	-14.943	2010-10-22
Field 6	F814W	883.0	19.764	-14.943	2010-10-22
Field 6	F814W	463.0	19.764	-14.943	2010-10-22

stacked together in order to obtain the final one.

The fields are shown in Fig. 2.9, 2.10, 2.11 for Draco, UMi, and Hercules respectively.

The data needed to be pre-reduced and it is discussed in Section 3.1.2.

2.3.3 IAC80 dataset

The standard fields observed during the nights listed in Table 2.4 do not allow to perform an accurate calibration of the data (see Appendix B). Hence,

Table 2.3: Subaru dataset. List of the images for Draco (Dra), with the associated fields, filter, total exposure time (s), number of images, seeing, airmass, α (h), δ (deg) in J2000 reference system, and date of the observations.

dSph	Field	Filter	Exp. time (s)	Image No.	Seeing ($'$)	Airmass	α [hh:mm:ss]	δ [deg:mm:ss]	Date
Dra	1	I	2400	10	0.62	1.271	17:20:19.651	+57:55:10.64	06/08/2005
Dra	1	V	1500	5	0.56	1.284	17:20:19.651	+57:55:10.64	06/08/2005
Dra	2	I	2800	14	1.08	1.438	17:24:16.333	+57:54:57.16	04/04/2008
Dra	2	V	600	5	1.26	1.605	17:24:16.333	+57:54:57.16	04/04/2008
Dra	3	I	3000	15	0.81	1.302	17:16:24.826	+57:54:57.41	04/04/2008
Dra	3	V	600	5	1.18	1.506	17:16:24.826	+57:54:57.41	04/04/2008
Dra	4	I	3000	15	0.72	1.649	17:20:19.742	+58:19:32.23	03/04/2008
Dra	4	V	600	5	0.78	1.285	17:20:19.742	+58:19:32.23	03/04/2008
Dra	5	I	3800	19	0.98	1.263	17:20:19.554	+57:31:10.86	04/04/2008
Dra	5	V	600	5	1.02	1.386	17:20:19.554	+57:31:10.86	05/04/2008
Dra	F	I	3000	15	0.78	1.442	17:20:19.836	+58:43:40.51	03/04/2008
Dra	F	V	600	5	1.06	1.285	17:20:19.836	+58:43:40.51	03/04/2008
Dra	1	I	30	3	0.70	1.693	17:20:19.651	+57:55:10.64	03/04/2008
Dra	1	V	30	3	0.74	1.283	17:20:19.651	+57:55:10.64	03/04/2008
Dra	2	I	30	3	1.00	1.456	17:24:16.333	+57:54:57.16	04/04/2008
Dra	2	V	30	3	1.28	1.629	17:24:16.333	+57:54:57.16	04/04/2008
Dra	3	I	30	3	0.78	1.309	17:16:24.826	+57:54:57.41	04/04/2008
Dra	3	V	30	3	1.16	1.525	17:16:24.826	+57:54:57.41	04/04/2008
Dra	4	I	30	3	0.68	1.681	17:20:19.742	+58:19:32.23	03/04/2008
Dra	4	V	30	3	0.92	1.288	17:20:19.742	+58:19:32.23	03/04/2008
Dra	5	I	30	3	0.76	1.263	17:20:19.554	+57:31:10.86	04/04/2008
Dra	5	V	30	3	1.10	1.400	17:20:19.554	+57:31:10.86	05/04/2008
Dra	F	I	30	3	0.80	1.425	17:20:19.836	+58:43:40.51	03/04/2008
Dra	F	V	30	3	0.92	1.287	17:20:19.836	+58:43:40.51	03/04/2008

Table 2.4: Subaru dataset. List of the images for UMi and Hercules (Her), with the associated fields, filter, total exposure time (s), number of images, seeing, airmass, α, δ in J2000 reference system, and date of the observations.

dSph	Field	Filter	Exp. time (s)	Image No.	Seeing ($'$)	Airmass	α [hh:mm:ss]	δ [deg:mm:ss]	Date
UMi	1	I	2400	10	0.70	1.571	15:09:10.466	+67:13:54.78	05/08/2005
UMi	1	V	1100	5	1.22	1.876	15:09:10.466	+67:13:54.78	04/08/2005
UMi	2	I	2400	10		1.671	15:11:38.720	+66:58:11.52	23/08/2009
UMi	2	V	1100	5		1.877	15:11:38.720	+66:58:11.52	23/08/2009
UMi	1	I	30	3	0.68	1.650	15:09:10.466	+67:13:54.78	03/04/2008
UMi	1	V	30	3	0.98	1.675	15:09:10.466	+67:13:54.78	03/04/2008
UMi	2	I	30	3	0.92	1.626	15:11:38.720	+66:58:11.52	05/04/2008
UMi	2	V	30	3	1.24	1.677	15:11:38.720	+66:58:11.52	05/04/2008
Her	1	I	3200	10	0.76	1.612	16:31:05.943	+12:47:45.30	23/08/2009
Her	1	V	1600	5	0.76	1.338	16:31:05.943	+12:47:45.30	23/08/2009
Her	2W	I	3200	10	0.52	1.331	16:29:29.932	+12:47:16.77	23/09/2009
Her	2W	V	1600	5	0.62	1.328	16:29:29.932	+12:47:16.77	24/09/2009
Her	1	I	30	3	0.56	1.276	16:31:05.943	+12:47:45.30	23/09/2009
Her	1	V	30	3	0.70	1.477	16:31:05.943	+12:47:45.30	23/08/2009
Her	2W	I	30	3	0.54	1.295	16:29:29.932	+12:47:16.77	23/09/2009
Her	2W	V	30	3	0.58	1.290	16:29:29.932	+12:47:16.77	24/09/2009

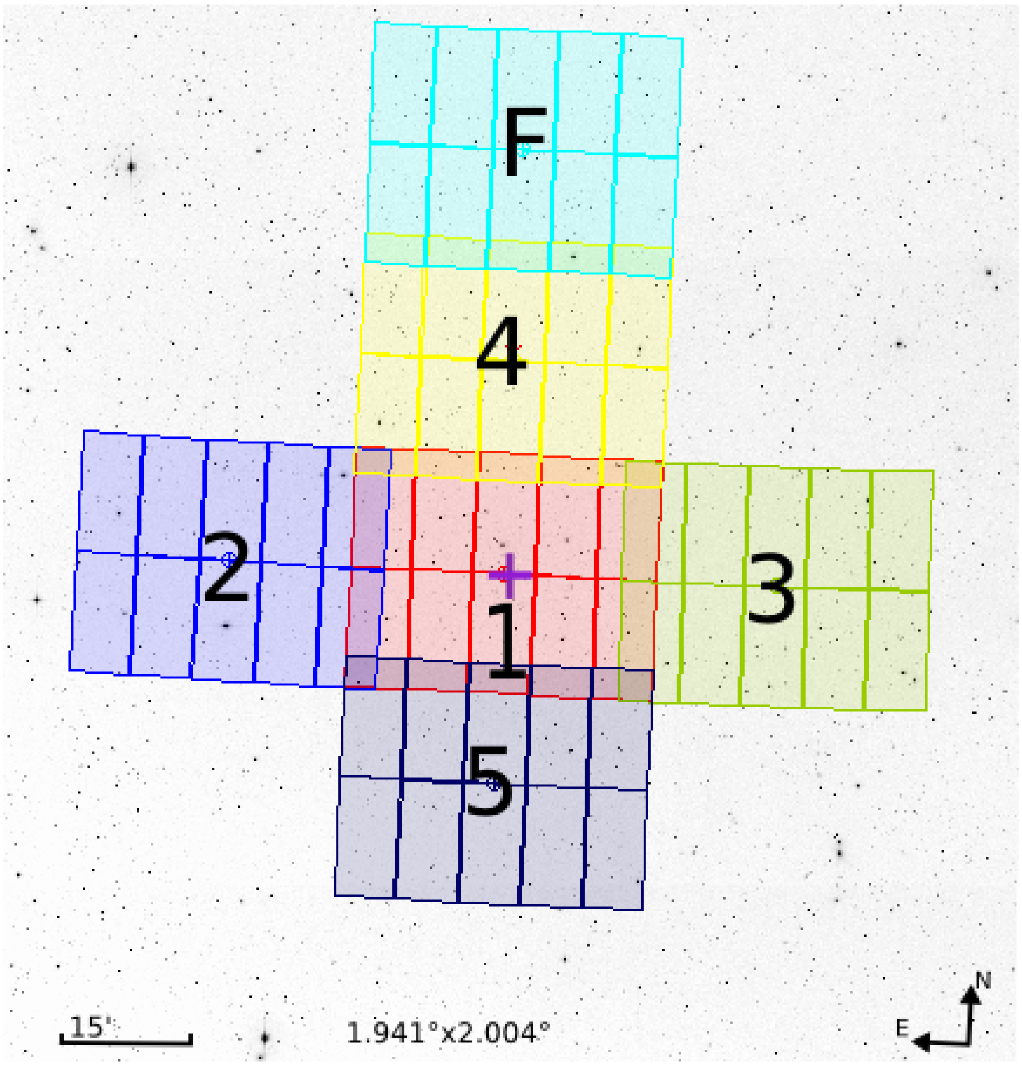

Figure 2.9: DSS image of Draco, with the footprints of the six observed fields. The labels are the same indicated in Table 2.3. More details about the observations are listed in Table 2.3.

I faced the necessity of new observations, which could lead to an accurate calibration of the present data set.

Thus, thanks to the joint PhD programme with the *Universidad de La Laguna*, I obtained one night at the IAC80, the 82 cm Ritchey-Chretien Cassegrain telescope, located at the Teide Observatory in Tenerife.

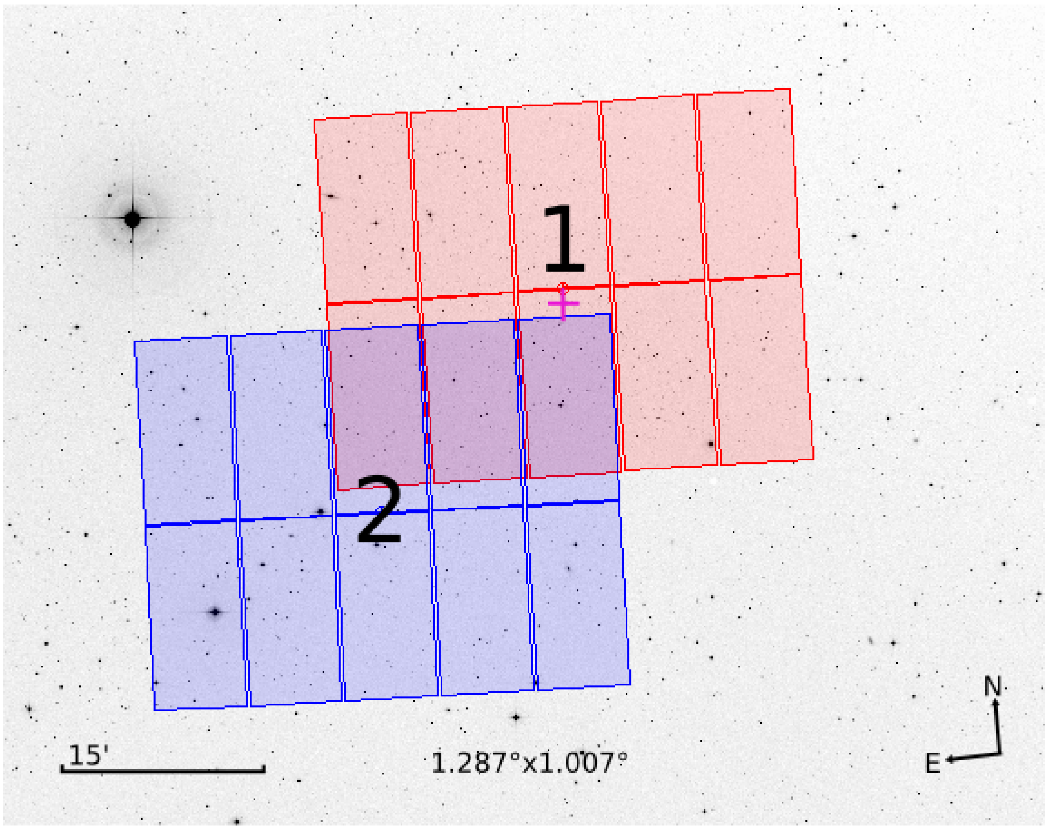

Figure 2.10: DSS image of UMi, with the footprints of the two observed fields. The labels are the same indicated in Table 2.4. More details about the observations are listed in Table 2.4.

The telescope is equipped with the CAMELOT[1] (Zurita 2011; Prieto et al. 2004) camera, whose features are listed in Table 2.1. Thanks to the large field of view, this camera is particularly suitable in performing observations of standard fields.

Given the importance of the issue, I programmed an intense schedule in order to have a huge amount of standards, spanning a wide range in airmass, colour, and magnitude. These standards were used to calibrate the field of programme galaxies, namely UMi and Her.

The observations were performed on the night of January 31st, 2015.

---

[1] All available information about the telescope and instrument can be found at http://www.iac.es/telescopes/pages/en/home/telescopes/IAC80.php and http://www.iac.es/telescopes/pages/en/home/instruments/camelot.php

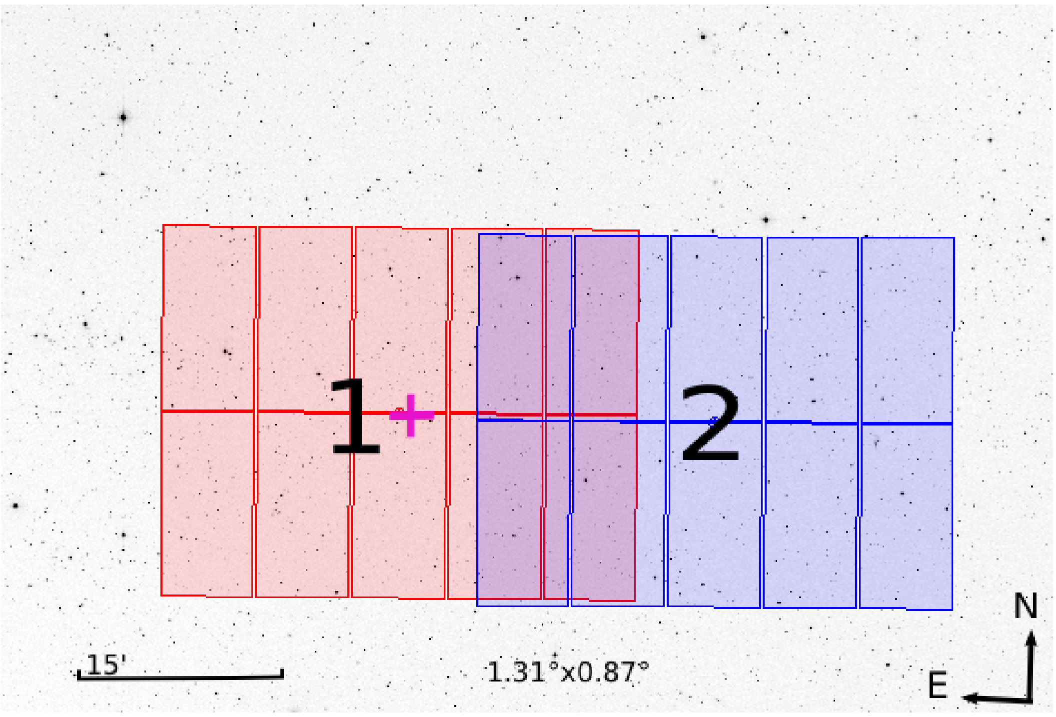

Figure 2.11: DSS image of Hercules, with the footprints of the two fields. The labels are the same indicated in Table 2.4. More details about the observations are listed in Table 2.4.

The list of the observations is presented in Table 2.5. All the standard fields observed belong to the Landolt (1992, 2009) sample, and are accordingly labelled. The fields observed in UMi and Her are labelled as UMI1, UMI2, HER1, HER2. UMI1 and HER1 are both located in the area where Subaru fields 1 and 2 overlap, respectively (Fig. 2.10, 2.11).

Table 2.5: Summary of the observations performed at the IAC80, with the name of the field, α and δ, filter, exposure time, and airmass.

Field	α [hh:mm:ss]	δ [deg:mm:ss]	Filter	Exp. time (s)	Aimrass
SA95	3:55:39	+00:08:24	I	45	1.185
SA95	3:55:40	+00:08:24	I	45	1.193
SA95	3:55:40	+00:08:24	I	120	1.198

Table 2.5: continued

Field	α [hh:mm:ss]	δ [deg:mm:ss]	Filter	Exp. time (s)	Airmass
SA95	3:55:40	+00:08:25	V	50	1.205
SA95	3:55:40	+00:08:25	V	100	1.208
SA95	3:56:01	+00:08:25	V	150	1.213
SA98	6:53:01	−00:23:26	V	5	1.188
SA98	6:53:01	−00:23:26	V	10	1.186
SA98	6:53:01	−00:23:26	V	50	1.185
SA98	6:53:22	−00:23:26	I	5	1.183
SA98	6:53:01	−00:23:25	I	10	1.182
SA98	6:53:01	−00:23:25	I	50	1.181
SA100	8:54:40	−00:39:51	I	20	1.554
SA100	8:54:19	−00:39:50	I	60	1.542
SA100	8:54:19	−00:39:52	V	5	1.528
SA100	8:54:40	−00:39:52	V	50	1.522
SA100	8:54:19	−00:39:52	V	75	1.511
SA95	3:55:20	+00:08:28	I	45	1.451
SA95	3:56:02	+00:08:30	I	45	1.485
SA95	3:55:41	+00:08:30	I	120	1.498
SA95	3:55:42	+00:08:32	V	100	1.517
SA95	3:55:42	+00:08:32	V	150	1.533
SA100	8:54:20	−00:40:02	V	50	1.262
SA100	8:54:20	−00:40:01	V	75	1.258
SA100	8:54:21	−00:40:01	I	20	1.251
SA100	8:54:20	−00:40:01	I	60	1.248
SA98	6:53:03	−00:23:23	I	5	1.153
SA98	6:53:03	−00:23:23	I	10	1.153
SA98	6:53:03	−00:23:23	I	50	1.154
SA98	6:53:24	−00:23:23	V	5	1.155
SA98	6:53:24	−00:23:22	V	10	1.156
SA98	6:53:03	−00:23:22	V	50	1.157
SA100	8:54:22	−00:39:58	I	20	1.147

Table 2.5: continued

Field	α [hh:mm:ss]	δ [deg:mm:ss]	Filter	Exp. time (s)	Airmass
SA100	8:54:21	−00:39:57	I	60	1.146
SA100	8:54:21	−00:39:57	V	50	1.146
SA100	8:54:21	−00:39:57	V	75	1.145
SA103	11:57:36	−00:31:40	I	10	1.638
SA103	11:57:35	−00:31:39	I	30	1.629
SA103	11:57:36	−00:31:39	V	15	1.615
SA103	11:57:36	−00:31:41	V	45	1.606
PG1047	10:50:49	−00:05:02	V	30	1.248
PG1047	10:50:49	−00:05:04	V	30	1.240
PG1047	10:50:50	−00:05:04	V	90	1.236
PG1047	10:50:50	−00:05:03	I	30	1.230
PG1047	10:50:50	−00:05:03	I	120	1.225
SA100	8:54:22	−00:40:06	I	20	1.158
SA100	8:54:44	−00:40:06	I	60	1.158
SA100	8:54:23	−00:40:06	V	50	1.160
SA100	8:54:23	−00:40:06	V	75	1.162
SA98	6:53:27	−00:23:14	V	10	1.643
SA98	6:53:27	−00:23:14	V	50	1.650
SA98	6:53:06	−00:23:14	I	5	1.662
SA98	6:53:06	−00:23:14	I	10	1.668
SA98	6:53:06	−00:23:14	I	50	1.674
PG1047	10:50:49	−00:05:04	I	120	1.155
PG1047	10:50:50	−00:05:04	V	90	1.152
SA103	11:57:16	−00:31:50	V	30	1.258
SA103	11:57:51	−00:31:57	V	30	1.252
SA103	11:57:30	−00:31:59	V	45	1.249
SA103	11:57:30	−00:31:58	I	15	1.245
SA103	11:57:30	−00:31:58	I	30	1.243
SA100	8:54:23	−00:39:59	V	75	1.299
SA100	8:54:24	−00:39:59	V	50	1.305

Table 2.5: continued

Field	α [hh:mm:ss]	δ [deg:mm:ss]	Filter	Exp. time (s)	Airmass
SA100	8:54:45	-00:39:59	I	20	1.309
SA100	8:54:24	-00:39:59	I	60	1.313
PG1323	13:26:59	-08:54:29	I	20	1.372
PG1323	13:26:39	-08:54:29	I	40	1.368
PG1323	13:26:39	-08:54:28	V	60	1.363
PG1323	13:26:39	-08:55:08	V	60	1.264
PG1323	13:26:39	-08:55:08	I	40	1.266
UMI1	15:10:17	+67:02:26	V	60	1.473
UMI1	15:10:17	+67:02:24	V	300	1.467
UMI1	15:10:17	+67:02:23	I	300	1.454
UMI1	15:10:18	+67:02:22	I	40	1.442
UMI2	15:07:48	+67:16:12	I	60	1.432
UMI2	15:07:48	+67:16:10	I	300	1.428
UMI2	15:07:48	+67:16:09	V	300	1.417
UMI2	15:07:49	+67:16:08	V	60	1.393
HER1	16:30:56	+12:40:39	V	80	1.557
HER1	16:30:56	+12:40:39	V	300	1.538
HER1	16:30:56	+12:40:38	I	300	1.500
HER1	16:30:56	+12:40:35	I	30	1.465
HER2	16:32:14	+12:51:58	I	30	1.451
HER2	16:32:14	+12:51:56	I	300	1.445
HER2	16:32:14	+12:51:55	V	300	1.413
HER2	16:32:14	+12:51:54	V	30	1.384

2.3.4 NOT dataset

As widely discussed in chapter 7, the analysis of UMi led to a peculiar result. In particular, the slope of the MS in the CMD appeared to be somewhat redder when compared to theoretical isochrones and HST observations. Hence, I decided to rely on additional observations for calibration. Therefore

Table 2.6: List of the observations performed with ALFOSC on the night of June 20th, 2015, with filter, total exposure time, number of images, α (h), δ (deg), and airmass.

Field	Filter	Exp. time (s)	No.	α [hh:mm:ss]	δ [deg:mm:ss]	Airmass
UMi	V	180	6	15:09:29.5	+67:09:17.0	1.273
UMi	V	1800	3	15:09:29.5	+67:09:17.0	1.274
UMi	I	4000	4	15:09:29.5	+67:09:17.0	1.288
UMi	I	120	4	15:09:29.5	+67:09:17.0	1.356

I requested time at the NOT telescope, in order to investigate more about this discrepancy.

The Nordic Optical Telescope (NOT) is a 2.5m Ritchey-Chretien Cassegrain telescope, located at the *Observatorio del Roque de los Muchachos*, in La Palma, Canarias, Spain.

For this purpose, I applied for two hours of observation using the ALFOSC[2] camera in one field of UMi. The details of this camera are listed in Table 2.1. I chose the total exposure time in order to reach $I \sim 23.3$ and $V \sim 24.3$ with a signal-to-noise ratio of ~ 10.

The observations were performed on the night of June 20th, 2015, in service mode. I did not request any standard observations as the field observed overlaps with those observed with the IAC80. In addition, I chose the field located in the region where the two fields of UMi overlap, as shown in Fig. 2.10. The list of observations can be found in Table 2.3.4. According to the standard procedure flat field and bias images were also provided.

---

[2] All information on the telescope and camera are available at http://www.not.iac.es/general/ and http://www.not.iac.es/instruments/alfosc/.

Chapter 3

Data Analysis

A brief analysis of the pre-reduction processes can be found in Section 3.1. There are several software packages to perform photometry in crowded fields. In my thesis I have used DAOPHOT. The data reduction is presented in Section 3.2.

3.1 Pre-reduction Processes

3.1.1 HST Pre-reduction

The HST data were prereduced by the HST team, using the CALACS pipeline. This standard prereduction process can be summarized by the following equation:

$$FLTIMAGE_{i,j} = \frac{RAWIMAGE_{i,j} - BIAS_{i,j} - DARK_{i,j}}{FLATFIELD_{i,j}} \tag{3.1}$$

The BIAS and DARK have been subtracted according to the standard procedure. The result is normalized for the FLAT FIELD

As mentioned in Section 2.1.1, a geometrical distortion arises because of the instrument position on the f.o.v. All in all the effect of this geometrical distortion is equivalent to modify the geometry and pixel size, affecting therefore the photometry. The map of the geometrical distortion is shown in

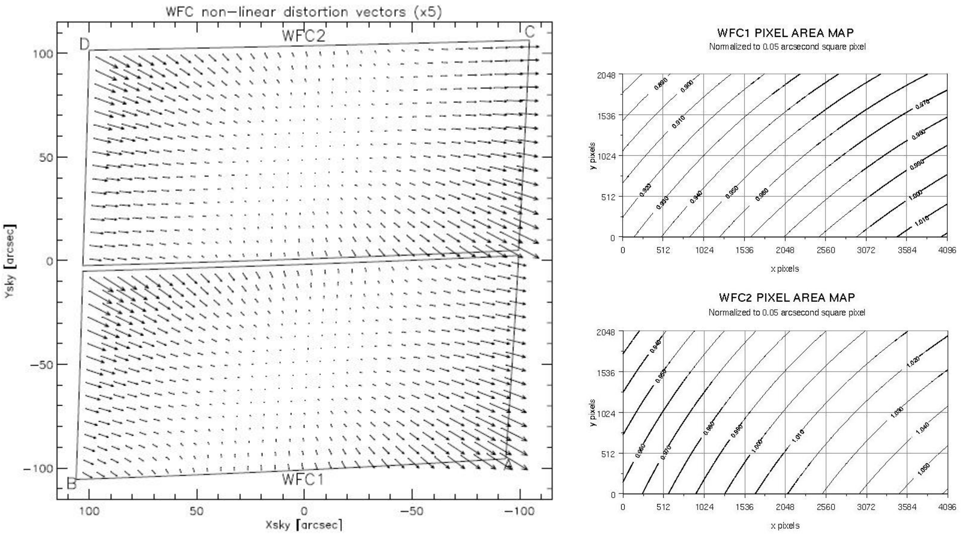

Figure 3.1: *Left Panel:* ACS WFC geometrical distortion map. *Right Panel:* Pixel Area Map (PAM) for WFC1 (up) and WFC2 (down). I multiplied these corrections by the original images.

Fig. 3.1 left. To correct for this effect I multiplied the measured flux on the FLT image by the pixel area at the corresponding position. The Pixel Area Maps (PAM) for WFC1 and WFC2 are shown in the *right-hand panel* Fig. 3.1.

3.1.2 Subaru Pre-reduction

As in the case of the HST data, a standard reduction package is also available in the case of the Subaru. Hence, the original images were processed using this package, called SDFRED[1]. This package allows to semi- or fully-automatically reduce the immense data output from Suprime-Cam, merging together a number of initial images. These are listed in Table 2.4 for every galaxy. Suprime-Cam is composed of 10 chips. For each chip, the number of images listed in Table 2.3 and 2.4 were available and they are slightly shifted and/or rotated in order to create a continuous unique image, which avoids gaps.

---

[1] Full guide to the pipeline: subarutelescope.org/Observing/Instruments/SCam/sdfred/v2.0/sdfred2_2p1ae.pdf

SDFRED pipeline can be summarized by Equation 3.1, and its standard execution works as follows:

1. the files are renamed, identifying both the set of the image and the chip;
2. overscan and bias are subtracted;
3. the flat field images are averaged, in order to obtain a master flat. Then the flat fielding is performed on the object images;
4. distortions and atmospheric dispersion are corrected;
5. the PSF is measured in every image. This is needed to co-add the images;
6. the PSF size is equalized and it is matched between all the images;
7. the sky contribution is subtracted in the single images;
8. bad pixels are identified and excluded;
9. the alignement and scaling between the images is determined;
10. in the end, all the images are combined through a clipped mean algorithm. A clipped mean algorithm considers the same pixels on all the images but ignores the highest and lowest value (or values) found.

This process is carried out for each filter in each field and each exposure.

3.1.3 IAC80 and NOT Pre-reduction

The pre-reduction in the case of the data acquired with these two telescopes was made according Equation 3.1.

The IAC80 data were pre-reduced during the same night of the observation by the support astronomer, using a pipeline specifically developed for this telescope. The pipeline at first subtracts overscan and bias from all the images, and then it created a master flat for every filter. Finally, the images with the objects are corrected for the associated flat field, to obtain the scientific images.

The NOT telescope does not provide any pre-reduction pipeline. Therefore I performed the single steps of the pre-reduction using IRAF. As in all the previous cases the first step was to subtract the bias from all the images. Then I averaged all the flat fields, in order to obtain a master flat for every filter. Then, the images were divided by the master flat.

The final step was to average all the images for the V filter, to obtain one final image for every exposure, i.e. long and short. In addition, for the I images I needed to remove the fringe pattern, which is very strong in the I band images acquired with this telescope, as shown in Fig. 3.2. Fringe is caused by multiple reflections of the interacting photon inside the CCD, and it affects more I than V photons.

This effect can be corrected using specific IRAF pipelines, provided that the images were taken with a small dithering. Using the single long exposure images and the specific IRAF pipeline I created a fringe mask, which I subtracted from all the images. The result was satisfactory, as shown in Fig. 3.2. Once I corrected the fringe pattern in all the I images, I averaged them to obtain one final image for every exposure, as in the case of the V band.

3.2 Data Reduction

The data reduction of the images has been done using DAOPHOT (Stetson 1987) and its companion packages ALLSTAR and ALLFRAME (Stetson 1994). DAOPHOT is a package for stellar photometry and astrometry developed to deal with crowded fields. It was developed by Peter B. Stetson at the Dominion Astronomical Observatory (DAO), and it is now available as "DAOPHOT II: The Next Generation". DAOPHOT identifies the brightness peaks in the frame, performs synthetic aperture photometry, and tries to estimate an accurate PSF.

According to Stetson (2000b), a typical DAOPHOT run in a crowded

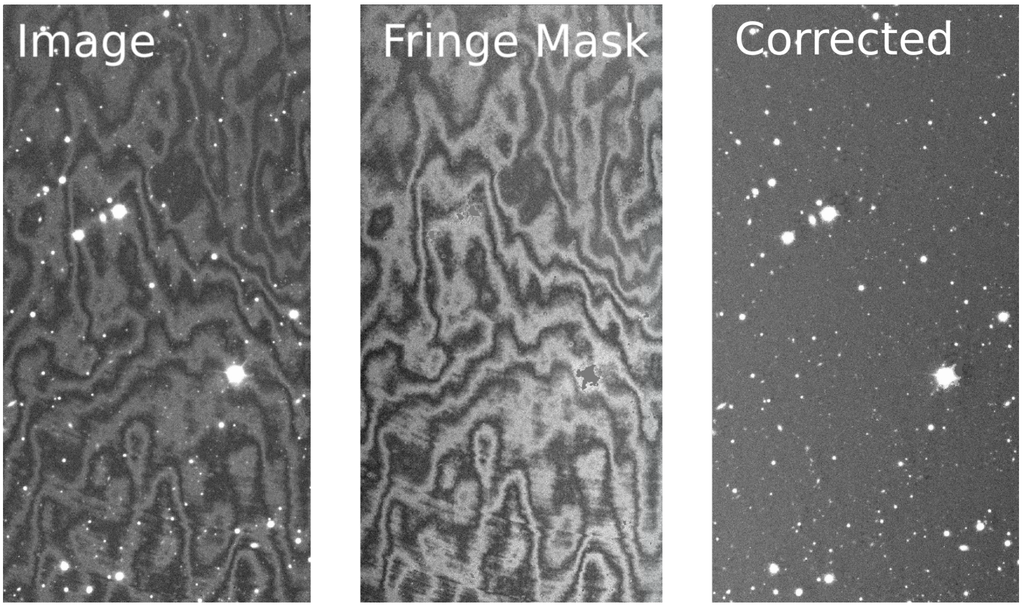

Figure 3.2: Example for the fringe pattern correction for one image in the I band. *Left panel:* original image in the I band, corrected for bias and flat field. The fringe pattern is clearly visible in the image. *Middle panel:* evaluation of the fringe contribution using the set of images in the I band together with IRAF routines. *Right panel:* same image as in the *left panel* after applying the fringe correction. The result appears satisfactory. Using the same fringe mask all I images were corrected.

field can be summarized as follows (in the following the parameter's name and DAOPHOT commands are in capital letters):

- **Sky determination** (FIND). The average sky brightness is determined by the modal value in the sky annulus, whose radius is set by the user. The program provides also the the standard deviations of the sky luminosity so estimated. The sky luminosity is then subtracted during the phase of photometry of the stars.
- **Stellar sources identification** (FIND). After having determined the luminosity of the sky the image is scanned pixel by pixel and the peaks of luminosity are detected at the confidence level selected by the user. The star detection threshold is set according to the gain and readout noise of the detector.

- **Aperture Photometry** (PHOT). The first step is to set the radii of the apertures to perform the photometry of the star (or group of stars) and to fix inner and outer radii to estimate the luminosity of the sky in that region. DAOPHOT then performs the photometry adding the counts (ADU) within each aperture and removing the average luminosity of the sky which has been estimated in an annulus around the stellar image. There are two obvious drawbacks affecting aperture photometry: on one side in case of crowded images it is arduous to isolate the contribution of each star to the luminosity of the image, on the other side, even in case of isolated images, photometry of faint objects, because the limited number of counts, is dominated by the error in the estimate of the background error and by fluctuations and statistics of the counts.

- **PSF modeling** (PICK and PSF). Once the aperture photometry has been performed, DAOPHOT selects a list of PSF stars (here the limit magnitude is set by the user).

- **PSF fitting** (ALLSTAR). This is a separate stand-alone program. ALLSTAR uses all the information collected in the former steps to perform an individual PSF fitting of all the sources. In each iteration, ALLSTAR subtracts all the stellar images from a working copy of the program image according to the current best guesses of their positions and magnitudes. The program then computes increments to the positions and luminosity of the images from a study of the residuals around each position. Usually the procedure converges rapidly so that the image can be subtracted permanently from the working copy of the frame. After all the program stars have been subtracted from the original frame ALLSTAR memorizes the final image, which can be interactively analyzed to check the quality of the fit and the possible existence of not yet detected faint objects.

- **Stacking the information** (DAOMATCH and DAOMASTER). The images are reduced one by one. Once the operation has been done for all the images the user may ask to have a unique catalogue containing all the parameters associated to a single star in the various frames. This is done by DAOMATCH and DAOMASTER (Stetson 1993). The first one identifies the transformations (translation, rotation, and scale) between the different frames. These transformations are passed to DAOMASTER, which execute the match between the different frames, identifying the stars in common, and produces a master catalogue.

- **Looking for the best PSF** (ALLFRAME). Up to this step the PSF fitting has been performed by ALLSTAR on single images. ALLFRAME is the final step of the procedure as it performs the simultaneous best fit of the stars in all the images, using the geometric and photometric information acquired in the previous steps. The pipeline DAOPHOT/ ALLSTAR/ DAOMASTER has produced different PSF stars list with the relative magnitude and the transformations from one frame to the other, ALLFRAME exploits all the information acquired to produce a list of stars to fit the same object simultaneously on all the frames. The key point of this package is the accuracy in the centroid determination, that allows an optimal fit of the stellar profile, which ensures precise estimates of the deconvolution volume magnitudes. Moreover using all the images stacked together it is possible to reach a deeper photometric level and identify the faintest stars.

3.2.1 Recipe for a good PSF

Given the importance of this issue for the following discussion, it seems appropriate to discuss the adopted procedure in some detail.

The PSF-fitting algorithms ALLSTAR/ALLFRAME require a good estimate of the PSFs on each frame. The first step is to select the stars to identify the PSF. The main criteria adopted to select PSF stars are:

- the stars should be bright, but the images should not be saturated, and they should have good shape parameters;

- the stars too near to the edge of the image are rejected;
- the stars should be isolated from other stars, especially the brighter ones, and not in region with a high crowding;
- the sample of stars selected should be distributed uniformly across the image.

The last point becomes fundamental when working in crowded fields, as it is the case for this thesis. In a crowded field the selection of the images is fundamental to derive the analytical expression of the PSF. I obtained the best PSF fitting using a three-parameter Lorentz function of the form

$$I(r) = \frac{I_0}{[1 + (r/\sigma^2)]^\beta} \tag{3.2}$$

where I_0 is the central peak of the image, σ is the width of the wings and β is the asymptotic slope of the image.

Once PSF stars have been selected, a non-linear analytic best fit is performed. The PSF estimated by DAOPHOT can account for a constant, linear, or quadratic variation across the image. To perform a good PSF fitting on each image I used an iterative procedure. This procedure consists in working on an image where all the neighbors of the PSF stars have been subtracted (SUBSTAR) and the steps listed before are repeated on these new images. I took advantage of the interactivity of the program to check the list of PSF stars and reject not suitable candidates (as stars near the edge, or two stars which were too near to be distinguished by the program). This procedure is repeated by changing the variability of the PSF across the frame every time, passing from a purely analytical to a quadratic varying PSF. The iteration allows ALLSTAR to give step by step a better determination of the centroids and as a consequence to perform an appropriate PSF fitting and, thus, a good photometry.

Following the recipe outlined above, the pipeline DAOPHOT/ALLSTAR was performed individually on all the frames I considered in this thesis.

In the case of the HST data set a further step is needed. For every field and every photometric band two images were available. After executing ALLSTAR, the images of each field were stacked together with DAOMATCH/DAOMASTER and the photometry was re-executed with ALLFRAME. This step was not required in the other cases, as the images had been stacked before.

I performed the photometry of the four sets of data described in Chapter 2. Thus, I ended up with a catalogue for every image. I coupled and merged together the catalogues associated with the same field, different filter, and different exposure time. In addition, the Subaru observations for Draco, UMi, and Her were merged together in one final catalogue each. The matching of the catalogues of the single galaxies is described in Chapters 6, 7, and 8, for Draco, UMi, and Her, respectively.

In the case of NGC 6822 I created one final catalogue for every field, joining those coming from the two chips and the two filters $F475W$ and $F814W$. The six fields of NGC 6822 do not overlap, as shown in Fig. 2.8, and thus I used the six catalogues independently.

Table 3.1 lists the number of objects obtained in each catalogue for the four galaxies, considering only data from HST and Subaru. In the Table the number of objects resulting from the merging of the several fields in Draco, UMi, and Her is indicated. More details on the merging of the Subaru catalogue is given in the following chapters.

3.3 Calibration

In this Section the calibration of the HST data is presented. The calibration of the Subaru data is presented in Sections 6.1, 7.1, and 8.1, for Draco, UMi, and Her, respectively.

3.3.1 HST Data Calibration

The photometry performed according to the lines above described produced six instrumental colour magnitude diagrams (CMDs) in the passbands F814W and F475W.

Table 3.1: List of the number of objects identified at the end of the photometry for the four galaxies. Only HST and Subaru data are considered. In the case of the Subaru data also the number of objects in the final catalogue is indicated.

Galaxy	Field	No. of stars	Galaxy	Field	No. of stars
NGC 6822	1	3740	Draco	1	171450
	2	3530		2	25281
	3	13423		3	28709
	4	139089		4	34431
	5	42279		5	33311
	6	11683		F	31744
				1+2+3+4+5	278773
UMi	1	73721	Her	1	61086
	2	68061		2	47328
	1+2	127428		1+2	95181

In order to reduce errors due to the residual flat-fielding error and background variations, and to increase the S/N aperture photometry and PSF-fitting photometry are usually performed by measuring the flux within a small radius around the center of the source. This measurement must be tied to the total count rates by applying an aperture correction (AP). I used a standard aperture correction for HST data of 0".5 (Sirianni et al. 2005), which correspond to $\sim$ 10 pixels. In a radius of this size around each star the aperture photometry was performed again and the aperture correction was calculated.

The final step was to calibrate into a standard photometric system, in order to allow me to compare instrumental and theoretical data set. HST data can be calibrated using the VEGAMAG system.

The VEGAMAG system is a synthetic photometric system, in which the zero points (ZP) are defined by the magnitude of Vega which is set exactly equal to zero in all filters. In order to compute the real ACS flux the zero-point of the system should be known. ACS WFC zero point are listed in Tab. 3.2 (Version May 2009[2]).

---

[2] The zero points depend on the exposure date. All the versions are available at http://www.stsci.edu/hst/acs/analysis/zeropoints.

Table 3.2: Synthetic Zero Points in the VEGAMAG system for WFC of ACS.

Filter	Zero Point
F435W	25.767
F475W	26.163
F555W	25.727
F606W	26.406
F625W	25.743
F658W	22.382
F814W	25.520

The final step of the calibration is to take into account the decrease in the charge transfer efficiency (CTE) with time, which is caused by the degradation of the silicon in the CCD. The CTE has been modeled with the equation (Riess & Mack 2004)

$$YCTE = 10^{0.14} \times SKY^{-0.31} \times FLUX^{-0.64} \times \frac{Y}{2048} \times \frac{(MJD - 52333)}{365} \quad (3.3)$$

where Y/2048 takes into account the linear relationship with pixel transfer of the CTE loss, MJD is the Julian date of the observations, FLUX is the flux of each star, and SKY is the sky value.

Finally the calibration can be performed according to the following equation

$$m_{cal} = m_{instr} + AP + CTE + ZP + 2.5 \times \log(t_{exp}) \quad (3.4)$$

where t_{exp} is the exposure time, listed in Tab. 2.2 and m_{instr} is the instrumental magnitude.

Chapter 4

Deriving the SFH: the method

The main goal of my thesis is to derive the SFH of NGC 6822, Draco, and UMi. In this chapter I present the codes to derive the SFH (Section 4.1), called IAC-star/MinnIAC/IAC-pop (Aparicio & Gallart 2004; Aparicio & Hidalgo 2009; Hidalgo et al. 2011), specifically developed for analysing resolved stellar populations. In Section 4.2 I focus on the characterization of the observational effects.

4.1 Deriving the star formation history

The technique used to derive the SFH is based on three main codes. The flow chart summarising a standard execution is shown in Fig. 4.1. The characteristics of the single codes are listed in the following:

- **IAC-star (Aparicio & Gallart 2004)**. IAC-star is used to generate a synthetic CMD. It calculates full synthetic stellar populations on a star-by-star basis, by computing the luminosity, effective temperature, and magnitude of each star. IAC-star offers the possibility to choose between a variety of stellar evolutionary and bolometric correction libraries, SFRs, chemical enrichment laws, and model functions such as IMFs and fraction of binary stars. More in detail, the luminosity and effective temperature are computed interpolating in the age-metallicity grid of a stellar evolutionary library (e.g. BaSTI by Pietrinferni et al.

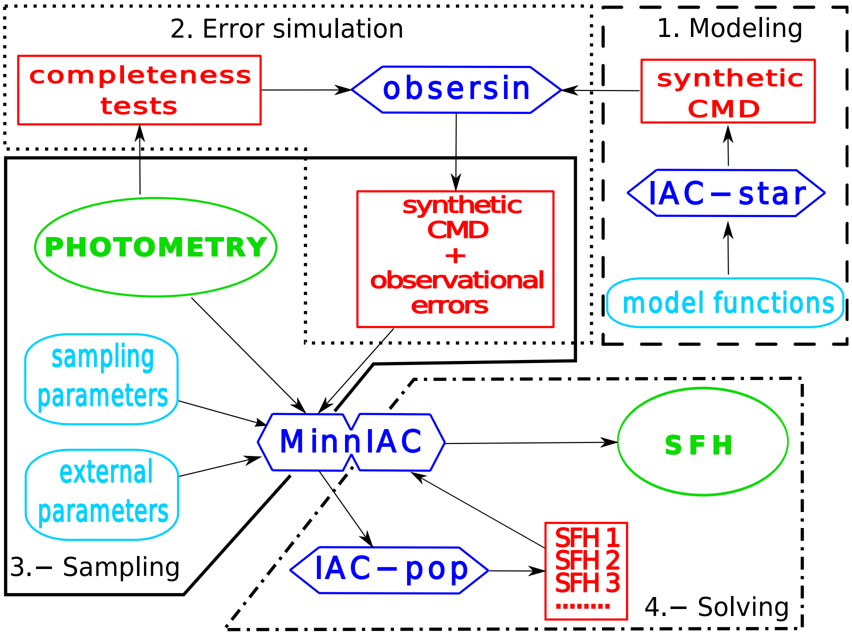

Figure 4.1: Figure from Hidalgo et al. (2011). The flow chart shown summarises how the SFH solution is obtained. For further details see the text, Hidalgo et al. (2011), and references therein. *Model functions* are the IMF and binary fraction. *External parameters* are distance and reddening to a galaxy. *Sampling parameters* are the bundles and the grid arrays for sampling the CMDs.

2004, Padova by Girardi et al. 2000). The mass loss is computed along the RGB and AGB phases. The bolometric correction library provides colours and magnitudes of the stars as a function of their age, mass, and metallicity. Depending on the bolometric correction library, the colours and magnitudes are given in visual broadband, infrared, and HST filters (e.g. Castelli & Kurucz 2003 for the visual regime, Origlia & Leitherer 2000 for the HST filters). Thus, the output is a smooth distribution of stars in a CMD. This is the first fundamental element to obtain the SFH. For a full description see Aparicio & Gallart (2004).

- **IAC-pop (Aparicio & Hidalgo 2009)**. IAC-pop has been designed to solve the SFH of a complex stellar population, like a galaxy. Considering that time and metallicity are the most important variables in the problem, we define the SFH as an explicit function of both. We will use two definitions, one in terms of the number of formed stars and another in terms of the gas mass converted into stars. Formally, $\psi(t, Z)\mathrm{d}t\mathrm{d}Z$ is the mass converted into stars formed within the time interval $[t, t + \mathrm{d}t]$ and within the metallicity interval $[Z, Z + \mathrm{d}Z]$. This function can be identified with the usual definitions of the SFR, as a function of time and metallicity. In addition, the solution of the SFH depends on other parameters, namely the model functions (i.e. IMF and the fraction of binary stars) and external parameters (i.e. photometric zeropoint, distance to the studied object and its reddening). However, the strongest limitation in the method are the observational errors. These will be discussed in Section 4.2. The first step is to create a synthetic CMD (sCMD), as those generate by IAC-star, with a large number of stars, which span an age and a metallicity range. This range has to cover all the possible ages and metallicities of the stars in the studied stellar system. The stars in the sCMD are divided into a number of simple models, i.e. single populations ψ_i each one in a small bin of age and metallicity. In the CMD several regions, called *bundles*, are defined. Every bundle is sampled with a uniform grid, whose dimension can vary from one bundle to the other. In every box j and simple stellar population i, the number of stars, M_i^j, is computed. The same is done in the observed CMD, producing the array O^j. Hence a parametrization of the CMD is obtained and the SFH can be written as a linear combination of M_i^j

$$M^j = A \sum_i \alpha_i M_i^j \tag{4.1}$$

where A is a scaling factor, and $\alpha_i \geq 0$. The CMD, M^j, best matching the distribution of stars O_j in the observed CMD is found using a merit function. A merit function is a function that measures the agreement between data and the fitting model for a particular choice of the parameters. In particular Mighell's χ^2_γ is used. The minimization of

$\chi^2_\nu = \chi^2_\gamma/\nu$, where ν is the number of freedom degrees, provides the best solution as a set of α_i. The minimization is performed through a genetic algorithm. Hence the SFH solution can be written as

$$\psi(t, z) = A \sum_i \alpha_i \psi_i \tag{4.2}$$

The solutions produced by IAC-pop depend on several input functions and parameters. These are the *model functions*, *external parameters*, *sampling parameters* (i.e. the bundles and the grid arrays for sampling the CMDs). In order to minimise the effects of these, several thousands of IAC-pop runs with different inputs are needed. All these solutions are averaged by MinnIAC.

- **MinnIAC (Hidalgo et al. 2011)**. MinnIAC is a suite of routines developed specifically to manage the process of selection of sampling parameters (e.g. bundle definition and grid arrays), creating input data sets, and averaging solutions. More in detail, MinnIAC is used for two tasks. First, to divide the sCMD in the corresponding single stellar populations CMDs according to the selected age and metallicity bins. Second, to define the bundles and box grids in the CMDs and to count stars in them. With this information, MinnIAC creates the input files for each IAC-pop run. Once IAC-pop has produced its output, MinnIAC is used to average solutions found.

The method is more effective if the regions of the CMD more sensitive to evolutionary phases and better known in stellar evolutionary theories are considered, e.g. the MS TO. In fact, one of the fundamental requirements to obtain a detailed SFH is that this region should be well described. Therefore the use of deep photometric data is highly encouraged to obtain a good SFH. For example the data available for NGC 6822 do not allow to reach magnitudes fainted than the TO. Hence, it is not possible to resolve the older populations in this galaxy. This will be widely discussed in Chapter 5.

4.2 Characterisation of observational effects

One of the limitations of the method are observational errors. Signal-to-noise limits, detector defects, and stellar crowding impact on the quality of the photometry of resolved stars. This can result in the loss of stars, variations in measured magnitudes and colours, and systematic uncertainties. Hence, to obtain a highly reliable SFH, the observational errors must be characterized, and then simulated in the stars of sCMD.

To characterize the observational effect, I adopted the standard method of artificial (or false) stars (Stetson & Harris 1988). I added a number of stars per field, placing them in a regular grid. The distance between two artificial stars was fixed in order to pack the largest number of stars but at the same time to ensure that the synthetic stars were not affecting each other. This value was chosen to be $R = 2\ R_{PSF} + 1$, where R_{PSF} is the PSF radius. In this way, the overlap of the wings of the artificial stars was minimized to avoid influencing the fit in the core of the PSF. With this criterion, taking into account the size of the CCD, the number of injected stars does not significantly alter the original crowding. In each iteration, the grid was moved by a few pixels, to better sample the crowding characteristics of the image.

Synthetic stars were randomly and uniformly distributed in order to cover the full colour and magnitude ranges of the observed stars. I set the limit in magnitude of the injected stars $\sim$ 1 mag below the photometric limit. The photometry was then repeated with the same parameters and the same PSF of the original images. The same procedure was adopted for the four galaxies studied here. Table 4.1 lists the number of artificial stars injected, the fixed distance from each other at which they were injected, and the number of iterations necessary to spread all the stars in the original images. Numbers are the same for the two filters of every field.

Once the procedure is concluded the completeness can be evaluated. The completeness is defined as follows

$$Completeness = \frac{N_r}{N_i} \tag{4.3}$$

Table 4.1: For every galaxy the number of false stars injected, the distance R at which they were placed, and the number of iterations is listed. These numbers are the same for the two filters of every field.

Galaxy	Field	Stars	R	N
NGC 6822	1	$\sim 10^7$	15	150
	2	$\sim 10^7$	15	150
	3	$\sim 10^7$	15	150
	4	$\sim 10^7$	15	150
	5	$\sim 10^7$	15	150
	6	$\sim 10^7$	15	150
Draco	1	$\sim 10^7$	31	294
	2	$\sim 10^7$	53	389
	3	$\sim 10^7$	49	320
	4	$\sim 10^7$	35	176
	5	$\sim 10^7$	43	268
	F	$\sim 10^7$	45	268
UMi	1	$\sim 2\ 10^7$	51	682
	2	$\sim 10^7$	35	144
Her	1	$\sim 1.5\ 10^7$	35	243
	2	$\sim 10^7$	31	120

where N_r and N_i are the number of recovered and injected stars, respectively. Fig. 4.2 and 4.3 show the completeness for NGC 6822, Draco, and UMi. In the case of Draco and UMi the artificial star tests were performed only in the long exposures. This is because we are interested in sampling mainly the region around the oldest MS TO.

To derive the SFH, the observational effects need to be simulated in the sCMD. For this purpose, the IAC method uses an additional specific package, *obsersin*. This code uses the unrecovered false stars and the difference between m_i and m_r, injected and recovered magnitude of a false star (Aparicio & Gallart 1995). In addition, as the crowding changes depending on the density of stars, I also used the spatial dependency of the crowding.

In short, for each synthetic star generated by IAC-star, of magnitude m_s a list of false stars with $|m_i - m_s| \leq \epsilon_m$ and $r \leq \epsilon_r$ is created for each filter. ϵ_m and ϵ_r are free parameters set by the user, while r is the spatial distance between the synthetic and the false star. The list of stars is completed when

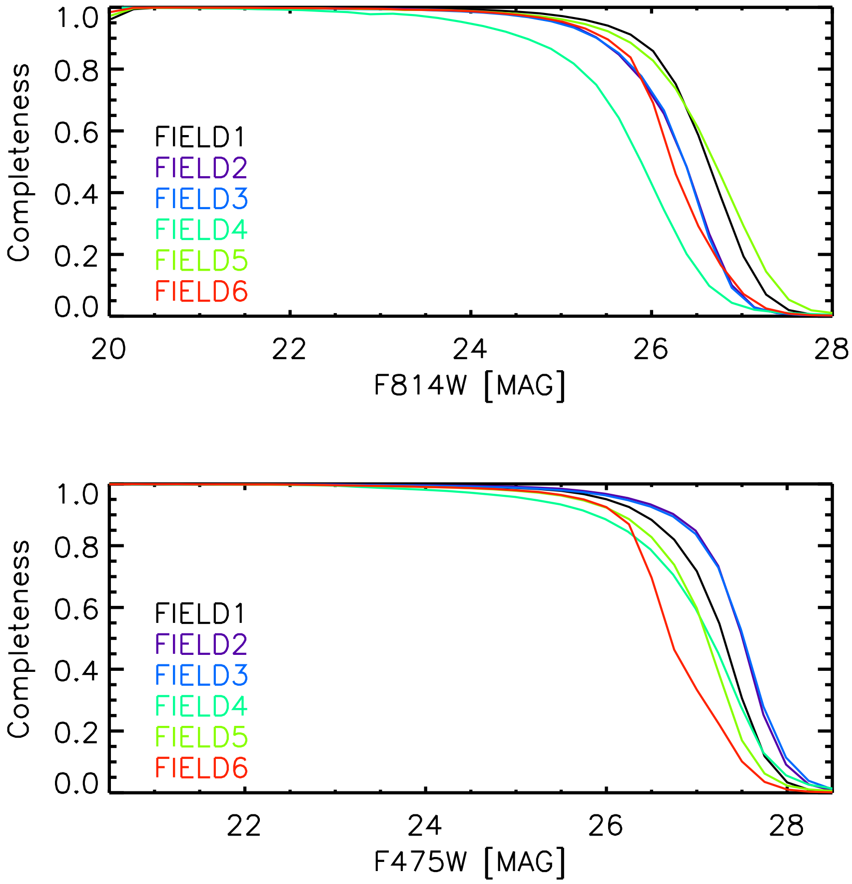

Figure 4.2: Result of the artificial star tests in all the fields of NGC 6822 for the two filters, F814W (*upper panel*) and F475W (*lower panel*). See text for a full description.

at least 10 stars have been found. From the list, one of the false stars is randomly selected. If it is unrecovered, then the associated synthetic star is deleted. On the contrary, if it is recovered, and m_i' and m_r' are its injected and recovered magnitude, then the associated synthetic star is going to have a magnitude $m_s^e = m_s + m_i' - m_r'$. This is the the magnitude of a false star with the observational effects simulated. Further details on the code are given in Hidalgo et al. (2011).

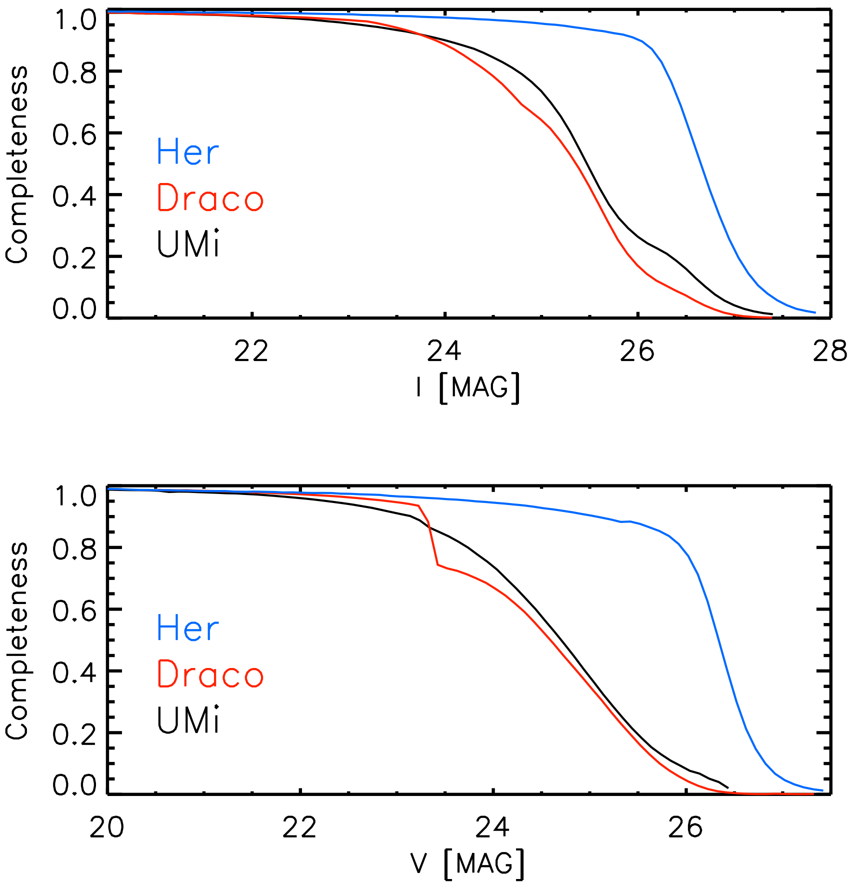

Figure 4.3: Result of the false star tests in all the fields for Draco (in red), UMi (in black) and Her (in blue), in the I (*upper panel*) and V (*lower panel*) filter.

Chapter 5

NGC 6822

5.1 CMDs and Photometric Errors

Using the procedure discussed in Chapter 3, I obtained six calibrated CMDs, one for each field of NGC 6822. The final CMDs obtained are shown in Fig. 5.1, with the associated error bars. These have been estimated using the difference in magnitude of each star, measured in different exposures in each field.

The error associated to each bin in magnitude for each filter is evaluated according to the formula:

$$\epsilon_M = \sqrt{\frac{\sum_{i=1}^{N}(\Delta M_i - bf)^2}{N}} \tag{5.1}$$

where ΔM_i is the difference in magnitude for each filter, and N is the number of stars in each bin of magnitude; bf is the best fit with slope 0 of the distribution.

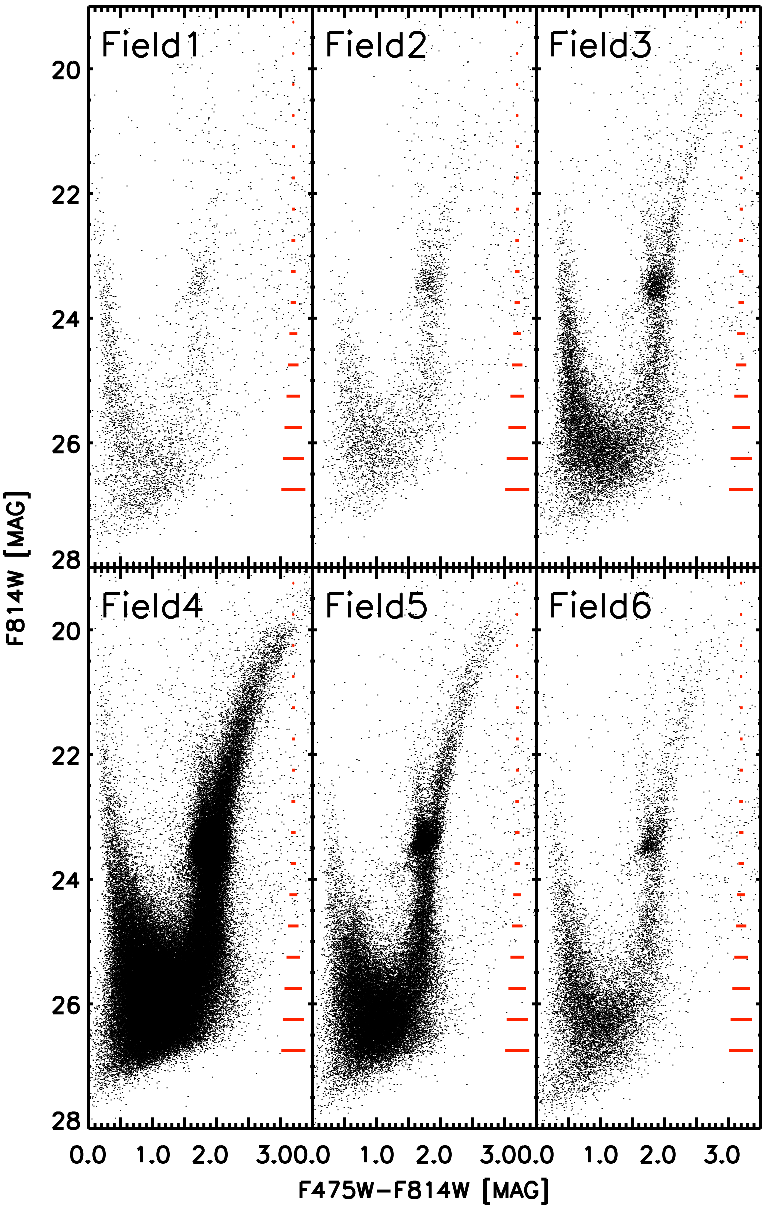

Figure 5.1: Final $F814W$, $F475W - F814W$ CMDs, for the six studied fields. The associated photometric errors are also shown in red.

5.2 Preliminary findings on the stellar populations in NGC 6822

To perform a preliminary analysis of the possible presence of different stellar populations across NGC 6822 I superimposed a set of isochrones to the CMDs of Fields 1 and 4. These two fields were chosen as they are the outermost and innermost of the dataset. I adopted scaled solar isochrones from the BaSTI library (Pietrinferni et al. 2004), and I used the distance modulus and reddening estimates discussed in Section 1.2.1. The result is shown in Fig. 5.2.

The comparison with the isochrones allows to obtain some preliminary estimate of the age and metallicity of the stellar populations in NGC 6822:

- The two isochrones for [Fe/H] = −1.27, age 11 Myr, and [Fe/H] = −0.35, age 30 Myr, shown in Fig. 5.2, appear to constrain the blue edge of the main sequence (MS) fairly well. This comparison strongly suggests that NGC 6822 was still forming stars, at least in these two fields, in a very recent epoch.

- The slope and the location of the RGB in the CMD, on the other hand, give a strong constraint on the metallicity. The RGB of NGC 6822 shows a significant spread, larger than the expected colour error at the magnitude of this branch, as shown in Fig. 5.1. Hence, a spread in metallicity or a combined spread in age and metallicity is present in this dwarf galaxy. The slope of the RGB mainly depends on the metallicity, but an age effect cannot be excluded. Younger RGB stars attain bluer colours, thus mimicking a more metal-poor stellar population. From Fig. 5.2 (*left panels*) it appears that the blue edge of the RGB is represented well by the [Fe/H] = −2.27 and 12 Gyr isochrone. On the other hand, the red edge is compatible with intermediate-age isochrones with slightly higher metallicity (i.e. [Fe/H] = −1.27 and [Fe/H] = −0.96). Therefore, the age-metallicity degeneracy on the RGB does not allow us to constrain the spread in age and metallicity of the population in

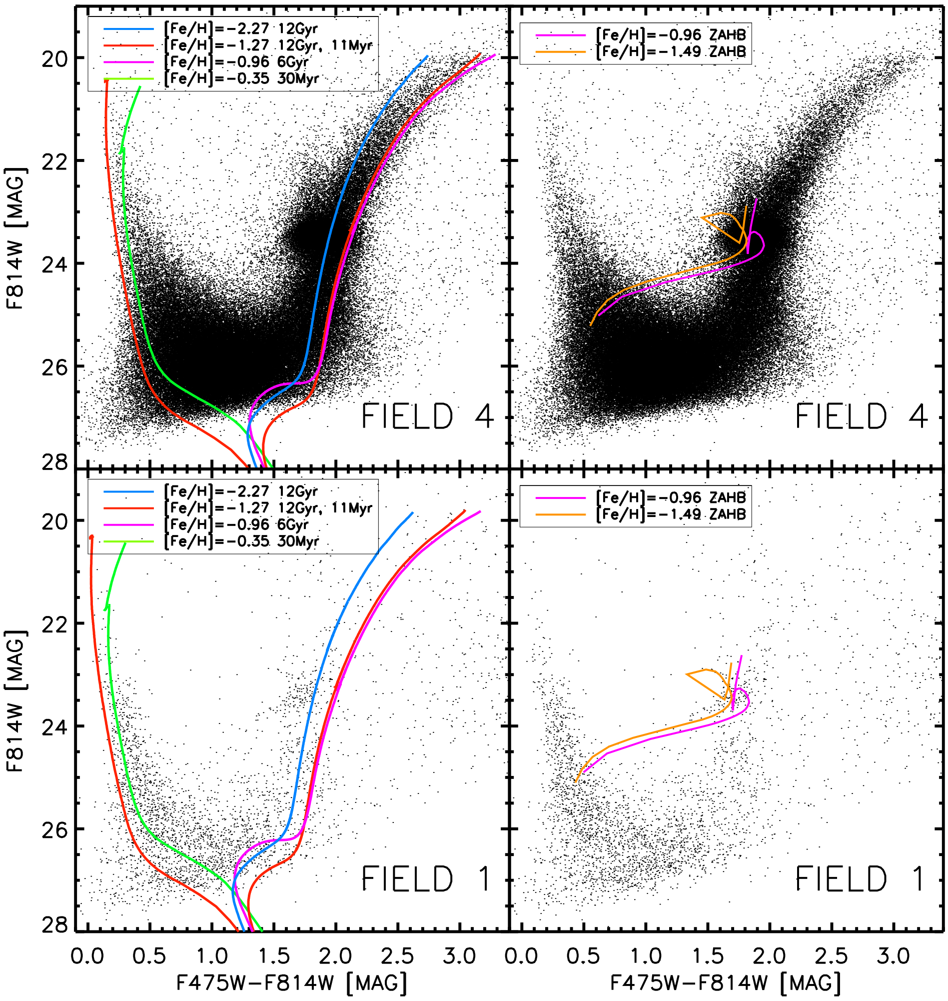

Figure 5.2: *Left panel:* Comparison between the observed CMDs for Fields 4 (*upper panel*) and 1 (*lower panel*) and scaled solar theoretical isochrones for different assumptions about age and metallicity. Lines on the RGB are for [Fe/H] $= -1.27$, 12 Gyr (red line), [Fe/H] $= -0.96$, 6 Gyr (magenta line), and [Fe/H] $= -2.27$, 12 Gyr (blue line). Lines on the MS show two isochrones, respectively with [Fe/H] $= -1.27$ and age 11 Myr (red line) and with [Fe/H] $= -0.35$ and age 30 Myr (green line). *Right panel:* Comparison between core He-burning stars in the CMDs of Fields 1 and 4 and a theoretical ZAHB (with mass range between 0.6 $M_{\odot}$ and 2.8 $M_{\odot}$, in order to include both low-mass HB models and RC ones) for two different metallicities, [Fe/H] $= -0.96$, and -1.49 (magenta and orange line, respectively). All the shown isochrones have been retrieved from the BaSTI archive except the one corresponding to [Fe/H] $= -1.27$ and age of 11 Myr, which has been computed for the present work.

NGC 6822. The qualitative comparison between theoretical isochrones and observational data discloses that the photometric limit does not allow us to detect the MS turn off (TO) of the oldest population.

- In the *righthand* panels of Fig. 5.2 the zero age horizontal branch (ZAHB) is shown for two metallicities [Fe/H] $= -0.96$ and [Fe/H] $= -1.49$ (mass range between 0.6 $M_\odot$ and 2.8 $M_\odot$). The observed red clump appears well fitted by the central helium-burning sequence of [Fe/H] $= -0.96$. There is some evidence that the intermediate-red colour HB is partially populated. The presence of the bright blue MS does not allow us to detect any blue HB stars.

To have a closer insight into the nature of the stellar populations in the different fields of NGC 6822 I performed star counts in the different branches of the CMDs. I started by selecting five boxes in the most populated regions in the CMD of Field 4. These are shown in Fig. 5.3 and were defined as

UpMS: The upper MS box encloses MS stars brighter than F814W= 23.7 mag where the MS luminosity function (LF) shows a slight change in its slope.

LowMS: The lower main sequence box contains MS stars between 25 mag $<$ F814W $<$ 23.7 mag. According to the completeness tests I performed, F814W = 25 mag is the limit of our photometry. The cut at F814W = 23.7 mag corresponds to the TO of the stars with an age of 450 Myr (for [Fe/H] $= -0.66$). The comparison between UpMS and LowMS allows us to discriminate between stars younger and older than 450 Myr.

RC: According to the change in slope of the RGB LF, we defined the interval 23 mag $\leq$ F814W $\leq$ 23.9 mag as the red clump region.

LowRGB: The lower RGB corresponds to 23.9 mag $\leq$ F814W $\leq$ 25 mag. The brighter limit in magnitude is set as the boundary of the RC region, while the fainter limit coincides with the limit in magnitude selected for our photometry according to the completeness tests.

Table 5.1: Star counts and corresponding number ratios in the selected boxes of the CMD for the various fields of NGC 6822. The distance modulus and the absolute reddening of the fields are listed.

	Field 1	Field 2	Field 3	Field 4	Field 5	Field 6
Region	$N_1 \pm \epsilon_{N1}$	$N_2 \pm \epsilon_{N2}$	$N_3 \pm \epsilon_{N3}$	$N_4 \pm \epsilon_{N4}$	$N_5 \pm \epsilon_{N5}$	$N_6 \pm \epsilon_{N6}$
LowMS	257 ± 16	160 ± 12	1146 ± 33	5047 ± 71	857 ± 29	477 ± 21
UpMS	86 ± 9	16 ± 4	188 ± 13	779 ± 27	79 ± 8	77 ± 8
LowRGB	106 ± 10	219 ± 14	708 ± 26	10191 ± 100	2435 ± 49	537 ± 23
UpRGB	62 ± 7	105 ± 10	403 ± 20	6223 ± 78	1313 ± 36	322 ± 17
Ratio	$R_1 \pm \epsilon_{R1}$	$R_2 \pm \epsilon_{R2}$	$R_3 \pm \epsilon_{R3}$	$R_4 \pm \epsilon_{R4}$	$R_5 \pm \epsilon_{R5}$	$R_6 \pm \epsilon_{R6}$
UpMS/UpRGB	1.4 ± 0.2	0.15 ± 0.04	0.47 ± 0.03	0.12 ± 0.01	0.06 ± 0.01	0.24 ± 0.03
LowMS/LowRGB	2.4 ± 0.2	0.73 ± 0.06	1.56 ± 0.05	0.49 ± 0.01	0.35 ± 0.01	0.89 ± 0.04
LowMS/UpMS	3.0 ± 0.5	10.0 ± 0.8	13.6 ± 0.4	6.5 ± 0.1	10.8 ± 0.4	6.2 ± 0.3
$(\mathrm{m} - \mathrm{M})_{\mathrm{F814W}}$	24.1±0.1	24.2±0.1	24.2±0.1	24.2±0.1	24.1±0.1	24.1±0.1
E(F475W−F814W)	0.51±0.05	0.63±0.05	0.63±0.05	0.63±0.04	0.51±0.05	0.51±0.05

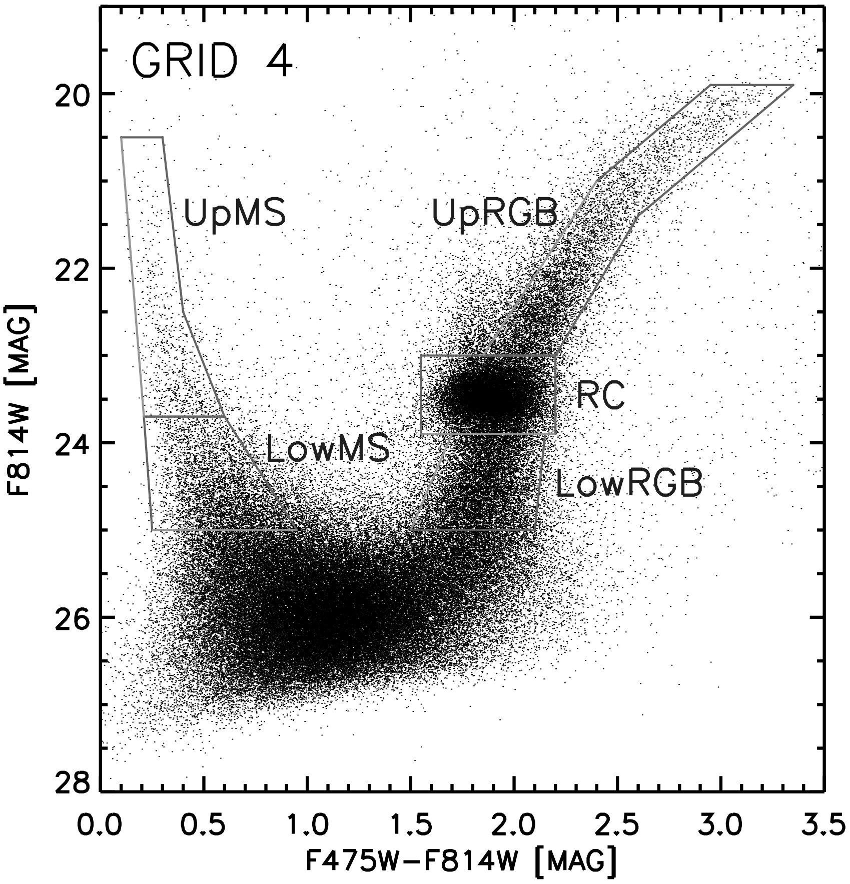

Figure 5.3: CMD of Field 4. The lines superimposed identify the regions where the counts have been performed. The counts in the different regions are listed in Table 5.1.

UpRGB: Correspondingly I define the upper RGB branch as the region of the RGB brighter than the RC. The bluer part of the RGB was excluded with a by-eye inspection in order to minimize the contribution of the asymptotic giant branch to the star counts.

Table 5.1 shows the star counts in each box and the relative ratios. The errors listed in this table are given by the statistical fluctuations of the counts. I performed several experiments of artificial stars in all the fields (for a complete description see Section 4.2) in order to confirm the statistical completeness of the star counts. The result is shown in Fig. 4.2, confirming that the counts at the limit F814W = 25 mag are complete at least at the 85% level.

To perform quantitative comparisons, the box boundaries were shifted according to the relative reddening of each field. Inspection of Table 5.1 immediately reveals that the two ratios UpMS/UpRGB and LowMS/LowRGB, i.e. the number of stars on the MS with respect to those on the RGB at the same luminosity level, turn out to be definitely higher in Field 1, and marginally in Field 3, than in all the other fields. The completeness of the star counts in the boxes of the first ratios is nearly 100%, hence, highly significative. These ratios, taken at their face values, could provide a first hint that the stellar populations in Field 1 and 3 could be peculiar owing to the under-abundace of RGB stars with respect to MS stars. In particular, this result could apparently suggest that a very recent burst of star formation took place in Field 1, which was more intense than in the other fields, including the innermost Field 4.

Therefore I computed the cumulative LFs of the RGB and of the MS for the six fields, as shown in Fig. 5.4. While the RGB LFs appear virtually identical in all of the fields, the LF of Field 1 starts increasing at brighter magnitudes for the MS with respect to all the other fields. This is a second hint to support the idea that the star formation in Field 1 could somehow be peculiar and that a relatively recent burst of star formation could have occurred in this region.

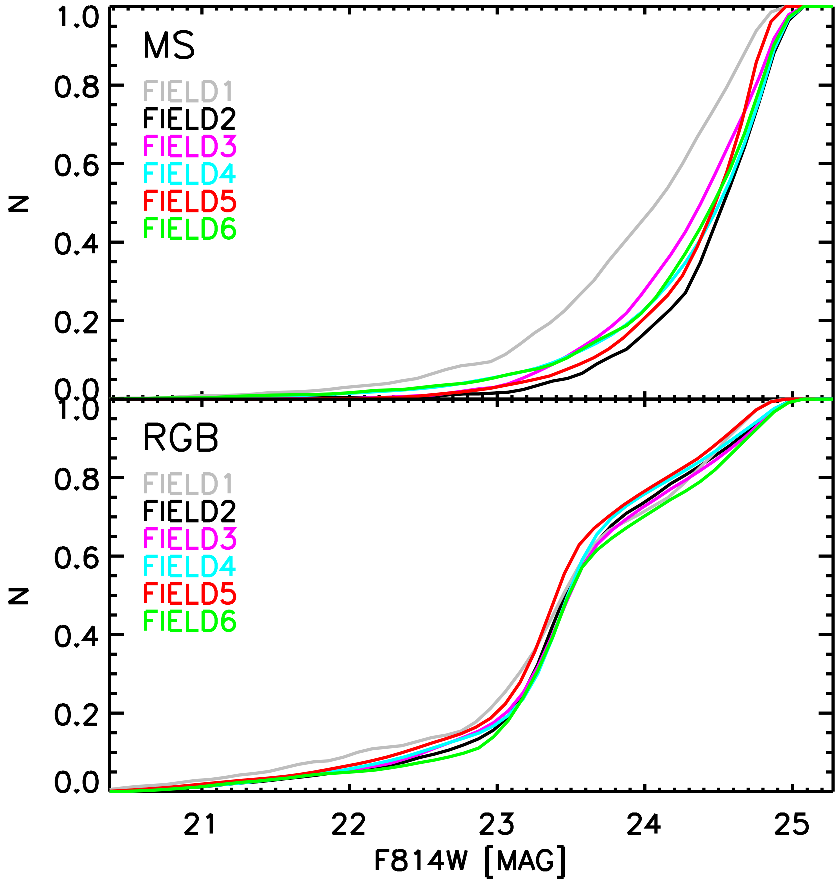

Figure 5.4: Cumulative LF of the MS (*Upper panel*) and of the UpRGB (*Lower panel*) for the six fields considered. The LF of the RGB in the interval $22.7 \leq \mathrm{F814W} \leq 23.7$, corresponding to the RC region, has been obtained by interpolation along the RGB LF at magnitudes slightly fainter and brighter than the RC box.

5.3 A detailed analysis of the SFH in the different fields

The former findings indicate that significant differences may exist in the stellar populations of the six fields. To investigate these differences in depth, I use resolved population synthesis tools to calculate the SFH of the six fields. To obtain the SFH solution I considered only the stars with $\sigma_{\mathrm{F814W}} \leq 0.2$, $\sigma_{\mathrm{F475W}} \leq 0.2$, and $|\mathrm{sharp}| \leq 0.5$[1]. This selection allows us to obtain the solution using only stellar objects and thus improving the precision of the SFHs.

The first step is to accurately represent the observational effects which is done through tests of artificial stars (Stetson & Harris 1988). The detailed description of the procedure adopted can be found in Section 4.2.

The SFH was derived by applying the state-of-art package IAC-star/IAC-pop/MinnIAC (Aparicio & Gallart 2004; Aparicio & Hidalgo 2009; Hidalgo et al. 2011), specifically developed for analysing resolved stellar populations. This has been widely discussed in Chapter 4.

In short, IAC-star is used to create a synthetic CMD model. In this case, the synthetic CMD model contains 10^7 stars with a constant star formation rate between 0 and 13.5 Gyr and uniform metallicity distribution between $Z = 0.0001$ and $Z = 0.01$ – corresponding to $[\mathrm{Fe/H}] = -2.27$ and $[\mathrm{Fe/H}] = -0.27$. The extreme values were selected to cover all the ages and all the metallicities (Clementini et al. 2003; Venn et al. 2001) of the stars present in NGC 6822. I selected the BaSTI stellar evolution library (Pietrinferni et al. 2004), a Kroupa initial mass function (Kroupa 2001), and a 30% binary fraction. After a suitable simulation of the observational effects in the synthetic CMD, the SFH is obtained using IAC-pop/MinnIAC algorithms (Aparicio & Hidalgo 2009; Hidalgo et al. 2011) by comparison of the distribution of stars in the synthetic CMD with that in the observed CMD. The age bins selected are of 0.1 Gyr for age < 0.2 Gyr,

---

[1] The sharpness parameter is a standard DAOPHOT output, which quantifies the accuracy of the PSF profile.

0.3 Gyr for $0.2 <$ age < 0.5 Gyr, 0.25 Gyr for $0.5 <$ age < 1 Gyr, 1 Gyr for $2 <$ age < 5 Gyr, and 8.5 Gyr for $5 <$ age < 13.5 Gyr. The metallicity bins selected are $3 \cdot 10^{-4}$ for $10^{-4} \leq \mathrm{Z} \leq 10^{-3}$, $2 \cdot 10^{-3}$ for $10^{-3} \leq \mathrm{Z} \leq 3 \cdot 10^{-3}$, $4 \cdot 10^{-3}$ for $3 \cdot 10^{-3} \leq \mathrm{Z} \leq 7 \cdot 10^{-3}$, and $3 \cdot 10^{-3}$ for $7 \cdot 10^{-3} \leq \mathrm{Z} \leq 10^{-2}$. These values were selected according to the age-metallicity resolution tests presented in Section 5.4. With this method I obtain the smoothed SFHs, which include 24 single SFHs. For a full description I refer to Hidalgo et al. (2011).

To minimize the effect of the estimates in the external parameters, namely distance, reddening, and photometric zeropoints, IAC-pop/MinnIAC synthesis codes provide an offset both in magnitude and colour. These values are those which minimize the χ^2 of the solution. Table 5.2 shows the distance of the fields from the centre of NGC 6822, the χ^2, and the offset in colour and magnitude of the solutions.

To evaluate the relative importance of the SFR in the fields, I evaluated the mass fraction of stars produced in two age bins. The results are listed in Table 5.2, where the old-intermediate- (between 13.5 and 0.5 Gyr ago) and young- (from 0.5 Gyr ago to date) epochs were taken into account. Inspection of this table reveals that the integral $\int_{0.5}^{13.5} \psi(t)dt$ in all the fields is comparable, whereas the integral $\int_{0}^{0.5} \psi(t)dt$ turns out to be very small for all the fields with the exception of Fields 1 and 3. In these fields the SFR shows a slight enhancement in this time interval. Nine and six times more stars were produced in Fields 1 and 3, respectively, than in Field 4.

In addition, the mean metallicity of the six fields is listed in Table 5.2. This result is perfectly compatible with the metallicity estimates by Kirby et al. (2013a). Moreover, the associated spread in metallicity is compatible with the spectroscopic results.

5.4 SFH solution and AMR

The SFH solution of the fields is shown in Fig. 5.5. The function $\psi(\mathrm{t})$ is the stellar mass formed as a function of time, while Ψ_{norm} corresponds to $\psi(\mathrm{t})$ normalized to $\int_{0}^{13.5} \psi(\mathrm{t})\mathrm{dt}$. The scales along the vertical axis are different for

Table 5.2: Field, distance from the centre (where the negative values identify the fields in the south-eastern region of the galaxy), χ^2, offsets in magnitude F814W and colour (F475W−F814W) of the solution, integral of the SFR in two time intervals (between 0.5 and13.5 Gyr ago and from 0.5 Gyr ago to date), mean metallicity and spread in metallicity are shown.

Field	Dist. [deg]	χ^2	ΔF814W	Δ(F475W − F814W)	$\int_0^{0.5} \psi(t)dt$	$\int_{0.5}^{13.5} \psi(t)dt$	$\langle$[Fe/H]$\rangle$
1	0.43	0.78	0.2	0.05	0.100 ± 0.007	0.90 ± 0.07	-0.9 ± 0.3
2	0.32	0.76	0.2	0.15	0.017 ± 0.002	0.98 ± 0.06	-0.8 ± 0.1
3	0.22	1.04	0.1	0.05	0.066 ± 0.004	0.93 ± 0.08	-0.9 ± 0.2
4	−0.06	2.35	0.08	0.15	0.011 ± 0.001	0.99 ± 0.08	-0.7 ± 0.1
5	−0.16	1.26	0.0	0.07	0.009 ± 0.001	0.99 ± 0.07	-1.0 ± 0.2
6	−0.26	1.23	0.05	0.02	0.018 ± 0.002	0.98 ± 0.09	-1.0 ± 0.1

each field as a consequence of the difference in the total stellar mass. The solutions I obtained are consistent with the results presented by Cannon et al. (2012). Figure 5.6 shows observed, solution and residual CMDs in the case of Field 5.

The photometric limit avoids properly sampling the MS TO of the oldest population. To estimate the age limit of our solution, I carried out age resolution tests (for a full description the reader should refer to (Hidalgo et al. 2011)). Using IAC-star I created six mock populations of 10, 5, 3, 1, 0.2, 0.1 Gyr. Thus I performed the same procedure adopted to obtain the SFH solution, in order to recover the narrow mock bursts at different times. The result is shown in Fig. 5.7 for Field 2, as an example. Scrutiny of this figure shows that it was not possible to recover the mock bursts of 5 and 10 Gyr. For this reason, the temporal scales of our solutions are not reliable for ages older than about 5 Gyr, although the integral $\int_5^{13.5} \psi(\mathrm{t})\mathrm{dt}$ is still accurate and well defined.

We now concentrate on the analysis of the individual SFH solutions (Fig. 5.5) taking only ages $\leq$ 5 Gyr into account. This analysis discloses the following results:

Field 1. This field does not show any significant burst of SF until 500 Myr ago, when the most recent burst began and continued to increase up to a very recent epoch.

Field 2. This field shows an SFR that remains quite constant over the whole time interval and tends to zero at the most recent epochs.

Field 3. The SFR in Field 3 appears to be as constant as that of Field 2. In the past 500 Myr the SF, according to our solution, maintains a higher rate than in the other fields, but tends to disappear at very recent epochs.

Field 4. A unique extended SF episode took place in this region of NGC 6822 between 5 and 1.5 Gyr ago. In the last 1.5 Gyr the SFR vanished.

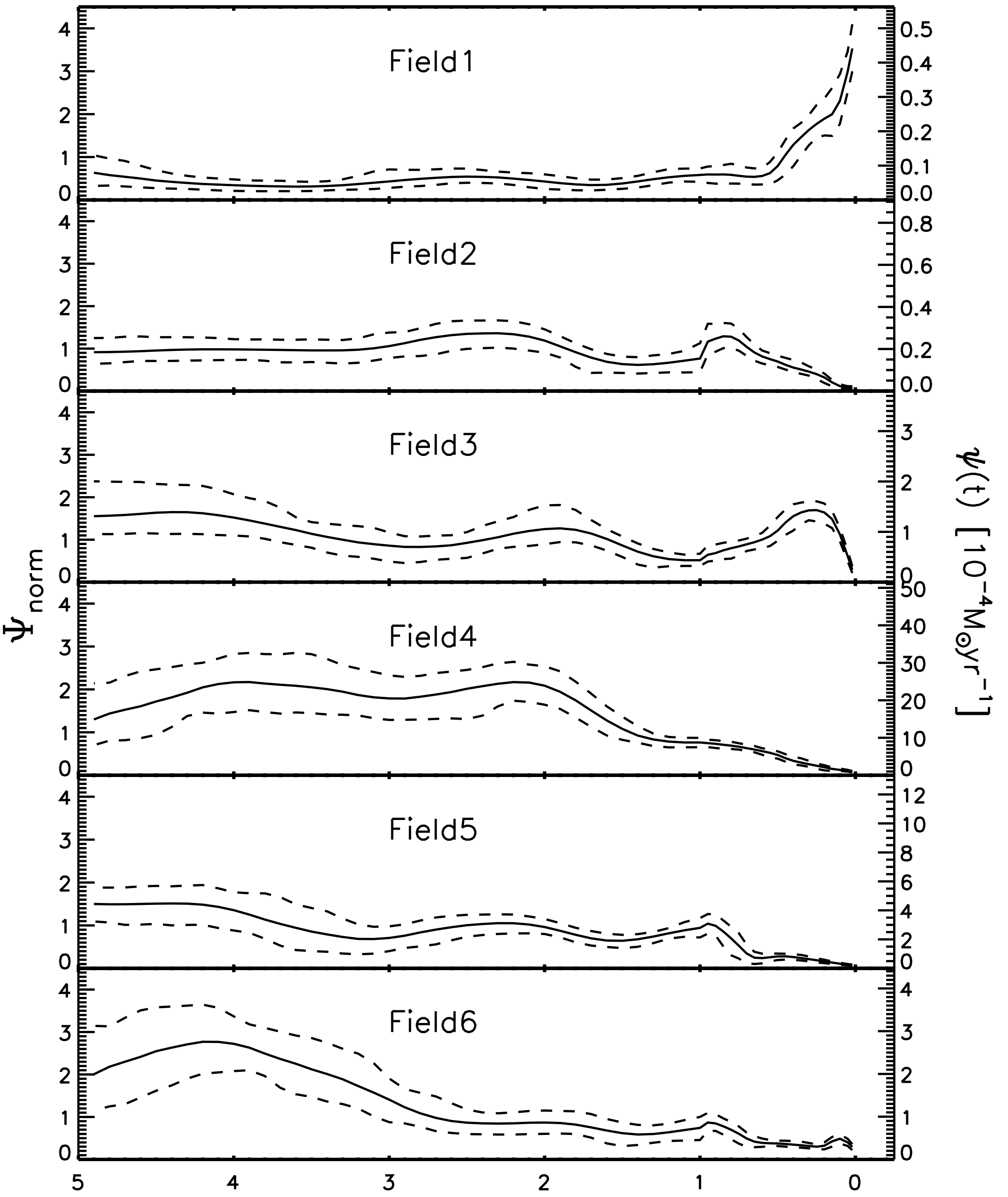

Figure 5.5: SFH for the six fields (solid line) as function of the time for the last 5 Gyr, with the relative error (dashed line). $\psi(t)$ (labeled of the right-side axis) is the stellar mass formed, while $\Psi_{\rm norm}$ (labeled of the left-side axis) shows $\psi(t)$ normalized to $\int_0^{13.5}\psi(\rm t)dt$. See text.

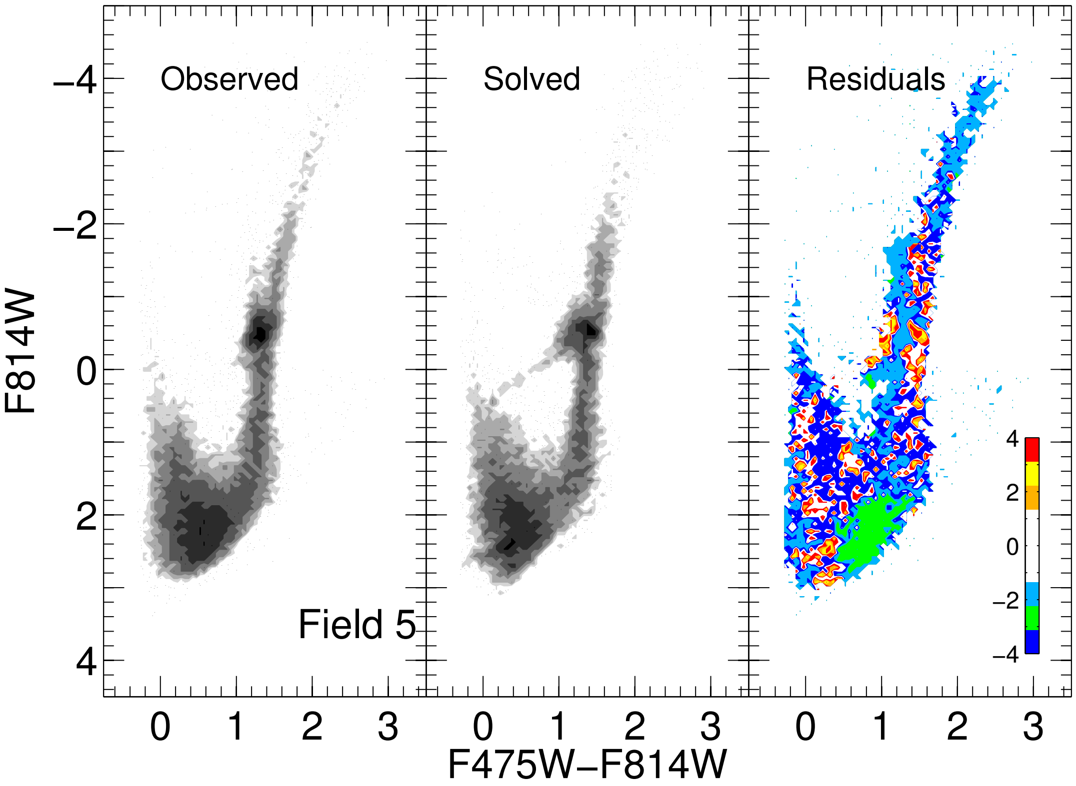

Figure 5.6: *Left panel:* Observed CMD for Field 5. *Central panel:* the CMD according to the SF produced by IAC-pop/MinnIAC. *Right panel:* Residuals obtained as the difference between the observed and the solution CMDs counted in different bins in units of Poisson errors. Different colours correspond to different errors in agreement with the scale shown in the right panel. A similar result is obtained for all the other fields.

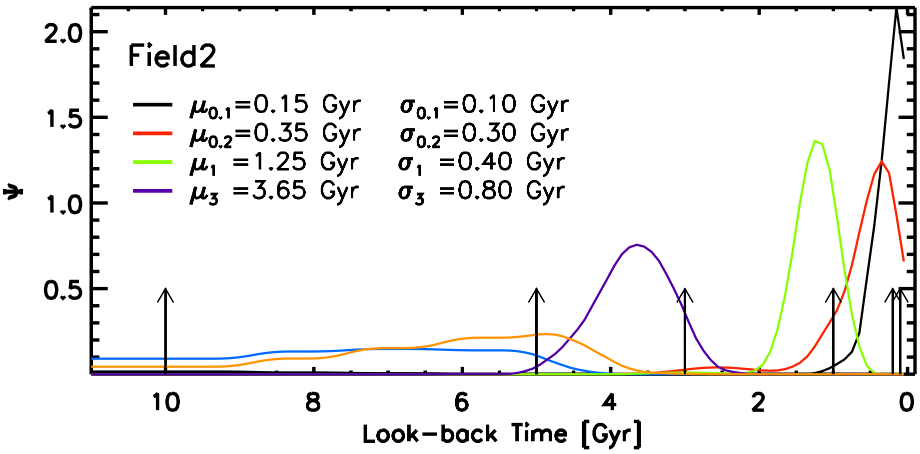

Figure 5.7: Age resolution tests for Field 2 for six different burst ages (indicated by the arrows), namely $10, 5, 3, 0.2, 0.1$ Gyr. Gaussian profiles represent the recovered SF episodes. The age peak and σ are given. Each colour represents the recovered SF episode of a different age, in blue, orange, violet, green, red, and black lines respectively from the oldest to the youngest. Similar results are obtained for all the other fields.

Field 5. The SF calculated for this field is analogous to the rate obtained in Field 2.

Field 6. The SF calculated for this field is analogous to the one obtained in Field 4.

From the analysis of the single solutions of the SF, I find that in Fields 2, 4, 5, and 6, the SFR has been slowly decreasing in the last 1.5 Gyr, and it is exhausting at very recent epochs. Fields 1 and 3 are apparent exceptions to this frame. For these field the solutions show an enhancement in the SFR in the last 500 Myr, and in the case of Field 1 it has still been active at very recent epochs.

In addition, the IAC-pop/MinnIAC method allows deriving the AMR as a part of the SFH. The AMRs for six fields of NGC 6822 are shown in Fig. 5.8 for the last 5 Gyr.

The AMRs disclose that the metallicity grows with time in all the six fields, ranging between $-1.0 \lesssim [\mathrm{Fe/H}] \lesssim -0.5$. According to our solution no difference in the AMR of the six fields is identified. These values are compatible with the mean metallicity and the spread in metallicity recently found spectroscopically for NGC 6822 by Kirby et al. (2013a).

5.5 Radial gradients

Our dataset samples the bar of NGC 6822 up to about five times its scale length. This offers a good opportunity to investigate the radial stellar populations distribution and the possible presence of a population gradients.

Several authors have studied the population gradients in the dwarf galaxies of the LG (e.g. Hidalgo et al. 2013 and references therein). In all the cases the trend found is the same: the age of the youngest populations gets older for increasing radius, and progressively younger populations are only found in the innermost regions. The observed effects agree with models of simulated dwarf galaxies (Schroyen et al. 2013).

Regarding NGC 6822, the spatial distribution of the stellar populations have already been discussed by Gallart et al. (1996b,a). They studied the central regions of the galaxy and found an enhancement of the SFR in the past 100-200 Myr, which occurred over the whole main body of the galaxy. The strength of this enhancement is different between the different regions of NGC 6822. This results were confirmed by Cannon et al. (2012), who noticed that NGC 6822 formed more than 50% of the stars in the last 5 Gyr.

In this research I started evaluating $\int \psi(\mathrm{t})\ \mathrm{dt}$ in two time intervals, between 0 and 0.5 Gyr ago and between 0.5 and 13.5 Gyr ago, as a function of the galactocentric distance. The results are shown in Fig. 5.9. Clear exponential profiles are disclosed in all cases, except for the young populations of Fields 1 and 3. The scale lengths are compatible within the errors for the old and young populations. These result in $r_{0.5}^{13.5} = 680 \pm 75$ pc and $r_0^{0.5} = 730 \pm 160$ pc for the old- and the young-population. $r_0^{0.5}$ was computed excluding Fields 1 and 3. Fields 1 and 3 show young populations that exceed the ones of the surrounding fields by a factors of 10 and 3, respectively. This may be the simple result of a stochastic enhancement of the SFR in recent

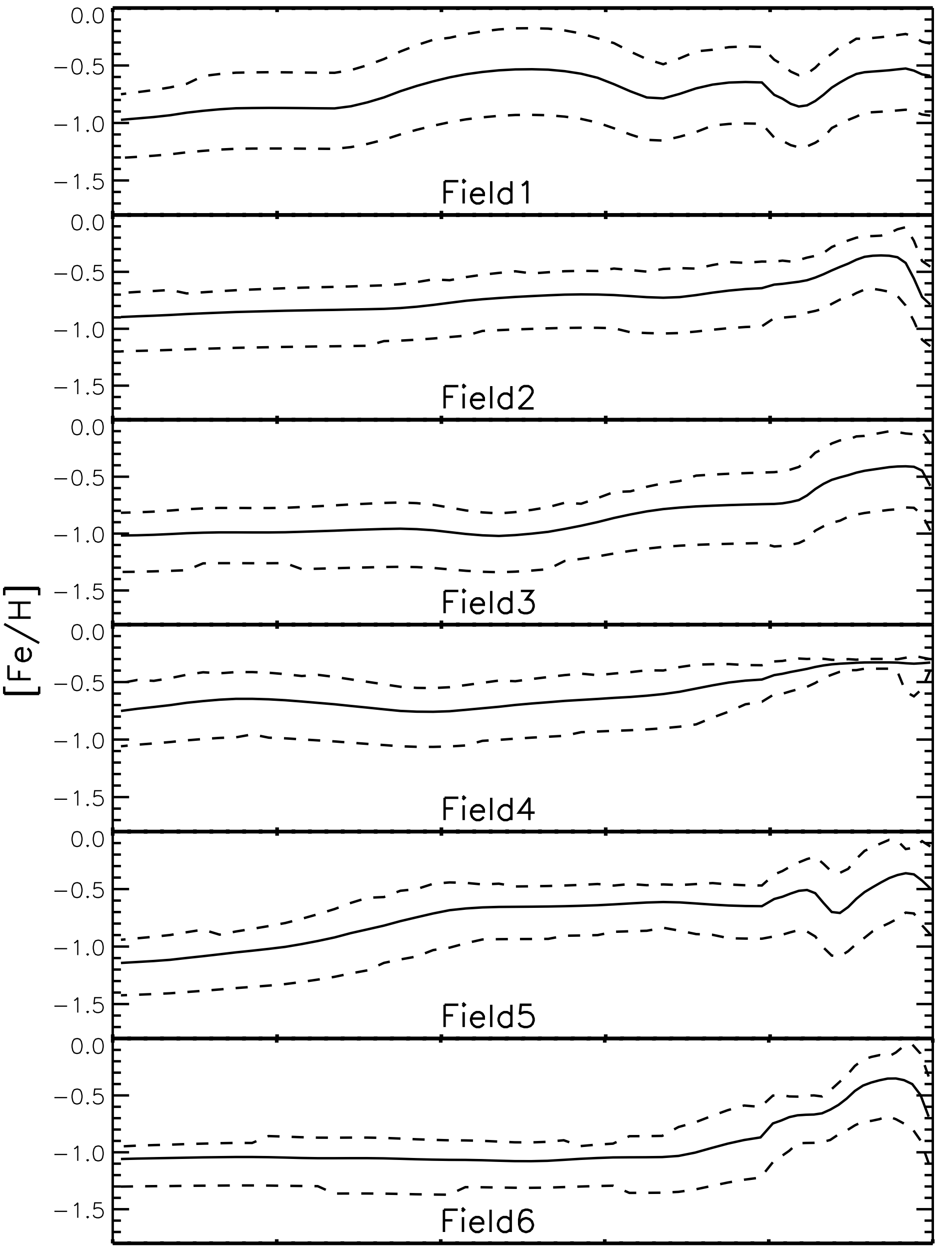

Figure 5.8: AMRs for the six fields (solid lines), including error bars (dashed lines), as function of the time for the last 5 Gyr.

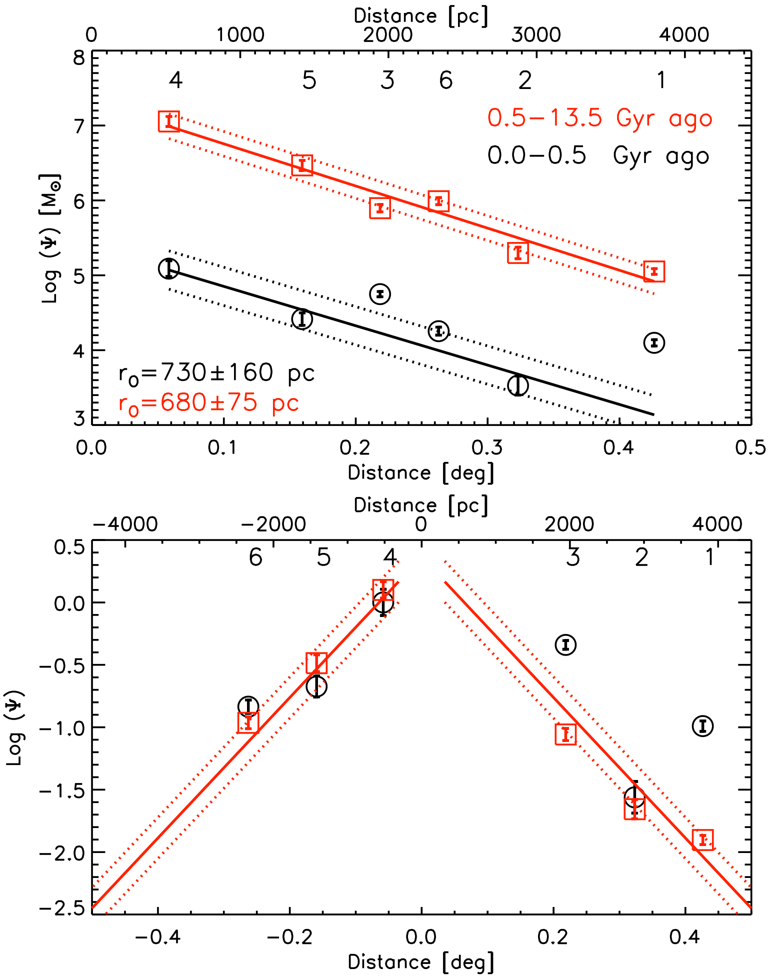

Figure 5.9: The integral of the SFR, ψ(t), for the young (from 0.5 Gyr to date; black dots) and intermediate-to-old (between 0.5 and 13.5 Gyr ago; grey squares) stellar populations, as a function of the galactocentric distance. *Upper panel*: the absolute value of the galactocentric distance is shown in the horizontal axis. Distances are given both in degrees (lower axis scale) and in parsecs (upper axis scale). Distances in parsecs have been obtained assuming a distance to NGC 6822 of 510 kpc (Fusco et al. 2012). The solid lines show the best fit of the points in the two time intervals, with the associated errors (dotted lines). Fields 1 and 3 were excluded from the fit in the case of the young stellar population. The resulting scale length r_0 and the name of the field are indicated. *Lower panel*: same as the *upper panel*, but the galactocentric distances are shown as they appear along the galactic semi-major axis (negative and positive values corresponding to eastern and western fields, respectively). Points have been shifted vertically in order to make the older and younger distribution barycentres coincide. The vertical scale zeropoint is arbitrary. Grey lines reproduce the fit shown in the *upper panel* for the older population. The colour coding is the same a in the *upper panel*.

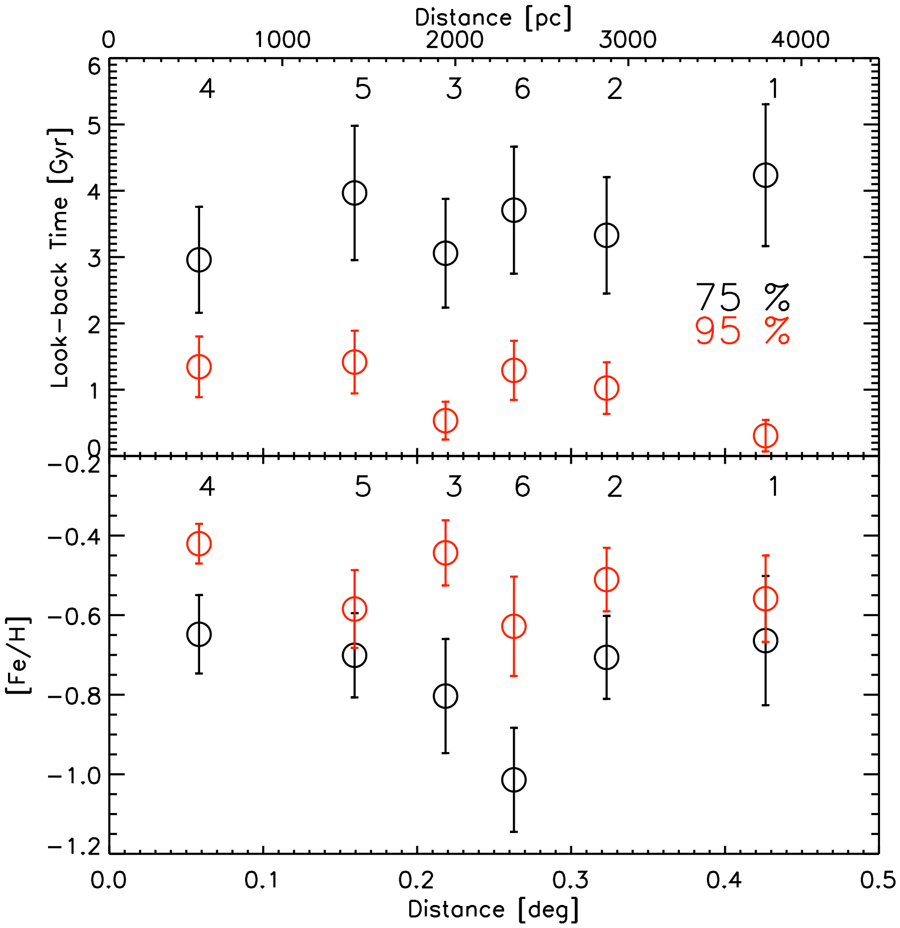

Figure 5.10: Age and metallicity as a function of the galactocentric distance. The latter is shown both in degrees (lower axis scale) and in parsecs (upper axis scale). The distances in parsecs have been obtained assuming a distance to NGC 6822 of 510 kpc (Fusco et al. 2012). *Upper panel*: look-back times of the 75 and 95 percentiles of the SFR as a function of the galactocentric distance. Numbers from 1 to 6 within the panel identify the corresponding fields. *Lower panel*: the mean metallicity for the same percentiles. The percentiles and the colour coding are the same as in the *upper panel*.

epochs. However, this could also be the signature of incipient spiral arms. With the present dataset this is only a speculative suggestion. New data are required to either support or rule out this possibility.

Following Hidalgo et al. (2009), I consider the times corresponding to the 75 and 95 percentiles of the SFR to further analyse the radial gradients. In other words, the times t_{75} such that $\int_0^{\mathrm{t}_{75}} \psi(\mathrm{t})\ \mathrm{dt}/\int_0^{\mathrm{T}} \psi(\mathrm{t})\ \mathrm{dt} = 0.75$ and t_{95} such that $\int_0^{\mathrm{t}_{95}} \psi(\mathrm{t})\ \mathrm{dt}/\int_0^{\mathrm{T}} \psi(\mathrm{t})\ \mathrm{dt} = 0.95$, where T is the current age of the system. Figure 5.10 shows the look-back time and the metallicity as a function of the galactocentric distance for the two percentiles. Scrutiny of this figure reveals that the 75 percentile corresponds to similar look-back times in all the cases. The look-back times associated to the 95 percentile are similar for Fields 2, 4, 5, and 6, but they correspond to a more recent epoch for Fields 1 and 3. Moreover, Fig. 5.10 discloses that the metallicity increases in all the fields from the 75 to the 95 percentiles, but it does not show any radial gradient. To quantify these findings, I obtained an empirical relation $Z = Z(t, D)$, where Z is the metallicity, t is the look-back time, and D the galactocentric distance in kpc

$$Z = [(5.7 \pm 1.5) - (0.57 \pm 0.08)t - (0.8 \pm 8.5)D] \cdot 10^{-3}. \tag{5.2}$$

The errors of the fitting parameters confirm that the metallicity significantly increases with time, but that no significant metallicity gradient as a function of the distance is present. These results confirm the findings that have already been presented.

NGC 6822 does not show the trend found in similar galaxies by Hidalgo et al. (2013). They studied the SFH of two dIrr/dSph galaxies, namely LGS-3 and Phoenix, whose total stellar masses are about 100 times lower than that of NGC 6822. They find that, for ages < 9 Gyr, the SFR gradually decreases outwards and that the metallicity does not change significantly with time or with distance from the centre. For recent epochs they find a steep increase in the metallicity, which does not have a counterpart in the SFR.

Chapter 6

Draco

In this chapter I will focus on the analysis of the dwarf spheroidal galaxy Draco. In Section 6.1 the calibration of the data is presented. The resulting CMDs and the estimate of the distance modulus are discussed in Sections 6.2 and 6.3. Hence, the SFH and the stellar populations in Draco are considered in Sections 6.4, 6.5, and 6.6.

6.1 Calibration

The first step in the analysis is to calibrate the instrumental magnitudes obtained by the photometry to a standard photometric system. In the case of Draco, the photometric observations were carried out in the Johnson-Cousin filters, hence I calibrated to this photometric system.

To calibrate Draco, I relied on the standard stars in the field of this galaxy, provided by Stetson (2000a, 2005). The advantage of having standard stars in the field of the galaxy is that the zero-point of the calibration includes also the aperture correction and the air mass. Therefore, the calibration equation can be written as

$$m_{cal} = m_{instr} + ZP_m + C_m \ (V - I) \tag{6.1}$$

where ZP_m is the zero-point, C_m is the colour coefficient, and $m_{instr} = m_{phot} + 2.5 \ \log(t_{exp})$.

The standard stars available fall mainly in field 1 and, as these stars are brilliant and their long exposure are saturated, I used the short exposure to carry out the calibration. Figure 6.1 shows the derivations of the calibration equations obtained for Draco, which result in:

$$\begin{aligned} V - v &= (27.354 \pm 0.001) \\ I - i &= (27.057 \pm 0.002) + (0.017 \pm 0.002)\ (V - I) \end{aligned} \tag{6.2}$$

Before calibrating all the other fields to field 1, I performed the short-long exposure calibration of every field. In all the cases only a zero-point was found. An exception is the I band in field 1, which exhibited a mild colour term. The long exposure of field 1 was observed $\sim$ 4 years before the short exposure. The origin of the colour term can be a degradation of the CCD itself, which generally affects more the wavelengths at the edge of the spectrum, such as the I band. The short-long calibrations are shown in Appendix A, figures A.1, A.2, A.3, A.4, A.5, and A.6.

Once I calibrated field 1 and the short-long exposures, I performed an internal calibration between field 1 and the other fields. I identified the commons stars which are contained in the overlapping regions between these (Fig. 2.9). Stars in field 1 became the standard stars for the other fields, which I used to obtain the calibration for the remaining fields. As shown in Fig. 2.9, field F intersects only with field 4. Therefore, I calibrated field 4 to field 1, and then I calibrated field F to field 4. All the plots, representing the internal calibration between the fields, are shown in Appendix A, Fig. A.7, A.8, A.9, A.10, and A.11, with the resulting equations.

The short-long calibrations together with the internal calibrations between the fields were performed for one reason. In this way, they all share the same photometric zero-point. This allowed me to obtain one final catalogue, including all the exposures and all the fields in order to create a unique final catalogue:

1. I used the internal calibration between the exposures, i.e. short and long, to create one catalogue for every field, including the two expo-

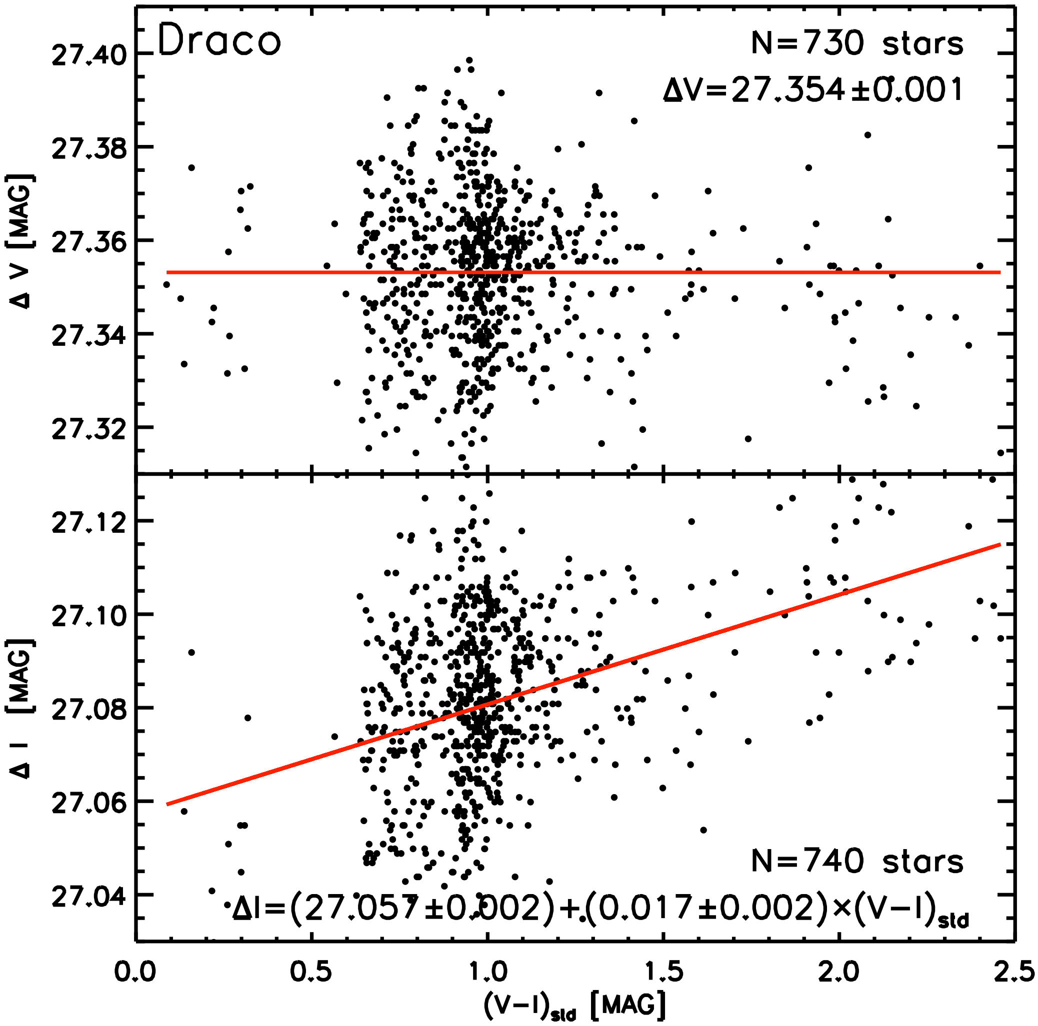

Figure 6.1: Draco calibration for V and I bands (*top* and *bottom panel*, respectively) using Stetson standard stars. $\Delta m = m_{std} - m_{instr}$, where m_{std} is the standard magnitude and m_{instr} is the instrumental magnitude. The red line shows the best fit to the points. The resulting calibration equation, with its uncertainties, is indicated in the figure. The number of stars used to perform the fit is also given.

sures. Objects with $V \leq 20$ and $I \leq 19$ were selected from the short exposure and objects with $V > 20$ and $I > 19$ from the long exposure. This selection was chosen for two reasons. On one hand, the photometric errors were taken into account. On the other hand, I managed to extract the HB magnitudes from one of the catalogues, and thus I avoided to split this branch.

2. The same procedure was adopted to match the fields. I used field 1 as a reference, and then I joint all the other fields, ordering them by number. For the common objects I evaluated the error $\sigma_i = \sqrt{\sigma_{Vi}^2 + \sigma_{Ii}^2}$. Here $i = 1, 2, 3, 4, 5$ denotes the number of the field considered, and $\sigma_{V,I}$ are the errors in the V and I band, respectively. If $\sigma_1 \leq \sigma_i$, the final V, and I magnitudes come from field 1, otherwise they are those of field i, where $i = 2, 3, 4, 5$.

3. In this way I matched the five fields. From this procedure, I excluded field F, which was used only to evaluate the contamination of the field in the CMD of Draco. This is discussed in Section 6.2. The final catalogue contains $\sim 280,000$ objects.

6.2 CMDs, Photometric Errors and Field Decontamination

The CMDs of the galaxy and of the field are shown in Fig. 6.2. Only objects with $\sigma_V \leq 0.2$, $\sigma_I \leq 0.2$ and $|\text{sharp}| \leq 0.25$ were considered stars. In the same figure the photometric errors are shown at every magnitude.

From Fig. 6.2 the strong field contribution to the CMD of Draco is clearly visible. Thanks to the presence of field F, I was able to rely on my own data to perform the decontamination, instead of applying Galactic models (e.g. Besançon or TRILEGAL – Robin et al. 2003; Girardi et al. 2012). The presence of the field limits the study I want to perform. Thus, the first step in my analysis was to evaluate its contribution and then remove it. This process needs to be carried out with high accuracy, since the presence (or absence) of stars in given regions of the CMD leads to completely different results when the SFH is derived. For example, the presence of stars at magnitudes slightly brighter than the sub-giant branch (SGB) can be interpreted as a burst of star formation. However, they may be also associated with a wrong subtraction of the field star contribution at that magnitude.

To decontaminate the field of Draco I used a simple statistical approach. For every bin in colour i and magnitude j I estimated the expected number of field stars, $n^F_{i,j}$, and of stars of the galaxy $N^G_{i,j}$, using the CMDs of the field and of the galaxy, respectively. The number of field stars $n^F_{i,j}$ was normalized to the area covered by the galaxy:

$$N^F_{i,j} = n^F_{i,j} \, \frac{A_5}{A_F} \tag{6.3}$$

where A_5 is the area covered by all the fields and A_F is the area covered by field F. Thus, I calculated the probability $P_{i,j}$ to find a field star in every bin i, j

$$P_{i,j} = \frac{N^F_{i,j}}{N^G_{i,j}} \tag{6.4}$$

In this way I created a probability map for all the colours and magnitudes of the CMD. Finally, I interpolated this discrete map in order to create a continuous function and to avoid the formation of groups of stars randomly distributed across the CMD.

The decontaminated CMD is shown in Fig. 6.3. The result is highly satisfactory, compared to Fig. 6.2. The main evolutionary features are now very well distinguished. Below $I \sim 24.5$ it was not possible to accurately decontaminate the CMD, due to the photometric limit of field F (Fig. 6.2). This region is not going to be used to obtain the SFH. Therefore, this limit does not introduce any limit to the present study.

6.3 Distance to Draco

There are several distance determination methods in the case of resolved stellar systems. Using a CMD, the two methods mainly used are the TRGB and the HB luminosity. The first one is applied in the case of stellar systems which have a populated tip of the RGB, as in the case of NGC 6822. The second method is used mainly to determine the distance to GGCs or systems

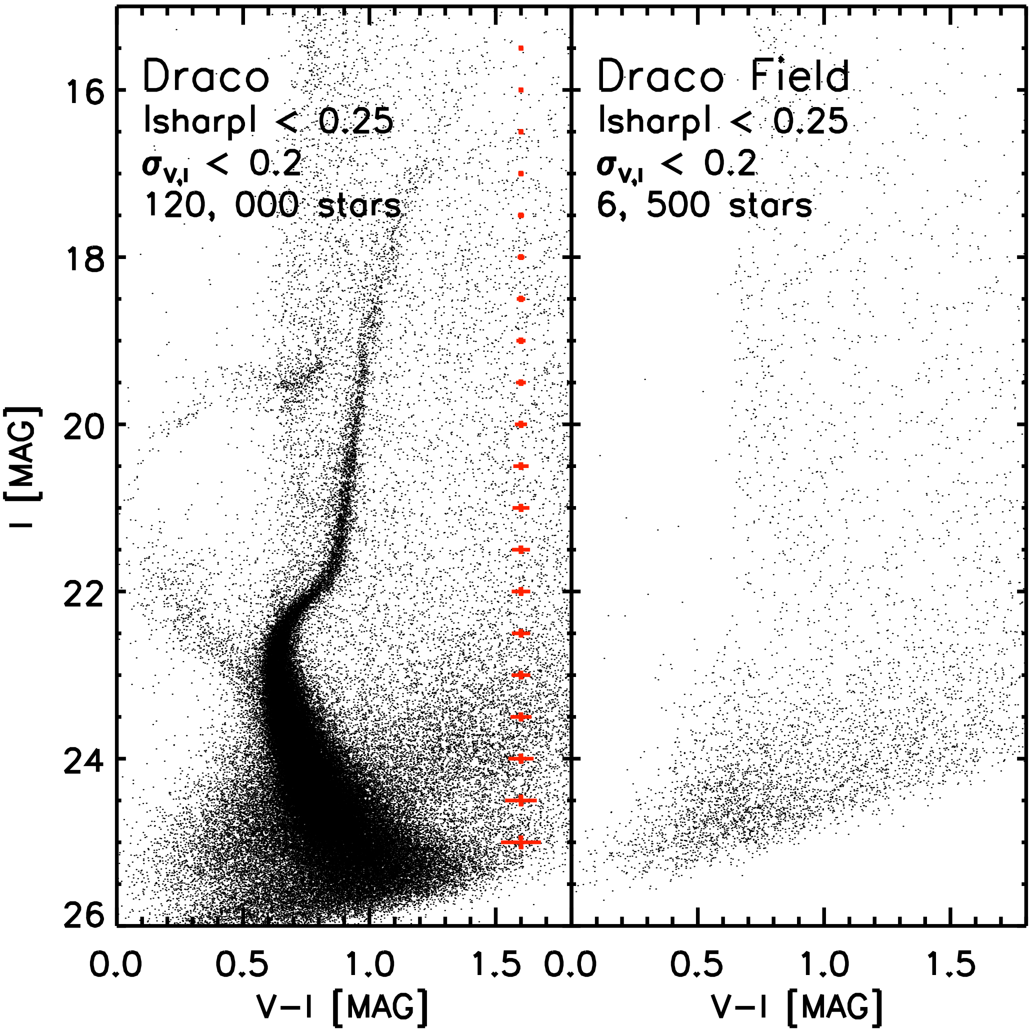

Figure 6.2: Draco $I, V-I$ CMDs. *Left panel:* Resulting CMD obtained with the process described in Section 6.1. Only objects with $\sigma_{\mathrm{V,I}} \leq 0.2$ and $|\mathrm{sharp}| \leq 0.25$ are shown. The resulting number is also indicated in the figure. The photometric errors are shown in red. *Right panel:* This CMD shows only the stars of field F. As already stated, these stars are all assumed to belong to the field, and, hence, need to be subtracted from the CMD on the left. The result is shown in Fig. 6.3. Even in this case the stars were selected according to the same criteria of the *left panel.* The resulting number of stars is shown in the plot.

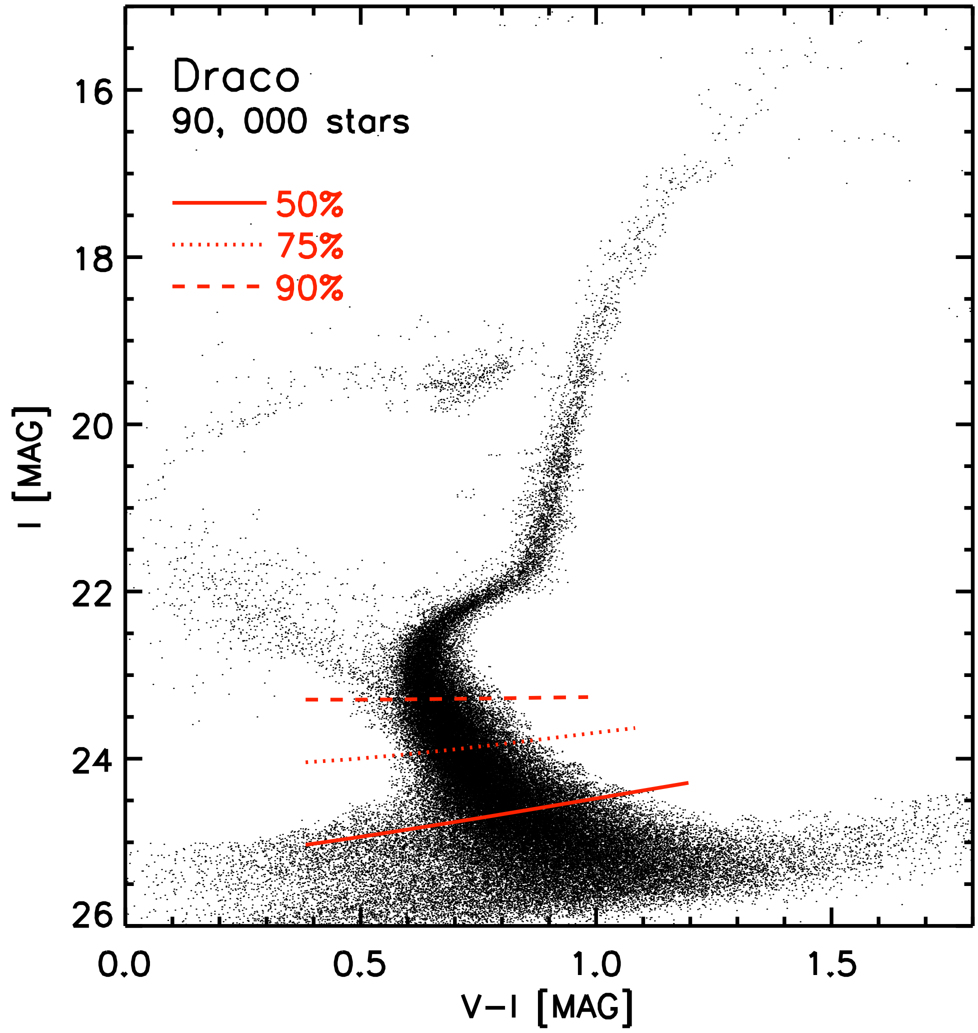

Figure 6.3: Final CMD of Draco. This CMD has been decontaminated using the procedure described in the text. The resulting number of objects is indicated in the figure. The photometric limit of field F does not allow to obtain an accurate decontamination for $I \geq 24.5$. The 90%, 75%, 50% completeness levels are shown in red, with the continuous, dotted, dashed lines respectively.

which are dominated by an old stellar population. This is the method I relied on when determining the distance to Draco.

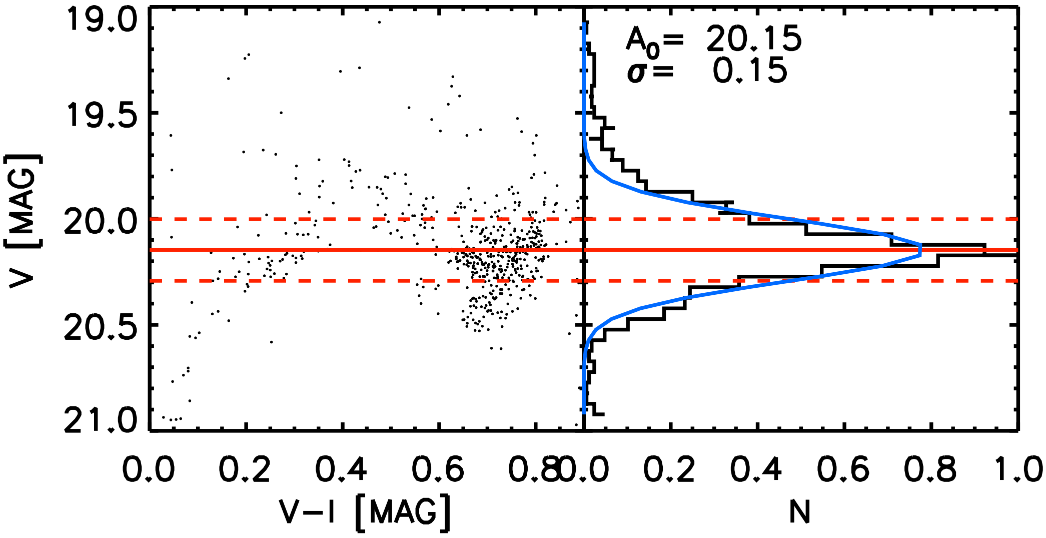

Figure 6.4: HB of Draco. *Left panel:* Zoom in HB region of the CMD. *Right panel:* Colour histogram of the HB. The gaussian fit of the histogram is shown in blue. The maximum of the histogram has been normalized to 1. In both panels the red line identifies its peak, whereas the two red dashed lines are placed at 1σ. The values of the peak, A_0, and of the sigma, σ, are indicated in the figure.

The HB corresponds to the phase in which low mass stars burn He in the central regions. HB stars are good *standard candles* because the luminosity of this evolutionary phase does not depend on the age, but only on the He core mass at the time of the He flash. The He core mass is independent from the initial stellar mass in the case of low-mass stars (Salaris & Cassisi 2005; Cassisi & Salaris 2013). The well populated MS TO in the CMD of Draco discloses that this galaxy is dominated by low-mass stars.

The calibration of the absolute magnitude of the HB is generally given in the V band. In this band, the HB luminosity is constant over a wide range of colours.

As shown in Fig. 6.4, the central part of the HB is not well defined. This is the region of the HB associated to the instability strip, where RR Lyrae variable stars are found. To overcome the uncertainty in the determination of a mean V magnitude for the HB, I performed a gaussian fit on the luminosity function of this branch. This is shown in Fig. 6.4. The magnitude obtained in this way corresponds to that of the RR Lyrae. The V magnitude of the HB of Draco results in $m_V^{HB} = 20.15 \pm 0.15$, where the error is set at 1σ of the gaussian profile. The large error reflects the uncertainty in the procedure described. This value is nicely compatible with those obtained by Aparicio et al. (2001) and Bonanos et al. (2004). According to Bonanos et al. (2004), the absolute magnitude V of the RR Lyrae is $M_V^{RR} = 0.69 \pm 0.13$, for a system with the metallicity of Draco. Therefore $(m-M)_V = 19.5 \pm 0.2$. The reddening obtained by Schlafly & Finkbeiner (2011) is $A_V = 0.074$, hence, the distance modulus obtained is

$$(m - M)_0 = 19.4 \pm 0.2 \tag{6.5}$$

6.4 Preliminary findings on the stellar populations in Draco

Once I determined the distance modulus, I could study the stellar populations in Draco. A first analysis of the CMD of Draco, shown in Fig. 6.3, immediately discloses that this closely resembles that of a GGC. The presence of the old MS TO and of the HB indicates that this galaxy is dominated by an old population. In order to have a first hint on the population in this galaxy, I performed a comparison both with GGCs and with theoretical isochrones.

I selected some GGCs, which cover a range in metallicity, encompassing the metallicity of Draco. Fig. 6.5 shows the comparison with three GGCs, namely M3, M68, and M92. The details of the clusters are listed in Table 6.1.

The slope of the RGB depends mainly on the metallicity. Hence, the comparison of the slopes of this branch can give a hint on this parameter. The comparison in Fig. 6.5 shows that the slope of the RGB of Draco is compatible with that of M68 and M92. On the contrary, the RGB of M3

Table 6.1: For every GGC the distance modulus $(\mathrm{m}-\mathrm{M})_\mathrm{V}$, the extinction $\mathrm{E(B-V)}$, and the metallicity [Fe/H] are given. All these values are from Harris (1996).

GGC	$(\mathrm{m}-\mathrm{M})_\mathrm{V}$	$\mathrm{E(B-V)}$	[Fe/H]
M3	15.07	0.01	-1.50
M68	15.21	0.05	-2.23
M92	14.65	0.02	-2.31

is too faint with respect to that of Draco. This means that the metallicity of this GGC is too high with respect to that of the dSph. The MS TO of Draco agrees with that of the three GGCs. This is an indication that they have roughly the same age. In particular, the age of the GGCs is ≥ 10 Gyr (Brocato et al. 1997; Gnedin & Ostriker 1997; Forbes & Bridges 2010), which is, hence, also expected for Draco.

The second comparison I performed is with the theoretical isochrones. The theoretical isochrones belong to the BaSTI library (Pietrinferni et al. 2004). To perform the comparison I used the distance modulus and reddening found in the previous section. The comparison is shown in Fig. 6.6.

The preliminary results obtained by the comparison with the isochrones, together with those obtained by the GGC, can be described as follows:

- the RGB of Draco is slightly larger than the colour errors expected at the magnitudes of this evolutionary phase (Fig. 6.2). This suggests that a marginal spread in metallicity is present in this galaxy. Fig. 6.6 (*left panel*) shows that the two isochrones of $[\mathrm{Fe/H}] = -2.27$ and -1.50 limit the blue and red edge, respectively, of the RGB of Draco. This means that the metallicities of the stars in this galaxy are between these two values. This is compatible with the results by Kirby et al. (2013b).

- the old MS TO and the SGB give a strong hint on both the metallicity and the age. Inspection of Fig. 6.2 reveals that the TO is compatible with the metallicities obtained from the RGB and ages > 10 Gyr (*right panel*), as the isochrones of $[\mathrm{Fe/H}] = -1.80$ and 13.5 Gyr and

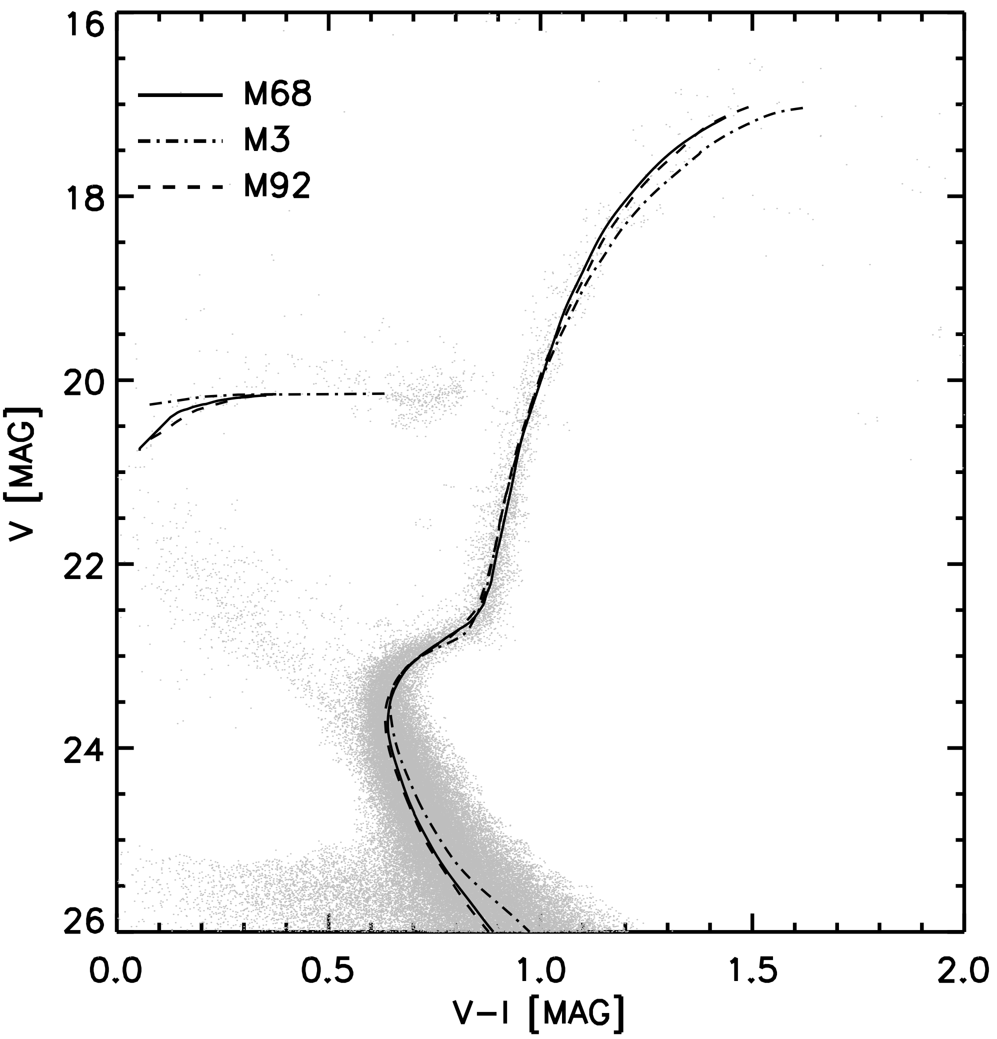

Figure 6.5: Comparison of Draco with three GGCs. Draco is shown in grey. Only the ridge-lines and HB were used. The continuous, dot-dashed, and dashed lines show the location of M68, M3, and M92, respectively. The ridge-lines were calculated on the photometry by Stetson (2000a) of these three GGC.

[Fe/H] = −1.50 and 10.0 Gyr show.

- the stars bluer than the MS TO are well reproduced by a very young population, as the isochrone of [Fe/H] = −1.80 and 2 Gyr shows. That

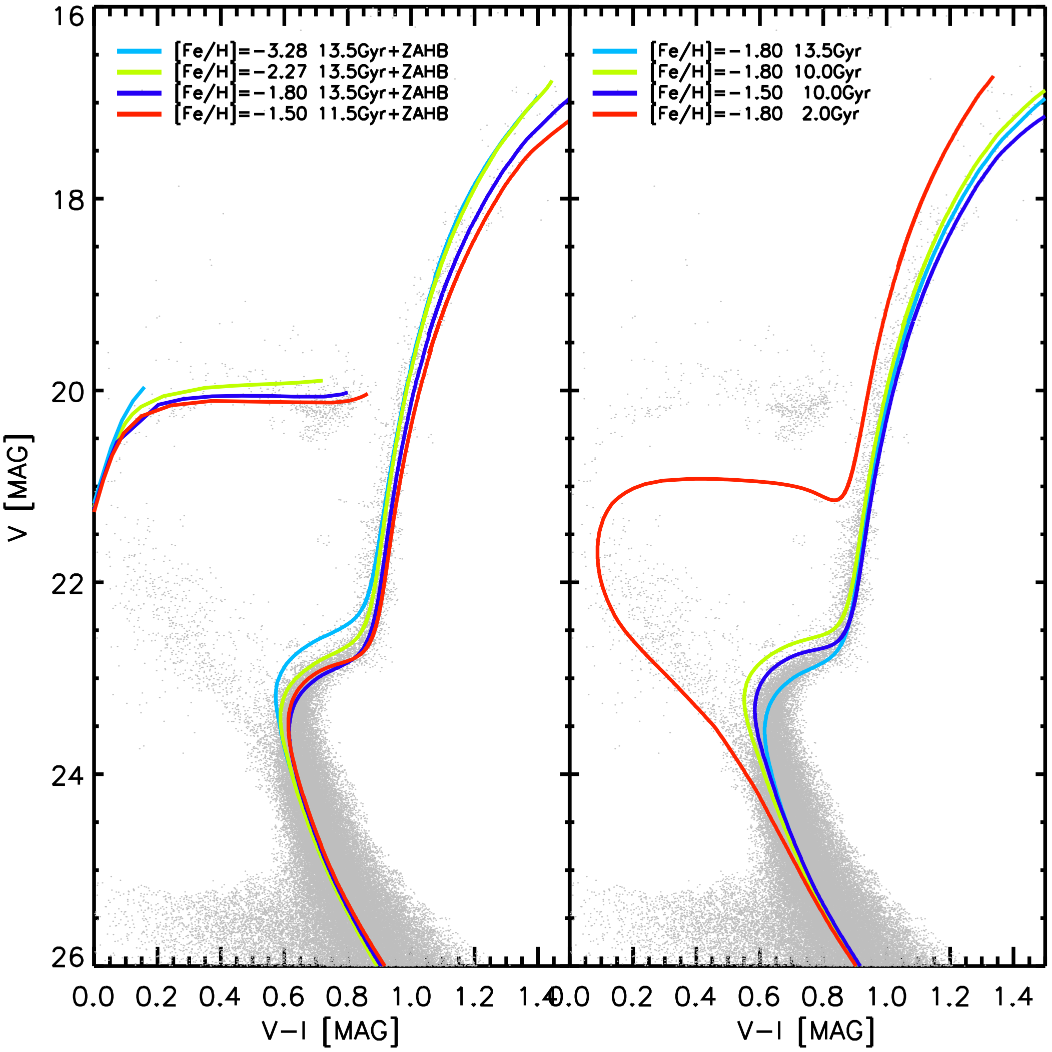

Figure 6.6: Comparison of the CMD of Draco and BaSTI scaled solar theoretical isochrones for different assumptions about age and metallicity. The CMD of Draco is shown in grey. *Left panel:* Lines on the RGB are for [Fe/H] = −3.28, 13.5 Gyr (light-blue line), [Fe/H] = −2.27, 13.5 Gyr (green line), [Fe/H] = −1.80, 13.5 Gyr (blue line), [Fe/H] = −1.5, 11.5 Gyr (red line). In addition, the comparison between HB stars in the CMD and theoretical ZAHB (masses up to $0.9 M_{\odot}$) for four different metallicities, [Fe/H] = −3.28, −2.27, −1.27, −1.50 are shown in light-blue, green, blue, and red, respectively. *Right panel:* Lines on the RGB are for [Fe/H] = −1.80, 13.5 Gyr (light-blue line), 10.0 Gyr (green line), 2.0 Gyr (red line) and [Fe/H] = −1.50, 10.0 Gyr (blue line).

area in the CMD is also compatible with BSS. Detailed studies on this galaxy revealed that these are BSS (Mapelli et al. 2007; Santana et al. 2013). I analysed these stars in Section 6.6.

- the presence of a very well populated HB is a synonym that the bulk of the stellar population in this galaxy is old and metal-poor, as already indicated by the other evolutive features. The ZAHB (Fig. 6.6, *left panel*) with metallicity [Fe/H] $= -1.80$ is the one which best reproduces this evolutive feature.

The comparisons with GGCs and isochrones confirm what was said previously. The bulk of the stars present in Draco are very old (age > 10 Gyr) and metal-poor ($\langle$[Fe/H]$\rangle \sim -2$). In addition, the width of the RGB is compatible with a spread in metallicity.

6.5 The SFH of Draco

Using the IAC method described in Chapter 4 I derived the SFH for Draco. The accuracy of the result depends on the depth of the CMD of the studied galaxy. To obtain the SFH, the regions of the CMD more sensitive to the age, as the MS TO, are used. The CMD presented in the previous sections has above 90% completeness (Fig. 6.3) at the magnitudes of the MS TO. Therefore, with the present dataset an extremely detailed SFH can be derived.

In addition to the CMD, the artificial star tests described in Section 4.2 are applied.

The synthetic CMD was created using IAC-star (Aparicio & Gallart 2004). In this case, the synthetic CMD contains 1.2 10^7 stars with a constant SFR between 0 and 13.5 Gyr and a uniform metallicity distribution between $Z = 0.00001$ and $Z = 0.001$ – corresponding to [Fe/H] $= -3.28$ and -1.27, respectively. The range in metallicity was selected in order to cover all the metallicities of the stars in this galaxy, according to Kirby et al. (2013b). I chose the BaSTI evolutionary library (Pietrinferni et al. 2006), a Kroupa

IMF (Kroupa 2001), and a binary fraction of 30%. The observational effects were simulated in the synthetic CMD, as described in 4.2. Thus, the IAC-pop/MinnIAC (Aparicio & Hidalgo 2009; Hidalgo et al. 2011) were applied to derive the accurate SFH for Draco.

The age bins selected are of 0.5 Gyr for age $\leq$ 0.5Gyr, 1 Gyr for 0.5 $\leq$age$\leq$ 10.5 Gyr, and of 0.5 Gyr for age $\geq$ 10.5 Gyr. The bins in metallicity are of 2 10^{-5} for $10^{-5} \leq Z \leq 7\ 10^{-5}$, 3 10^{-5} for $7\ 10^{-5} \leq Z \leq 10^{-4}$, of 2 10^{-4} for $10^{-4} \leq Z \leq 7\ 10^{-4}$, and 3 10^{-3} for $7\ 10^{-4} \leq Z \leq 10^{-3}$. These values were selected according to the age and metallicity resolution tests. With this method I obtained the smoothed SFH, which includes 24 single SFHs.

Using IAC-pop/MinnIAC codes, I obtained the offset both in magnitude and colour which minimises the effect of the estimates in the external parameters, namely distance, reddening, and photometric zeropoints. These values are those which minimise the χ^2 of the solution and result in $(\Delta\mathrm{col}, \Delta\mathrm{mag}) = (-0.033, 0)$.

The SFH solution obtained is shown in Fig. 6.7. The χ^2 of the solution is 2.7. The function $\psi(\mathrm{t})$ is the stellar mass formed as a function of time, while Ψ_{norm} corresponds to $\psi(\mathrm{t})$ normalized to $\int_0^{13.5} \psi(\mathrm{t})\mathrm{dt}$. In this figure only ages between 8 and 13.5 Gyr are shown, as the last 8 Gyr are not characterised by any significant SF event.

The SF of Draco appears to be characterised by one burst of SF, which took place $\sim$ 12.9 Gyr ago. The width of the burst is $\sim$ 0.5 Gyr. Also the AMR obtained is shown. The mean metallicity of the solution is [Fe/H] $= -1.5 \pm 0.2$. This value appears to be somewhat higher than that measured spectroscopically [Fe/H] $= -1.98 \pm 0.43$ (Kirby et al. 2013b), but it is compatible with their result within the errors. The SFH derived is in good agreement with previous studies (e.g. Aparicio et al. 2001; Weisz et al. 2014). The residuals between the observed and the solved CMDs are displayed in Fig. 6.8.

The SFH derived using the IAC-method is nicely supported by the results described in the previous section.

As discussed in the Section 1.5, LG dSph galaxies of the dimension of Draco are expected to be those affected by the reionization (Grebel & Gal-

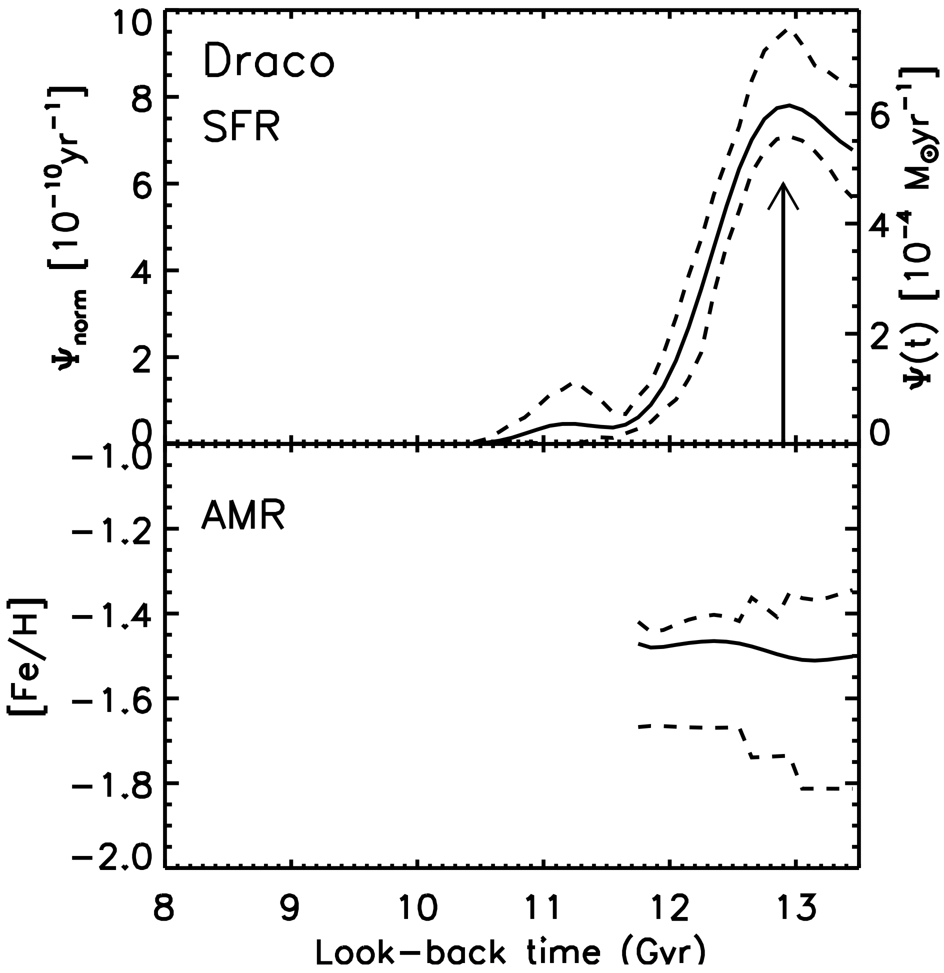

Figure 6.7: *Top panel:* SFR as a function of look-back time. $\Psi_{\rm norm}$ denotes $\psi(t)$ normalized to $\int_0^{13.5} \psi({\rm t}){\rm dt}$. Only the ages between 8 and 13.5 Gyr are shown. The continuous line shows the mean solution obtained by averaging 24 single solutions, whereas the dashed lines show the errors on the solution. The arrow indicates the position of the main burst. *Bottom panel:* AMR for Draco, according to the best SF solution. The continuous line represents the mean metallicity obtained, whereas the dashed line shows the error bars. Only ages between 8 and 13.5 Gyr are shown.

lagher 2004). Reionization is expected to take place at $z_{reioniz} = 6$, which corresponds to ∼ 12.7 Gyr (Wright 2006). A galaxy is considered to be affected by reionization if before this time it has produced the bulk of its stars. The peak of SF at 12.9 Gyr with a width of 0.5 Gyr found in the SFH anal-

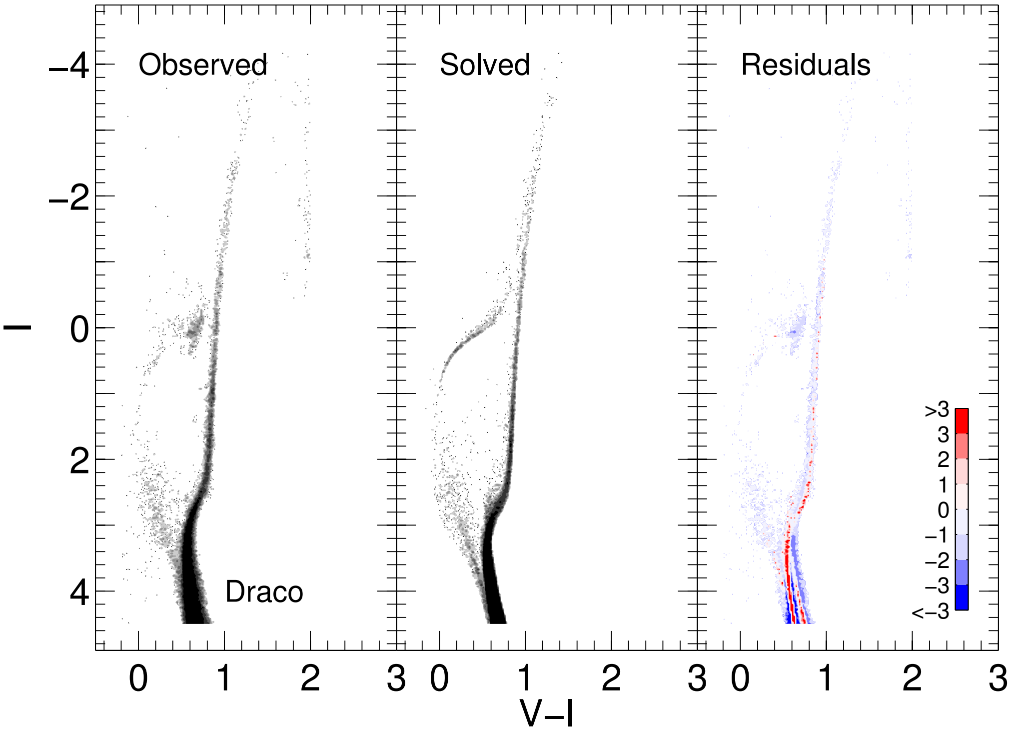

Figure 6.8: *Left panel:* Observed CMD for Draco. *Central panel:* the CMD according to the SF solution produced by IAC-pop/MinnIAC. *Right panel:* The residuals are shown. These are obtained as the difference between the observed and the solution CMDs counted in different bins in units of Poisson errors. The colours correspond to the errors, as shown by the colour scale.

ysis presented here, is in agreement with the predicted effect of reionization. In any case, the reionization effects on dSphs are still controversial, as they cannot be confirmed by a spectroscopic metallicity analysis.

6.6 Radial Gradients

Once I obtained the SFH solution for this galaxy, I looked for the presence of radial gradients in the stellar populations of Draco. The huge dimension of the field allows to study the stellar populations as far out as 3 core radii ($r_c = 9\ arcmin$) of Draco.

Other authors, who studied the stellar population gradients in Draco (e.g.

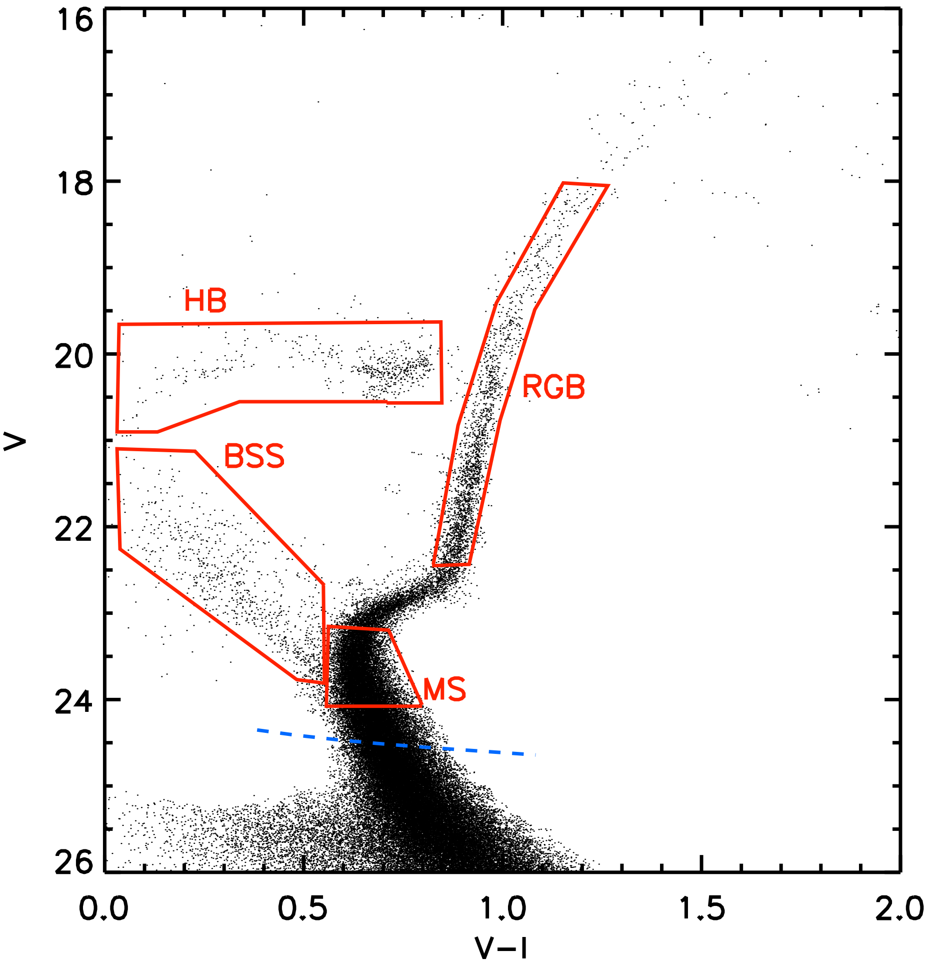

Figure 6.9: CMD of Draco showing the four regions used to study the presence of radial gradients in red and the 75% completeness level in blue.

Aparicio et al. 2001), did not detect any difference in the populations as a function of the distance from the centre.

In the CMD of Draco I selected four regions: the MS, the RGB, the BSS, and the HB. This is shown in Fig. 6.9. I used the eccentricity(ϵ) of Draco and its position angle ($P.A.$) to divide the field of the galaxy into several ellipses, with centres coincident with that of Draco. According to Irwin & Hatzidimitriou (1995) these parameters are $\epsilon = 0.33$ and P.A. $= 82°$.

Table 6.2: For every evolutionary phase the scale length r_0, derived in Fig. 6.10 is given in *arcmin* and *pc*, with the associated errors.

Phase	r_0 $[arcmin]$	r_0 $[pc]$
MS	10.1 ± 0.4	223 ± 28
BSS	11.9 ± 0.5	262 ± 35
RGB	11.0 ± 0.3	244 ± 29
HB	13.0 ± 0.8	287 ± 43

The mean distance of the stars contained within each elliptical annulus was adopted as the radial distance of that area.

I counted the stars in each region of the CMD and in each elliptical annulus. The result is shown in Fig. 6.10, where the counts are given normalised to the area of each annulus.

All the evolutionary phases disclose an exponential profile. For each of these I evaluated the scale length. The values of the scale lengths are listed in Table 6.2, both in arcmin and in parsecs (*pc*), which was obtained using a distance to this galaxy of 75 ± 7 *kpc* as obtained in Section 6.3. The derived scale lengths are consistent within the errors. This is an indication that the stellar populations present in this galaxy are well mixed, hence, there is no evidence for any radial gradients in the stellar populations of Draco. All the regions selected in the CMD have a completeness level over 75% (Fig. 6.9).

In addition, I studied the ratios between BSS, RGB, and HB with respect to MS stars. These are shown in Fig. 6.10 (*bottom panel*). All these ratios appear to follow a flat distribution, with the exception of a small increase associated to the outermost annulus. This is caused by a lower completeness in the outer fields, which affects mainly the MS counts. Therefore, the enhancement is not considered to be relevant.

In particular, I focused on the nature of the stars bluer than the MS TO, in order to confirm that these are not associated to a recent burst of SF. The ratios between BSS and MS stars appears to follow a flat distribution. BSS would be associated to a young MS if they appeared more concentrated in the centre of the galaxy than older stars (Mapelli et al. 2007). In Draco, BSS do not show any clump across the field, as young MS stars would do. Hence, from the present dataset I can confirm that these stars are BSS.

To conclude, Draco appears dominated by one single stellar population, of age ≥ 12.5 Gyr.

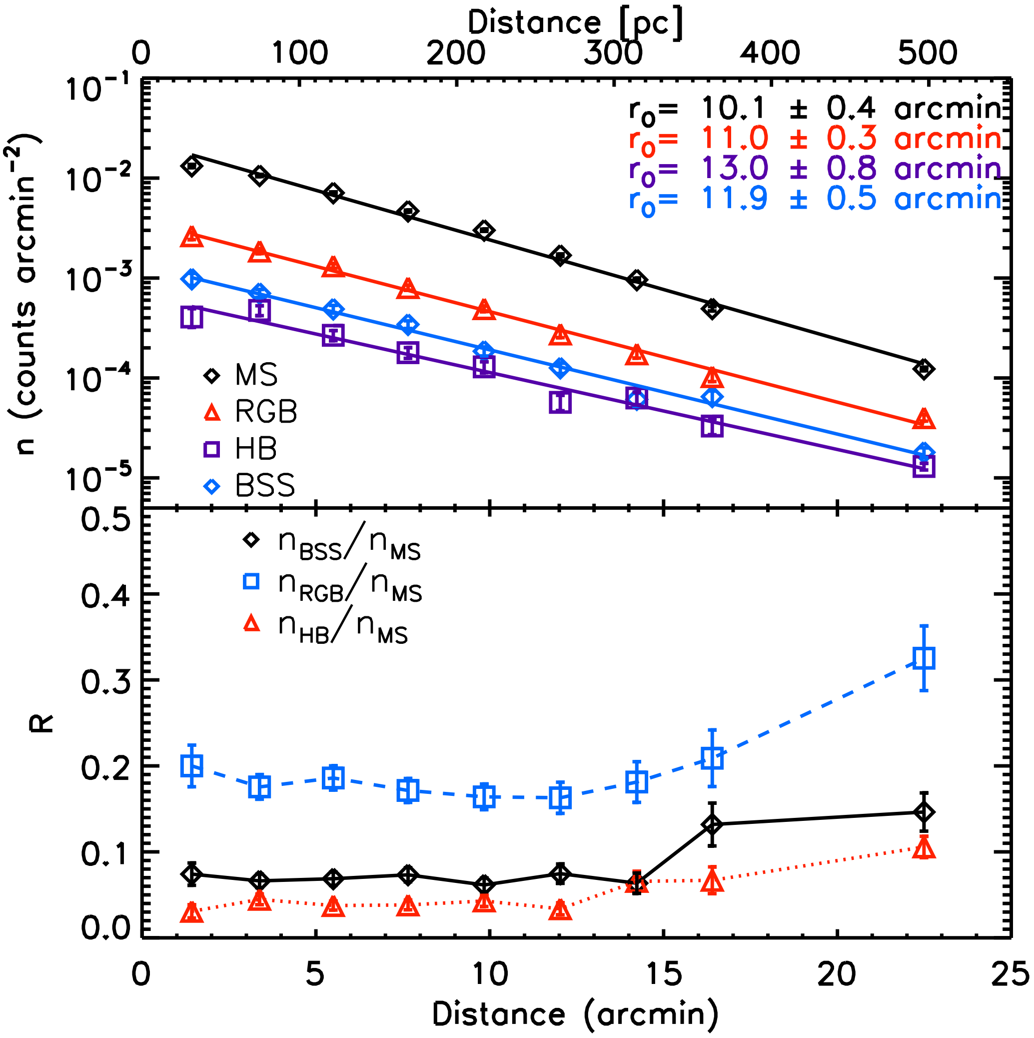

Figure 6.10: *Top panel:* The counts in each elliptical annulus and in each region of the CMD are shown as a function of the distance from the centre of the galaxy in a logarithmic scale, with the associated errors. The distance is shown both in arcmin (*bottom axis*) and in parsecs (*pc*, *top axis*). To obtain the distance from the centre in *pc* I assumed a distance to the galaxy of 76 ± 7 *kpc*, as derived in Section 6.3. The counts are normalised to the area of each ellipse in *arcmin*^{2}. In addition, the best fit to the points is shown. The resulting scale lengths r_0 are indicated in the figure. Both the points and the lines associated to the MS, RGB, HB, and BSS are shown in black, red, violet, and blue, respectively. *Bottom panel:* Ratios between different stellar evolutionary phases shown as a function of the distance from the centre of the galaxy. The ratios between BSS and MS, RGB and MS, and HB and MS are shown in black, blue, and red respectively. The errors are also shown.

Chapter 7

Ursa Minor

In this chapter, I present the analysis of the dSph UMi, starting from ita data calibration in Section 7.1, to the CMD description and distance estimate in Section 7.2. The preliminary study on its stellar populations in Section 7.3 show that there is a discrepancy between Subaru and HST photometries. This difference is widely discussed in Section 7.4. To conclude deeper insights into the stellar populations in this dSph are given in Section 7.5 and 7.6.

7.1 Calibration

The calibration performed in the case of the UMi dSph galaxy is analogous to that of Draco.

Also in the case of UMi, I used Stetson standard stars to calibrate the short exposure of field 1, since the standards are bright and fall mainly in this field. The calibration equation is the same as Equation (6.1). Despite the poor number of stars the coefficients obtained appear to be reliable, according to the errors. The calibration is shown in Fig. 7.1 and the equations result in:

$$\begin{aligned} V - v &= (27.225 \pm 0.007) - (0.009 \pm 0.006)\ (V - I) \qquad (7.1) \\ I - i &= (26.948 \pm 0.005) + (0.029 \pm 0.004)\ (V - I) \end{aligned}$$

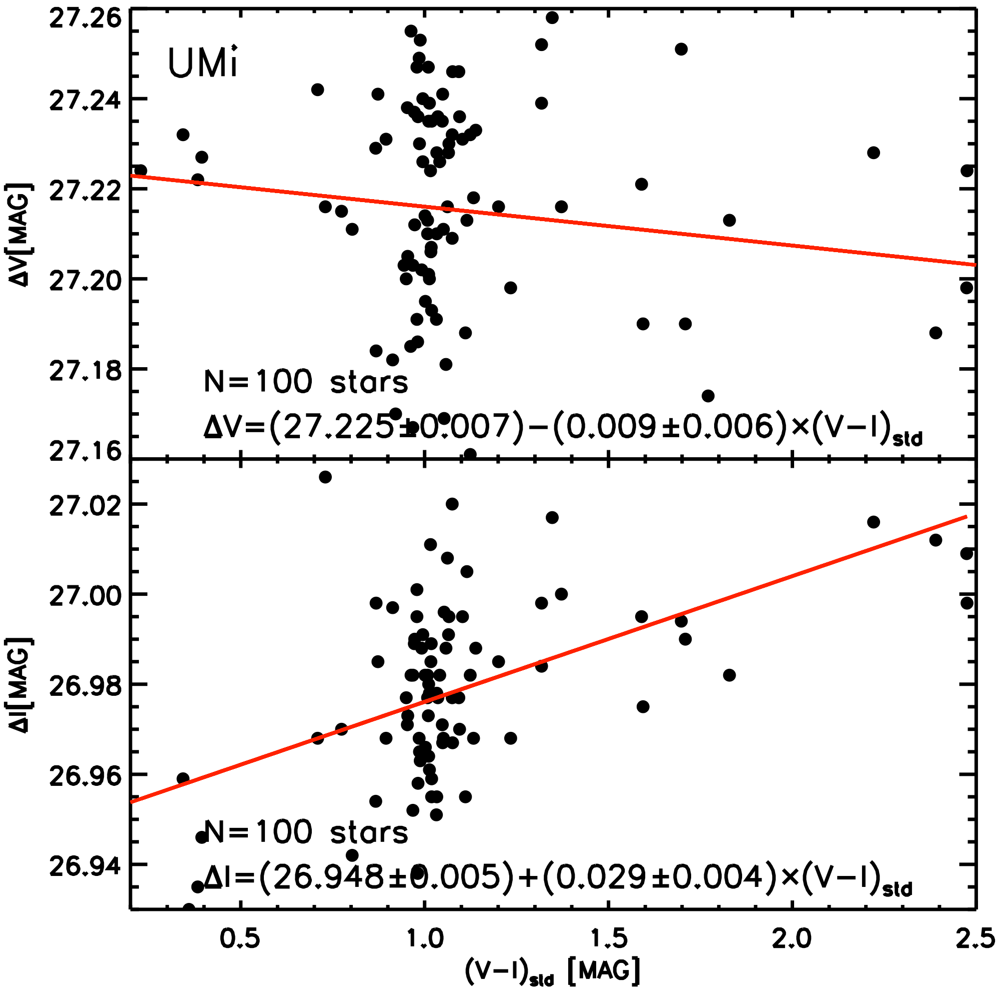

Figure 7.1: UMi calibration for V and I bands (*top* and *bottom panel*, respectively) using Stetson standard stars. $\Delta m = m_{std} - m_{instr}$, where m_{std} is the standard magnitude and m_{instr} is the instrumental magnitude, for V and I. The red line shows the best fit to the points. The resulting calibration equation, with its uncertainties, is indicated in the figure. The number of stars used to perform the fit is also indicated.

I then performed the short-long calibration for the two fields. The resulting calibrations are shown in Fig. A.12 and A.13, in Appendix A. The results resemble those found for Draco: a colour-term was found only in the short-long calibration of field 1. This is a nice confirmation of the result, as the long exposures of Draco were observed together with those of UMi. Approximately 4 years later the short exposures were also obtained together for both galaxies (see Table 2.3 and 2.4).

Once the matching between the two exposures was performed in both the fields, I used the calibrated stars of field 1 as standards for field 2. This was possible thanks to the overlap between the two, as shown in Fig. 2.10. The internal calibration is shown in Appendix A, Fig. A.14. In this way the calibrations of the several exposures share all the same photometric zero-point. Thus, I was able to create one catalogue, which includes all the exposures and all the fields. In order to create a unique final catalogue, I used the same rules applied for Draco:

1. Using the short-long calibration I ended up with one catalogue for every field. The final catalogue was created selecting objects with $V \leq 20.5$ and $I \leq 20$ from the short exposure and objects with $V > 20.5$ and $I > 20$ from the long exposure. The limiting values were chosen for two reasons. On one hand, the photometric errors were taken into account. On the other hand, I extracted the stars belonging to the HB from one of the catalogues, in order to avoid a splitting of this branch.

2. The same procedure was adopted to match the fields. I used field 1 as a reference. For the common objects between fields 1 and 2, I evaluated the error $\sigma_i = \sqrt{\sigma_{Vi}^2 + \sigma_{Ii}^2}$, $(i = 1, 2)$, where σ_V and σ_I are the errors in the V and I band, respectively. If $\sigma_1 \leq \sigma_2$, the final V and I magnitudes are those of field 1, otherwise they are those of field 2.

3. In this way I matched the two fields. The final catalogue contains $\sim 130,000$ objects.

7.2 CMDs, Photometric Errors, Field Decontamination, and Distance to UMi

The CMD resulting from the process described is shown in Fig. 7.2. Only objects which have $\sigma_\mathrm{V} \leq 0.2$, $\sigma_\mathrm{I} \leq 0.2$ and $|\mathrm{sharp}| \leq 0.25$ are selected to be stars. The resulting photometric errors are shown in Fig. 7.2 at every magnitude level.

At odds with Draco, UMi is affected by an only moderate contamination from field stars. However, to obtain a detailed SFH for this galaxy, I also had to remove the field stars contribution from the CMD of UMi.

To decontaminate the CMD of UMi, I carried out a very similar procedure to that described in Section 6.2. The only exception is that in the dataset of UMi a region dominated by field stars has not been observed. To overcome this problem I used the areas of the CMD dominated by field stars, which are easily identified as those where no evolutionary features are present, e.g. MS, RGB. In these areas I counted the number of field stars $N^F_{i,j}$, in every bin of colour i and magnitude j. Then, in every bin i, j in the CMD which contains evolutionary features I counted the number of stars $n^G_{i,j}$. Therefore, I used the surrounding areas dominated by field stars to interpolate around the position i, j and to estimate the number of field stars $N^F_{i,j}$ in each bin. From this I evaluated the number of stars belonging to the galaxy as $N^G_{i,j} = n^G_{i,j} - N^F_{i,j}$. In this way, I created the probability map defined in Equation 6.4 for every bin i, j. Once the probability map was created, I repeated the same process described for Draco. The resulting CMD is shown in Fig. 7.2 (*right panel*).

I did not decontaminate the CMD for $I \geq 24$. At this magnitude level photometry starts to become significantly incomplete, and, hence, these magnitudes are not used to derive the SFH.

The CMD of UMi looks very similar to that of Draco. Also in this case I determined the distance to this galaxy using the HB. In Section 6.3 further details on the HB standard candle are given.

Following the same method described in Section 6.3, I estimate the apparent mean magnitude of the HB to be $m_V^{HB} = 19.91 \pm 0.12$. As shown in Fig. 7.3, these values are the peak and σ of the gaussian, which best fits the histogram in V magnitude of the HB. The absolute magnitude for a galaxy of the metallicity of UMi is $M_V^{RR} = 0.66 \pm 0.15$ (Gould & Popowski 1998; Bonanos et al. 2004) and $A_V = 0.088$ (Schlafly & Finkbeiner 2011). Hence the distance to UMi results in

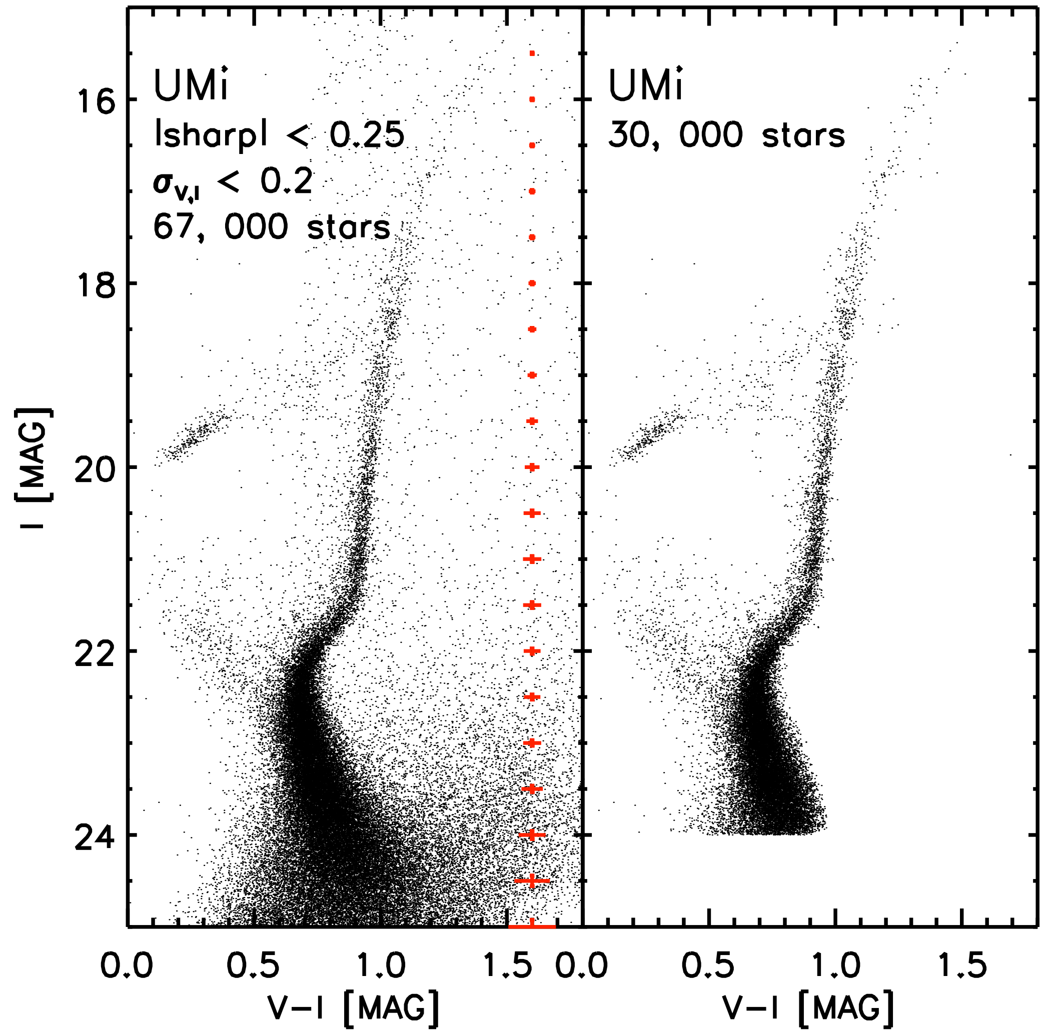

Figure 7.2: UMi $I, V-I$ CMDs. *Left panel:* Resulting CMD obtained by following the procedure described in Section 7.1. Only objects with $\sigma_{\rm V,I} \leq 0.2$ and $|{\rm sharp}| \leq 0.25$ are shown. The resulting number of objects is indicated in the figure. The photometric errors are shown in red. *Right panel:* CMD resulting from the decontamination. Stars with $I \geq 24$ were not included in the figure, because they were not used in the analysis of this galaxy. The resulting number of stars is indicated in the figure.

$$(m-M)_0 = 19.2 \pm 0.2 \tag{7.2}$$

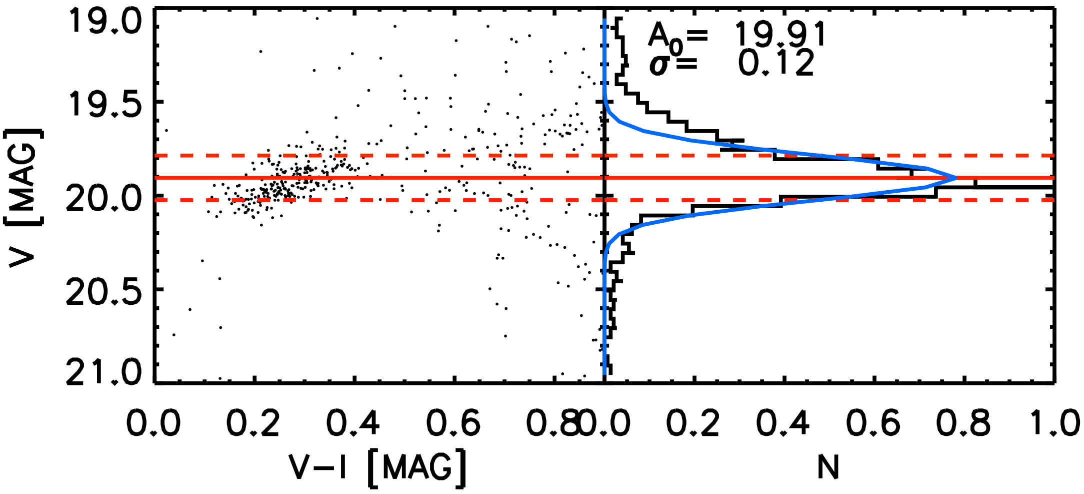

Figure 7.3: HB of UMi. *Left panel:* Zoom into the HB region in the $V, V-I$ CMD. *Right panel:* Colour histogram of the HB. The gaussian fit of the histogram is shown in blue. The maximum of the histogram has been normalized to the unity. In both panels the red line identifies its peak, whereas the two red dashed lines are placed at 1σ. The values of the peak, A_0, and of the sigma, σ, are indicated in the figure.

7.3 Preliminary findings on the stellar populations in UMi

In the following step, I analysed the stellar populations in the UMi dSph galaxy. A first analysis of Fig. 7.2 immediately discloses that the CMD of this galaxy resembles that of a GGC. This is the first hint that the bulk of the star formation in UMi took place at very early ages.

To obtain a closer insight into the stellar populations of this galaxy, I performed a comparison with both GGC and a set of theoretical isochrones.

The comparison with GGC is shown in Fig. 7.4. The three GGC selected are the same presented in Section 6.4, whose details are listed in Table 6.1. The comparison confirms what was previously observed: the CMD of UMi resembles very closely that of a GGC. As in the case of Draco, the RGB slope shows that the metallicity of this dSph is similar to that of M68 and

M92. On the contrary, M3 appears to be too metal-rich. Hence, UMi is a metal-poor dwarf galaxy.

When the oldest MS TO of UMi is compared to the GGCs the result is surprising. The TO and the MS of UMi turn out to be somewhat redder than that of the GC.

After having compared UMi with the GGC, I compared it with some theoretical isochrones. The result is shown in Fig. 7.5. The isochrones belong to the BaSTI database (Pietrinferni et al. 2004) and cover a wide range in age and metallicity.

The preliminary results obtained from the comparison with the isochrones, together with those obtained by the GGC, can be described as follows:

- the RGB of UMi is marginally wider than the photometric errors at the magnitudes of this branch, as shown in Fig. 7.2. This means that UMi is affected by a spread in metallicity. The slope of the RGB is fundamental to obtain information about the mean metallicity. Inspection of Fig. 7.5 (*left panel*) shows that the mean metallicity appears to be between [Fe/H] $= -3.28$ and -1.80, as these two isochrones encompass all the stars in the RGB of UMi. Based on this result I assume a mean metallicity of [Fe/H] ~ -2. This is compatible with the results of Kirby et al. (2013b). The isochrone with [Fe/H] $= -1.50$ does not match the slope of the RGB of UMi.

- when compared to the isochrones, the old MS TO and the SGB confirm the result found with GGCs. The SGB of UMi is somewhat too short and it results in a MS and a MS TO redder than theoretical models predict. However, the more luminous part does not show any sign of anomaly. This result is discussed is Section 7.4.

- the stars bluer than the MS TO are well reproduced by a very young population, as the isochrone of [Fe/H] $= -1.80$ and 2 Gyr shows. As in the case of Draco, these stars have been identified to be BSS by, e.g., Mapelli et al. (2007); Santana et al. (2013). In Section 7.6, I investigate the nature of these stars.

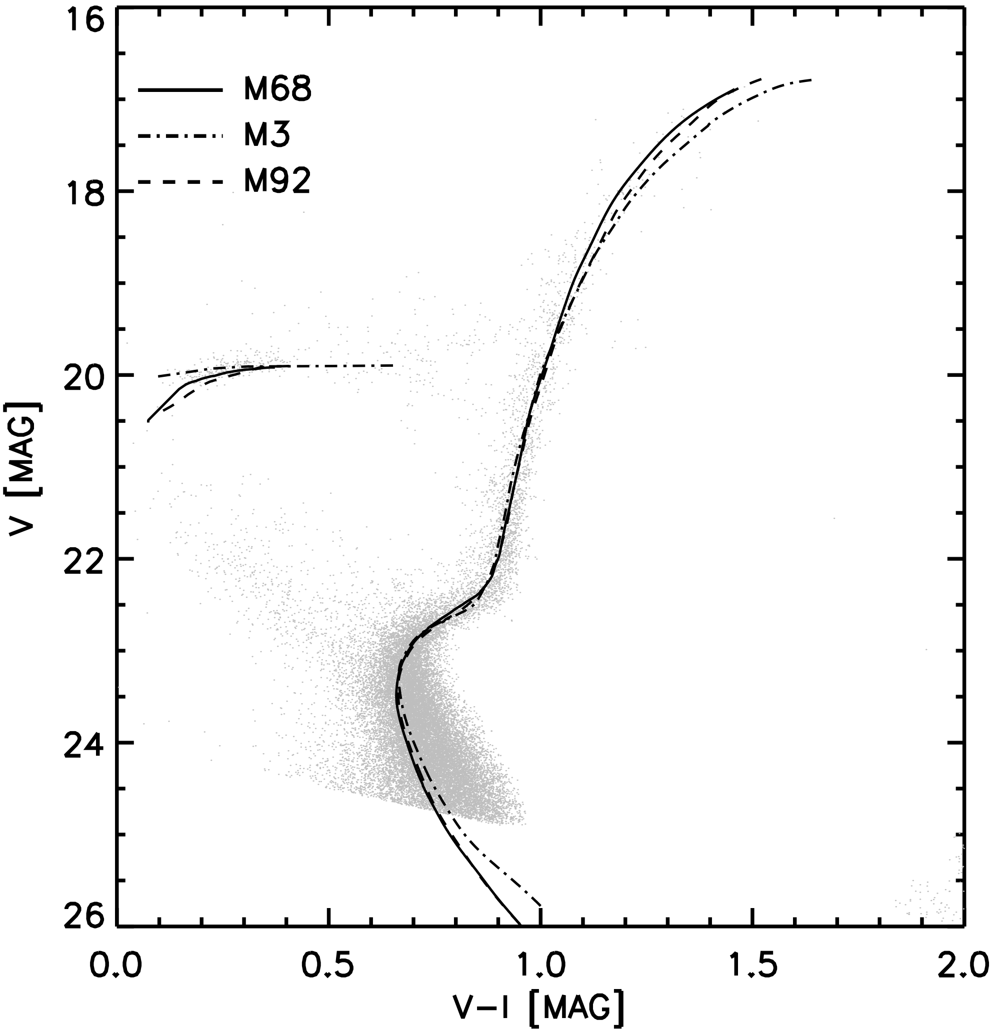

Figure 7.4: Comparison of UMi with three GGCs. UMi is shown in grey. Only the ridge-lines and HB were used. The continuous, dot-dashed, and dashed lines show the location of M68, M3, and M92, respectively. The ridge-lines were calculated on the photometry by Stetson (2000a) of these three GGC.

- the HB is very well populated in the case of UMi. The ZAHB (Fig. 7.5, *left panel*) with metallicity [Fe/H] $= -2.27$ is the one which best reproduces this evolutionary feature, confirming that this galaxy is dom-

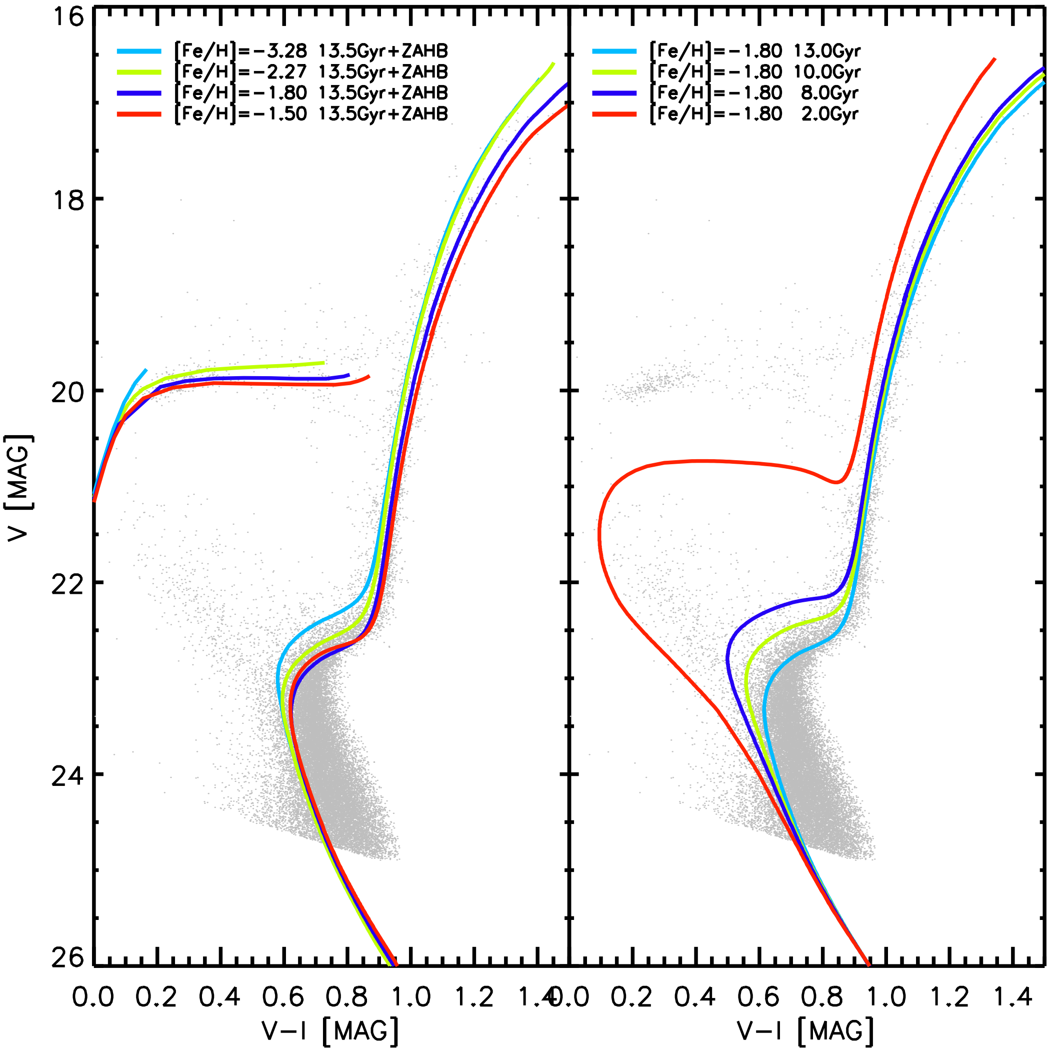

Figure 7.5: Comparison of the CMD of UMi with BaSTI scaled solar theoretical isochrones of different assumptions about age and metallicity. The CMD of UMi is shown in grey. *Left panel:* Lines on the RGB are for [Fe/H] = −3.28, 13.5 Gyr (light-blue line), [Fe/H] = −2.27, 13.5 Gyr (green line), [Fe/H] = −1.80, 13.5 Gyr (blue line), [Fe/H] = −1.5, 11.5 Gyr (red line). In addition, the comparison between HB stars in the CMD and theoretical ZAHBs (masses up to 0.9 $M_{\odot}$) for the four different metallicities, [Fe/H] = −3.28, −2.27, −1.27, −1.50 are shown in light-blue, green, blue, and red, respectively. *Right panel:* Lines on the RGB are for [Fe/H] = −1.80, 13.5 Gyr (light-blue line), 10.0 Gyr (green line), 2.0 Gyr (red line) and [Fe/H] = −1.50, 10.0 Gyr (blue line).

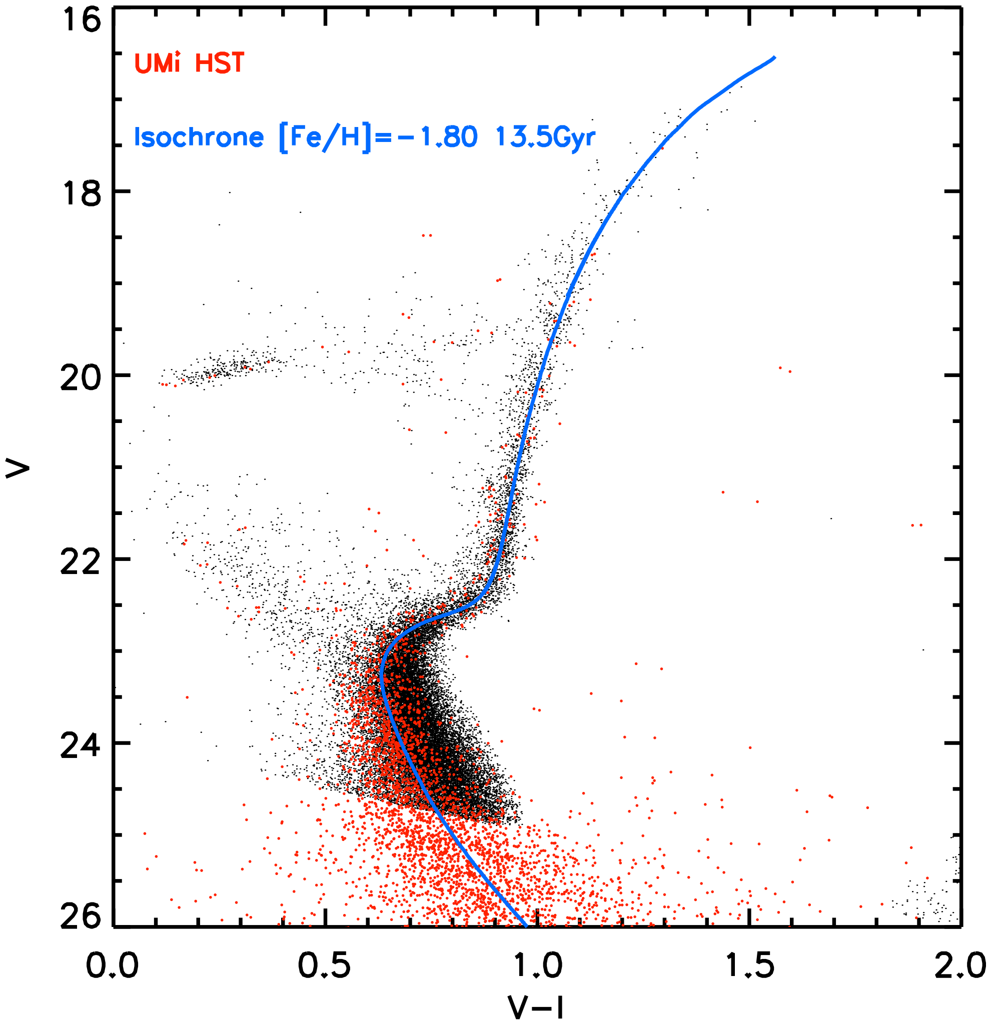

Figure 7.6: Comparison between Subaru and HST photometry (Holtzman et al. 2006), shown in black and red respectively. In addition, the isochrone of [Fe/H] = −1.80 and 13.5 Gyr is shown in blue.

inated by a metal-poor population.

7.4 Analysis of the discrepancy in UMi data

The comparisons with GGC and isochrones have revealed the presence of a difference between theoretical models and observations. The fundamental question to answer is whether this discrepancy is due to a real effect, i.e. some peculiarity into this system, or if it is some kind of non linearity within the data.

The only photometry available which can help to solve this issue has been published by Holtzman et al. (2006). The authors performed the photometry of a huge quantity of HST data[1], which include UMi. The result of the comparison is shown in Fig. 7.6. Inspection of this figure immediately reveals that HST data follow the theoretical models. In addition, it appears that the brighter part of the CMD introduced in present study is in agreement with the photometry by Holtzman et al. (2006). Therefore, the preliminary findings derived from the bright part of the CMD, i.e. the HB and RGB, can be considered reliable.

The discrepancy between the Subaru and HST data does not allow to derive the SFH for this galaxy. The most important area used to derive the SFH is the TO region, but this is also the region mostly affected by the disagreement.

The identification of the stars in common between the HST and Subaru observations would immediately shed light on the difference between the two photometries. However, the difference between the pixel scale of the two cameras (see for comparison Table 2.1) combined with the absence of the atmosphere in the case of the HST photometry, introduce an ambiguity in the identification of the common stars.

Figure 7.6 rules out that the effect found is intrinsic to this galaxy, i.e. caused by some kind of peculiarity in its chemical abundances. For this reason, I requested new observations, as discussed in Sections 2.3.3 and 2.3.4. By using these data I investigate two possibilities:

---

[1] The photometry of the dwarf galaxies by Holtzman et al. (2006) is collected at the webpage http://astronomy.nmsu.edu/holtz/archival/html/lg.html. The authors converted WFPC2/HST to standard Johnson magnitudes.

- the calibration equation found in Section 7.1 is not reliable. Thus a new calibration and additional standards are needed. The Subaru standard fields observed together with UMi are affected by large uncertainties, as discussed in Appendix B. Hence, the IAC80 data were requested to carry out a new calibration of the Subaru photometry.

- if this calibration turns out to be reliable, then a non linearity of the camera at faint magnitudes remains the only explanation for the mismatch. For this reason, I requested additional observations with the NOT telescope, to cover magnitudes as faint as the MS TO.

The IAC80 data were reduced according to the procedure in Chapter 3.

I started deriving the calibration equation for the night of the observation. For a given photometric band m, where m is V or I in the studied case, the calibration equation is the following:

$$m_{cal} = m_{instr} + k_m \ AM + ZP_m + C_m \ (V - I) \tag{7.3}$$

where ZP_m is the zero-point, C_m is the colour coefficient, $V - I$ is the colour, k_m is the extinction coefficient in a photometric band for the night of the observation, and AM is the air mass of the observation listed in Table 2.5. m_{instr} is the instrumental magnitude, defined as

$$m_{instr} = m_{phot} + AP + 2.5 \ \log(t_{exp}) \tag{7.4}$$

Here m_{phot} is the magnitude obtained from the photometry, AP is the aperture correction, and t_{exp} is the exposure time in seconds (see Table 2.5). I estimated the aperture correction fixing the aperture at 25 pixels, according to the growth curves.

Figure 7.7 shows the derivation of the extinction and of the calibration coefficients, which result in

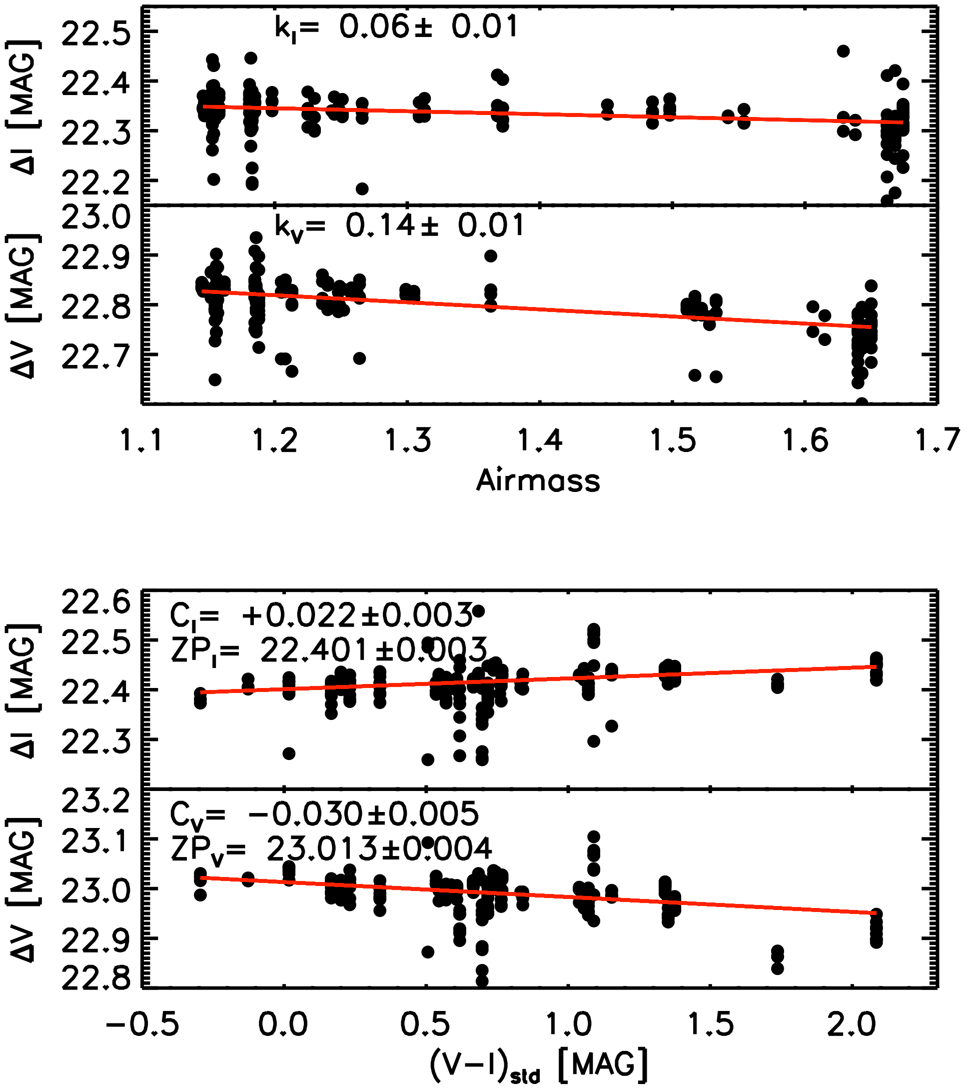

Figure 7.7: Calibration equation for the IAC80 data. *Top panels:* Δm as a function of the airmass for both the I (*upper panel*) and V band (*lower panel*). $\Delta m = m_{std} - m_{instr}$, where m_{std} is the standard magnitude and m_{instr} is the instrumental magnitude, for V and I. The best fit is shown in red. The resulting extinction coefficients are indicated in the figures, with the associated errors. *Bottom panels:* Calibration equations for the two photometric bands obtained by using the extinction coefficients derived. The best fit is indicated in red and the resulting coefficients are shown in the figure with their uncertainties.

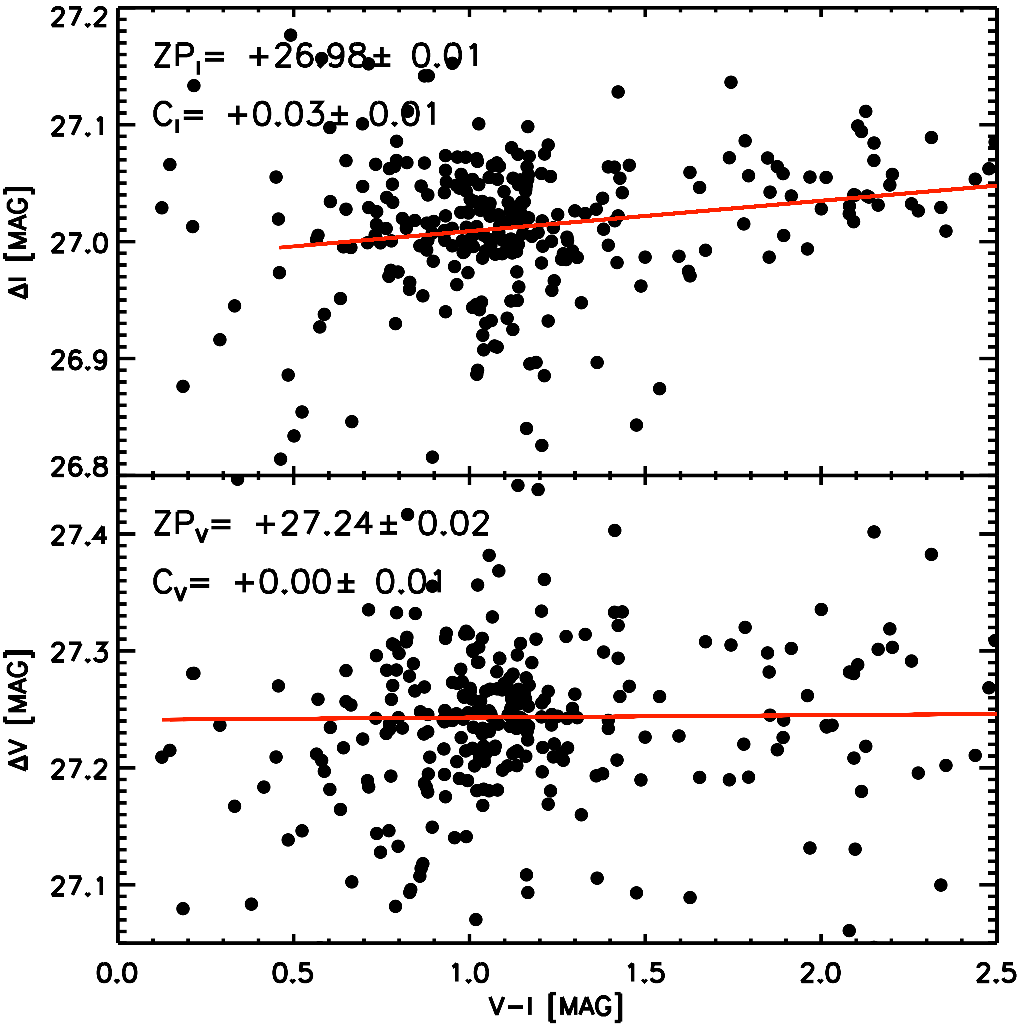

Figure 7.8: Calibration of Subaru UMi data using the UMi IAC80 stars as standards, for the V and I band (*bottom* and *top panels*, respectively). The coefficients obtained from the best fit (in red) are indicated in the figure, with the associated errors.

$$\begin{aligned} V - v &= (0.14 \pm 0.01)\ AM + (23.013 \pm 0.004) + \\ &\quad -(0.030 \pm 0.005)\ (V - I) \qquad (7.5) \\ I - i &= (0.06 \pm 0.01)\ AM + (22.401 \pm 0.03) + \\ &\quad +(0.022 \pm 0.003)\ (V - I) \end{aligned}$$

Using these equations I calibrated the UMi observations performed with the IAC80. Hence, these stars are used as standard stars to calibrate UMi. The resulting calibration equation has the same structure as Equation 6.1. The result is shown in Fig. 7.8. The resulting calibration equations are:

$$\begin{aligned} V - v &= 27.24 \pm 0.02 \\ I - i &= (26.98 \pm 0.01) + (0.03 \pm 0.01)\ (V - I) \end{aligned} \tag{7.6}$$

The derived coefficients are in good agreement with those originating from the calibration with Stetson standards (Equations 7.1).

The good agreement between the two calibrations, which have been obtained with two independent methods and data, confirms the result previously found and does not solve the discrepancy with the HST data.

Thus, having confirmed that the data calibration is robust, a possible non-linearity of the camera is the only reason remaining to explain the disagreement. So far, all the calibrations have been performed on the short exposure, and then the short-long calibration has been used (Fig. A.12). Hence, to minimize the errors of this transition I used the NOT data, which are deep enough to immediately calibrate the long exposure.

The NOT data were reduced according to the process described in Section 3. The photometry results to be as deep as the SGB, and it was calibrated using the IAC80 standards. In the regime of overlap between the NOT and the Subaru, the data are linear the one with respect to the other.

However, the photometry does not reach as deep as the MS of UMi. In addition, to derive the SFH the degree of accuracy of the calibration has to be higher than that provided by these data.

7.5 SGB investigation

The photometry derived with the Subaru for UMi turned out not to be reliable in order to derive the SFH. Nonetheless the data are still suitable to perform star counts. Hence, to obtain some hints on the duration of the

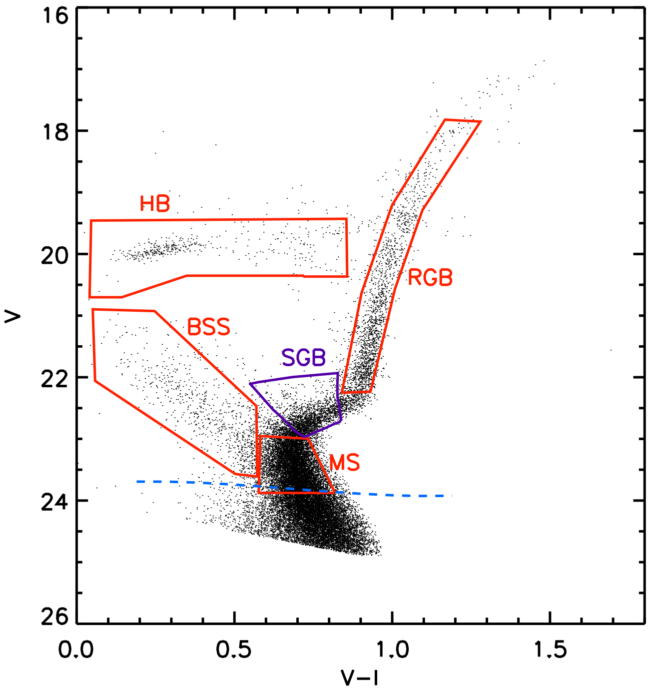

Figure 7.9: CMD of UMi showing the adopted SGB region (in violet). The four regions in red are used to study the presence of radial gradients in Section 7.6. The 90% completeness level is indicated in blue.

main stellar burst in this galaxy I focused on its SGB. The dispersion of the stars in this branch gives a hint on the relative duration of the main burst of SF in UMi.

I selected a region in the observed CMD corresponding to this branch, as shown in Fig. 7.9. I computed the ridge-line and I evaluated the dispersion of the stars with respect to this line. In this manner, I built a histogram centered on the ridge-line, and I estimated the width of its best fitting gaussian, which results in $\sigma_{obs} = 0.053$.

Using IAC-star (Aparicio & Gallart 2004) I created a synthetic CMD (sCMD) with the same metallicity dispersion as that derived by Kirby et al. (2013b) in their spectroscopic study (Fig. 7.10). Using this sCMD, I selected several age bins, starting from 13.5 Gyr. Using only the stars in the SGB box, I calculated the ridge-line for every age bin, and built the histogram of

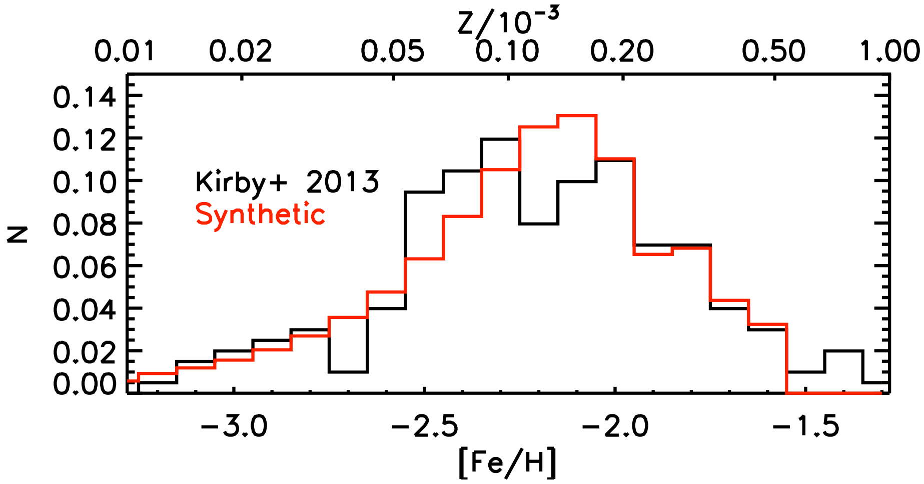

Figure 7.10: Comparison between the normalized histograms of the metallicitis of the stars in UMi (black) by Kirby et al. (2013b) and of the synthetic stars (red) of the sCMD created with IAC-star. The *bottom axis* shows the metallicity in [Fe/H], while the *top axis* shows the associated Z value.

Table 7.1: Age bins, starting from 13.5 Gyr ago, resulting σ of the gaussian that fits best the dispersion of the synthetic SGB, and probability P obtained from a two sample KS test (see text). The bottom line gives the σ of the observed CMD.

Age bin (Gyr)	σ	P
0.05	0.047	0.49
0.15	0.050	0.77
0.25	0.049	0.68
0.50	0.050	0.77
1.00	0.052	1.00
1.50	0.052	1.00
2.00	0.059	0.49
2.50	0.064	0.06
3.50	0.080	0.00
Observed	0.053	

the dispersion of the stars with respect to this line. The age bins and the associated σ obtained are listed in Table 7.1.

A comparison between the σ of the observed and synthetic SGBs immediately discloses that the age bins of 1 and 1.5 Gyr have the most similar

Table 7.2: For every evolutionary phase the scale length r_0, derived in Fig. 7.11 is given in arcmin and *pc*, with the associated errors.

Phase	r_0 [arcmin]	r_0 [pc]
MS	15.1 ± 1.8	304 ± 64
BSS	17.5 ± 2.2	351 ± 77
RGB	14.6 ± 1.0	295 ± 48
HB	18.6 ± 1.9	374 ± 73

width. In order to constrain the width in age of the burst more in detail, I performed a two-sample Kolmogorov-Smirnov test (KS) between the observed and synthetic gaussian profiles. This test yields the probability that the two distributions are related. The result is given in Table 7.1.

The KS test allows to conclude that the duration of the burst lasted for at least 0.15 Gyr and not longer than 2 Gyr. The present dataset for UMi does not allow to obtain an absolute value of the age, but only of the relative width of the main burst of SF. The duration of the star burst is compatible with the previous results, e.g. Carrera et al. (2002); Ikuta & Arimoto (2002).

7.6 Radial Gradients

To conclude the analysis of this galaxy, I investigated its radial gradients. Also in this case the discrepancy found does not affect the result, as this analysis is based on star counts. The present dataset allows to study the populations as far out as $\sim 2r_c$.

The study of radial gradients of UMi can disclose interesting results, as this galaxy is well known for being tidally disrupted by the MW. However, in previous studies no radial gradients were found in this galaxy (e.g. Carrera et al. 2002; Mapelli et al. 2007).

I applied the same procedure as I did for Draco. I began by selecting four regions associated to four different evolutionary features, as shown in Fig. 7.9. The four regions all have a completeness level of more than 90%.

Using the P.A. and ellipticity I built a set of elliptical annuli centered on the centre of UMi. These values are $\epsilon = 0.56$ and P.A. $= 53°$ (Irwin &

Hatzidimitriou 1995). In every elliptical annulus and CMD region I counted the stars, and I normalised them to the area of the associated annulus. The result is shown in Fig. 7.11. In all the cases clear exponential profiles are found.

For every evolutionary phase I calculated the scale lengths r_0 of its exponential profile. The resulting values are listed in Table 7.2, both in arcmin and in parsecs (*pc*). To obtain the scale lengths in *pc*, I assumed a distance to UMi of 69.2 ± 6.5 *kpc*, as derived in Section 7.2. All the r_0 are compatible with each other.

In addition, I considered the ratios between BSS, RGB, and HB with respect to the MS (Fig. 7.11). The ratios do not exhibit any trend. In particular, the stars bluer than the MS TO appear well mixed with the stars of the other evolutionary phases, meaning that these are confirmed to be BSS stars, as stated by, e.g., (Mapelli et al. 2007).

These results mean that none of the evolutionary phases appears to be distributed in a different way from the others. Hence, UMi appears to be dominated by a unique stellar population, which was born by a very narrow burst, which lasted, at most, 2 Gyr. Moreover, with my dataset I can confirm that the stars bluer than the MS TO are BSS.

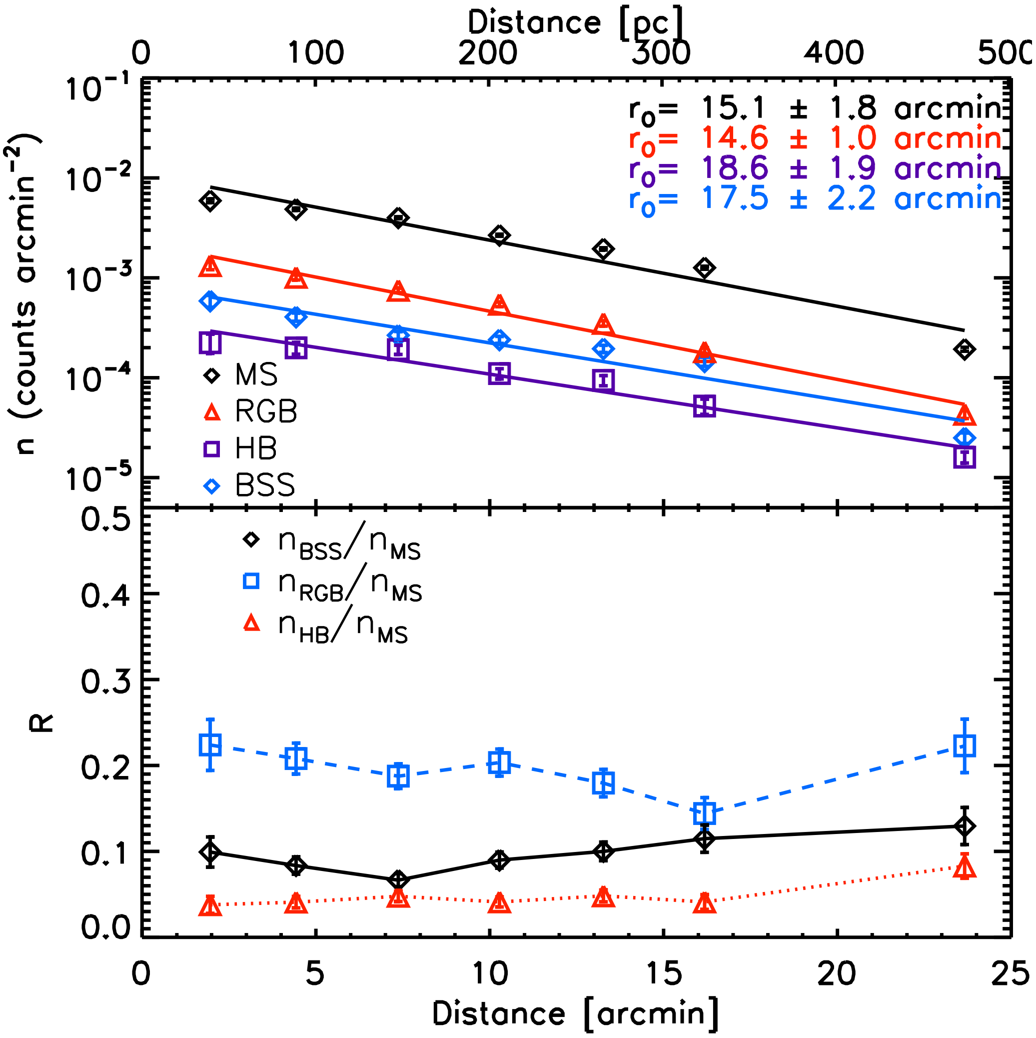

Figure 7.11: *Top panel:* The counts is each elliptical annulus in logarithmic scale and in each region of the CMD are shown as a function of the distance from the centre of the galaxy, together with the associated errors. The distance is shown both in arcmin (*bottom axis*) and in parsecs (*pc*, *top axis*). To obtain the distance from the centre in *pc* I assumed a distance to the galaxy of 69.2 ± 6.5 *kpc*, as derived in Section 7.2. The counts are normalised to the area of each annulus in $arcmin^2$. In addition, the best fit to the points is shown. The resulting scale lengths r_0 are indicated in the figure. Both the points and the lines of the MS, RGB, HB, and BSS are shown in black, red, violet, and blue, respectively. *Bottom panel:* The ratios between the number of stars of BSS and MS, RGB and MS, and HB and MS are shown in black, blue, and red respectively. The errors are also displayed.

Chapter 8

Hercules and Future Work

In this chapter, the UFD Her is presented. In Section 8.1 the calibration is presented, whereas in Sections 8.2 and 8.3 the CMD is introduced, the distance to this galaxy is estimated, and the stellar populations are discussed. In Section 8.4 I describe the future work and plans.

8.1 Calibration

Stetson (2000a, 2005) standards stars are not available in the case of Her. Therefore, to calibrate the photometric data of the UFD Her I relied on the IAC80 observations described in Section 2.3.3. The calibration equation for the night of observation has already been derived in Section 7.4 and it is shown in Fig. 7.7, and the calibration equation is given in Equation 7.6.

Using these equations I calibrated the observations of Her of that night, and then I used them as standard stars for the short exposure of the Subaru observations. Hence, I calibrated these data as shown in Fig. 8.1. For both the bands V and I only a zero point is found:

$$\begin{aligned} V - v &= 27.35 \pm 0.03 \qquad (8.1) \\ I - i &= 27.05 \pm 0.04 \end{aligned}$$

I then performed the short-long calibration for the two fields. These are shown in Fig. A.15 and A.16. Also in this case no colour term was found. Thus, I used the stars in field 1 to calibrate field 2W.

Once I calibrated all the catalogues, I merged them in order to have one catalogue for this galaxy. To perform the matching I executed the same procedure described for UMi in Section 7.1. In this case the matching magnitudes were $V = 20$ and $I = 19$.

8.2 CMDs, Photometric Errors, and Distance to Her

The resulting CMD is shown in Fig. 8.2. Despite of not being as deep as those presented previously for Draco and UMi, the CMD of Her however reaches $\sim 2mag$ below the MS TO. The photometric errors are shown in the figure.

The field contamination in the CMD of Her is too high to perform a statistical decontamination as in the cases of Draco and UMi. However its HB appears well detached from field stars. For this reason I estimated the distance to this galaxy using this branch.

The HB of Her is very poorly populated, but it can be easily identified. I created a histogram based on the selected the stars of the HB. Thus the mean magnitude obtained is $m_V^{HB} = 21.73 \pm 0.12$. I considered an error of 3σ of the best fitting gaussian shown in Fig. 8.3, to take the small number of stars into account. The RR Lyrae magnitude expected for a system of the mean metallicity of Her, [Fe/H] $= -2.3$, is $M_V^{RR} = 0.60 \pm 0.15$ (Gould & Popowski 1998; Bonanos et al. 2004). Hence, the distance to this galaxy results in

$$(m - M)_0 = 20.8 \pm 0.2 \tag{8.2}$$

where the extinction has been set to $A_V = 0.171$ (Schlafly & Finkbeiner 2011). This result is compatible with previous distance estimates (e.g. Adén et al. 2009; Coleman et al. 2007).

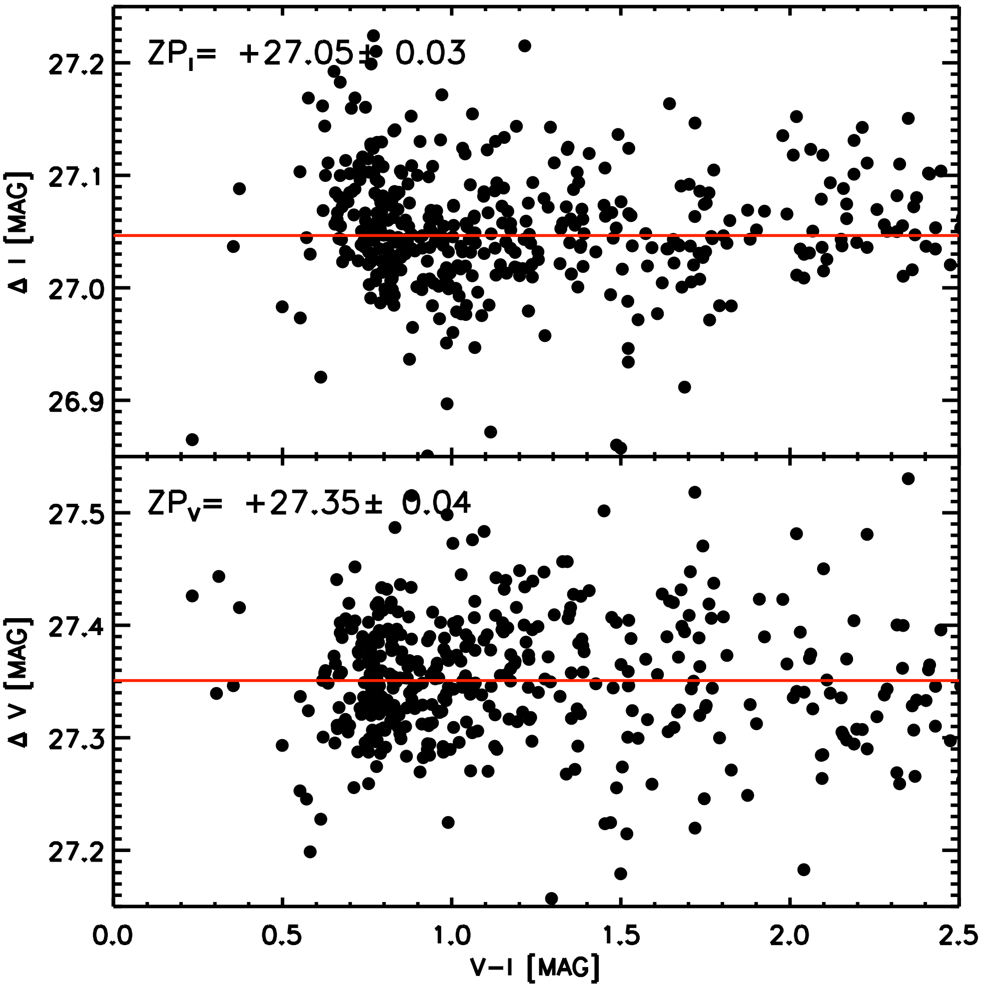

Figure 8.1: Her calibration for V and I bands (*top* and *bottom panel*, respectively) using IAC80 standard stars. In both panels $\Delta m = m_{std} - m_{instr}$, where m_{std} is the standard magnitude and m_{instr} is the instrumental magnitude, for V and I. The red line shows the best fit to the points. The resulting calibration equation, with its uncertainties, is indicated in the figure.

8.3 Findings on the stellar populations in Her

To study the stellar populations in this galaxy I consider the CMD shown in Fig. 8.2 (*right panel*), where only stars within 2 r_c, with $r_c = 4.74$ *arcmin* (Coleman et al. 2007), are considered. In this way the field contamination is

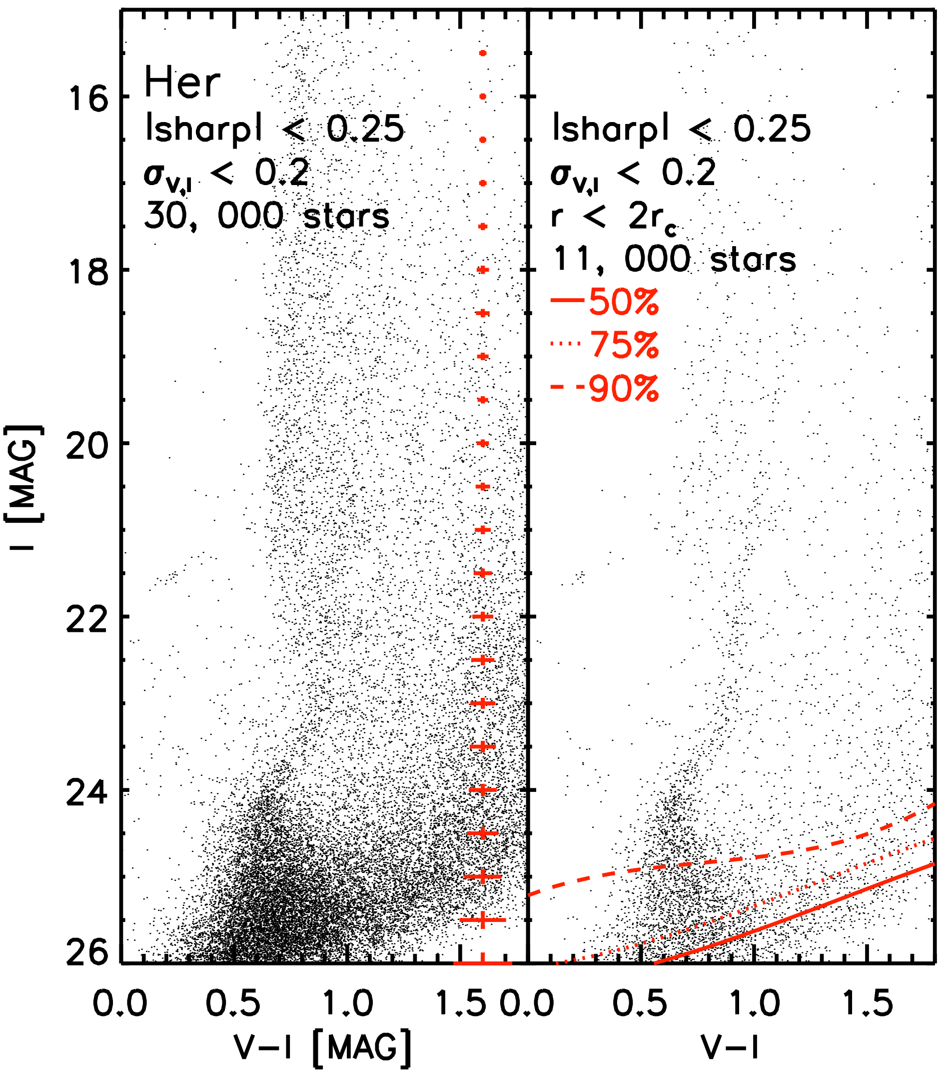

Figure 8.2: Her $I, V-I$ CMDs. Only objects with $\sigma_{\rm V,I} \leq 0.2$ and $|\text{sharp}| \leq 0.25$ are shown. *Left panel:* Resulting CMD obtained by following the procedure described in Section 7.1. The resulting number of objects is indicated in the figure. The photometric errors are shown in red. *Right panel*: Stars within 2 r_c, where $r_c = 4.74$ *arcmin* (Coleman et al. 2007). The number of stars is indicated in the figure. The 90%, 75%, and 50% completeness levels are shown in red, with a dashed, dotted, and continuous line, respectively.

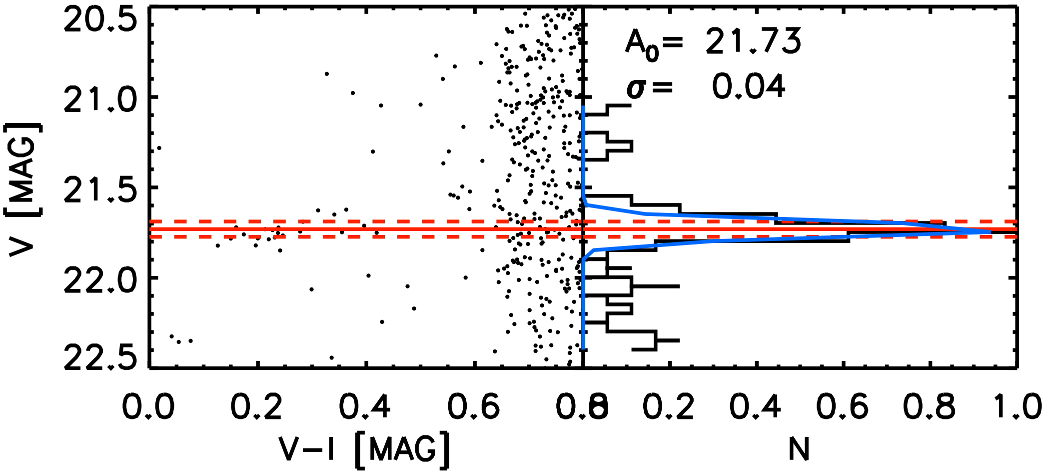

Figure 8.3: HB of UMi. *Left panel:* Zoom of the HB region in the $V, V-I$ CMD. *Right panel:* Colour histogram of the HB. The gaussian fit of the histogram is shown in blue. The maximum of the histogram has been normalized to 1. In both panels the red line identifies its peak, whereas the two red dashed lines are placed at 1σ. The values of the peak, A_0, and of the sigma, σ, are indicated in the figure.

minimised.

In order to investigate the stellar populations in Her, I compared its CMD with that of GGCs and a set of isochrones, as shown in Fig. 8.4. The GGCs selected are those listed in Table 6.1.

The comparison with the M68 and M92 shows a very good agreement with the slope of the RGB of Her. On the contrary, the RGB of M3 appears to be somewhat too faint with respect to that of this UFD. Also the MS TO of the GGCs appears to fit well the MS TO of Her.

The comparison with the isochrones (Fig. 8.4, *right panel*) discloses very similar results, which can be summarised as follows:

- the RGB is well reproduced by the isochrones with metallicities between [Fe/H] = −3.28 and −1.80, which appear to include all the RGB stars of Her. This result is in very good agreement with the spectroscopic results published (e.g. Kirby et al. 2013b; Fabrizio et al. 2014).

- the old MS TO and the SGB appear to be very well constrained by the isochrone of [Fe/H] = -2.27 and 13.5 Gyr, whereas the isochrone of the same metallicity and 12.0 Gyr appear too luminous. This indicates that the lower limit of the age of the stars in Her is ~ 12 Gyr.

- the HB is very poorly populated, but it confirms that the mean metallicity obtained with the RGB is a good approximation.

- a small population of stars bluer than the MS TO is found, which are identified as BSS (Santana et al. 2013).

To conclude, this galaxy appears to be dominated by an old (age ≥ 12 Gyr), very metal poor population ($\langle$[Fe/H]$\rangle = -2.27$).

For this galaxy I did not derive the SFH, because the photometry is shallower than that of Draco and UMi.

8.4 Future Work

The study of stellar populations in the LG is fundamental, especially the analysis of small systems as Her and the UFDs.

In this thesis I presented a complete study of NGC 6822 and Draco, whereas the analysis of UMi and Her turned out to be somewhat limited by the present datasets. For this reason, I am planning to perform the photometry of the HST data for these two galaxies in order to derive the SFH using the IAC-method.

Despite the small field of view, the HST data are those which allow to reach the faintest magnitudes with the highest completeness. In addition, a huge amount of data exists for the LG dwarfs in the HST archive. Hence, by combining these data with the highly efficient IAC-method to derive the SFHs, it will be possible to study in great detail the formation and evolution of these systems. Using data from the same telescope, the same photometric package, and the same code to derive the SFH, will lead to results which are directly comparable between each other.

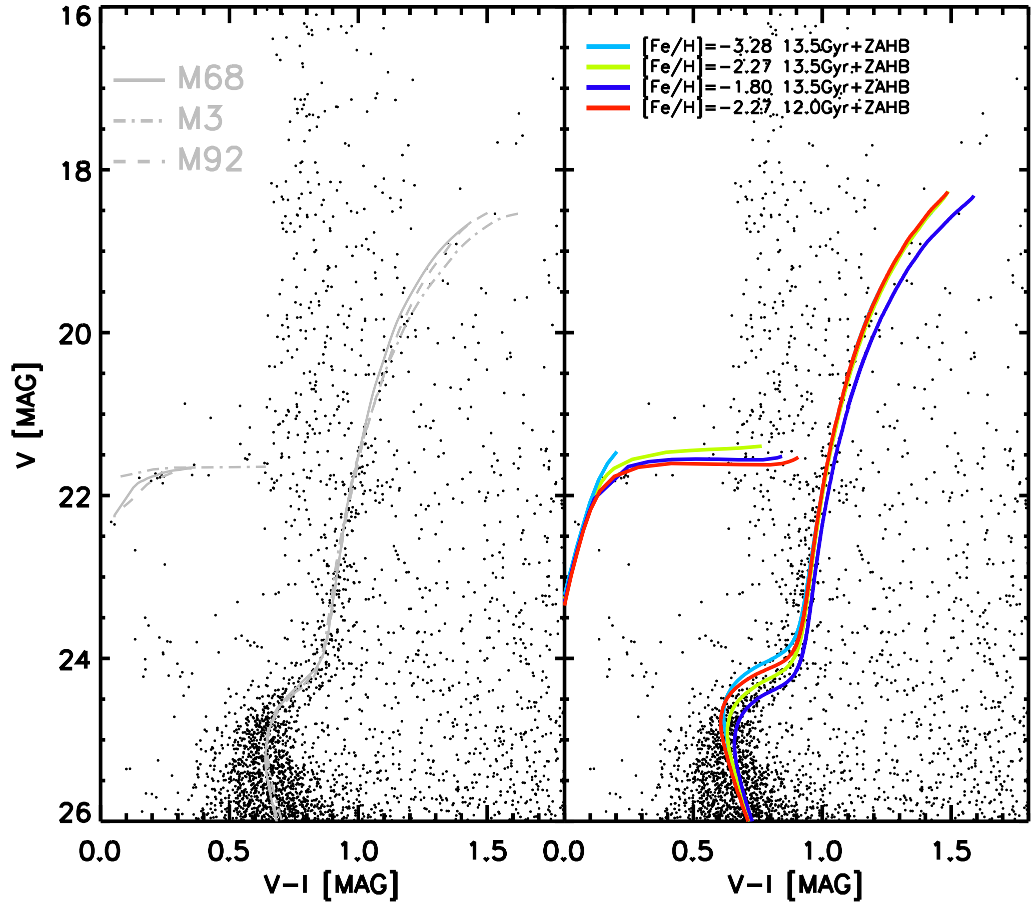

Figure 8.4: *Left panel:* Comparison of Her with three GGCs. Only the ridge-lines and the HB were used. The continuous, dot-dashed, and dashed lines show the location of M68, M3, and M92, respectively. The ridge-lines were calculated using the photometry by Stetson (2000a) of these three GGC. *Right panel:* Comparison between the CMD of Her and BaSTI scaled solar theoretical isochrones for different assumptions about age and metallicity. Lines on the RGB are for [Fe/H] = −3.28, 13.5 Gyr (light-blue line), [Fe/H] = −2.27, 13.5 Gyr (green line), [Fe/H] = −1.80, 13.5 Gyr (blue line), [Fe/H] = −2.27, 12 Gyr (red line). In addition, the comparison between HB stars in the CMD and theoretical ZAHB (masses up to $0.9M_{\odot}$) for four different metallicities, [Fe/H] = −3.28, −2.27, −1.27, −1.50 are shown in light-blue, green, blue, and red, respectively.

A complete study of the SFH in the dwarf galaxies of the LG is essential to gain a deeper understanding of LG cosmology and stellar evolutionary theories.

Chapter 9

Conclusions

In this thesis I studied some dwarf galaxies of the LG. The study of the nearby dwarf galaxies is fundamental as they represent perfect laboratories for testing both evolutionary and cosmological models.

The set of data I used includes all morphological types of dwarf galaxies present in the LG. In all the cases I performed the photometry using DAOPHOT (Stetson 1987). For two of the four galaxies in the sample I derived a very accurate SFH, using the IAC-method, which consists in IAC-star/IAC-pop/MinnIAC (Aparicio & Gallart 2004; Aparicio & Hidalgo 2009; Hidalgo et al. 2011).

The main results can be summarised as follows:

- **NGC 6822**. For this dwarf irregular galaxy six fields observed with the HST telescope were available. These cover the main body of this galaxy, and, hence, offer a good opportunity to study its populations, focusing on the presence of radial gradients. The data set does not reach below the MS TO, therefore the SFH was very accurate only at very recent epochs. The SFH discloses an enhancement in the SFR in the past 500 Myr in Fields 1 and 3, which are the outermost and innermost fields in the north-western side of NGC 6822. All the other fields show a decreasing SFR at very recent epochs. I then studied the radial gradients in this galaxy, selecting two time intervals. One of these samples the very young population and includes ages between 0 and

0.5 Gyr ago. The other encompasses the intermediate-old population, with ages between 0.5 and 13.5 Gyr. Both these populations show clear exponential profiles, whose scale lengths are perfectly compatible. An exception is found in the cases of Fields 1 and 3, whose young populations clearly exceed that of the other fields. This is the most relevant result obtained for this galaxy, which indicates that maybe we are sampling incipient spiral arms associated with these two fields. In addition, I derived the AMR. The metallicity grows with time, and no sign of radial gradient was found. The mean metallicity obtained is in very good agreement with the recent spectroscopic results by (Kirby et al. 2013b).

- **Draco**. This dSph was observed with the Subaru telescope. The observations were divided into six fields. One of these fields was used to decontaminate the CMD of Draco, which is affected by a strong field contamination. The resulting CMD was used to derive the distance to this galaxy, which results in $(\mathrm{m}-\mathrm{M})_0 = 19.4 \pm 0.2$, as well as the SFH. This shows that the history of Draco was characterised by a unique burst of SF, which took place at a very old epoch $\sim$ 12.9 Gyr ago, and shows a full width of $\sim$ 1 Gyr. This is the most accurate estimate of the age and width of the burst of SF in this galaxy, obtained so far. The SFH of Draco is compatible with a quenching of it SF due to the cosmic reionization, as it formed the majority of stars before 12.7 Gyr ago. This effect is still controversial as a counterpart in the spectroscopical metallicity estimate is not found. The mean metallicity derived is higher than what was found spectroscopically by Kirby et al. (2013b), but the result is compatible within the errors. Once I derived the SFH, I studied the radial gradients in this galaxy. The huge field of the observations allows to study its populations as far out as 3 r_c, selecting four evolutionary phases (MS, RGB, HB, BSS). In all the cases an exponential profile is found. For these I calculated the scale lengths, which are compatible within the errors. This confirms that Draco is composed by only one very old stellar population, in good agreement with previous findings (e.g. Aparicio et al. 2001). In addition, I studied the radial distribution of the stars bluer than the MS TO, and found that they follow a flat distribution. Thus, these blue stars are BSS, as previously found (Mapelli et al. 2007).

- **UMi**. The observations of UMi were carried out with the Subaru telescope in two fields. As in the case of Draco, I decontaminated the CMD of this galaxy using a statistical approach. The distance to this galaxy was found to be $(\mathrm{m}-\mathrm{M})_0 = 19.2 \pm 0.2$. The comparison with GGC and BaSTI isochrones (Pietrinferni et al. 2004) discloses that there is a discrepancy with the observed CMD, which consists in a MS redder than expected. I investigated this effect, trying to understand if it was something peculiar in the galaxy, or some kind of non linearity in the data. The first possibility is immediately ruled out when a comparison with the HST photometry of the same galaxy is performed (Holtzman et al. 2006). Thus, I requested two additional data sets, observed with the IAC80 and NOT telescope. The IAC80 data set was used to confirm the data calibration performed bases on the standard stars by Stetson (2000a, 2005). However, the coefficients derived are compatible with the former ones. Consequently, I used the NOT data to investigate the possible presence of a non linearity in the Subaru data. However, these data resulted in not being not deep enough to solve this discrepancy. In any case, the data can be used to study the relative width of the SF burst in this galaxy. Thus, I compared the observed and the theoretical distributions of stars in the SGB. From this analysis I obtained that the burst of SF in this galaxy is between 0.15 and 2 Gyr long. This is compatible with the results previously found (e.g. Carrera et al. 2002; Ikuta & Arimoto 2002). In addition, I studied the radial gradients in UMi. All the evolutionary phases exhibit exponential profiles, whose scale lengths are compatible within the errors. Therefore UMi does not show any sign of radial gradients in its populations. To conclude I studied the nature of the stars bluer than the MS TO. These do not exhibit any particular trend, and are hence confirmed as BSS stars, in agreement with other authors (e.g. Mapelli et al. 2007; Carrera et al. 2002).

- **Her**. This UFD is observed in two fields using the Subaru telescope. I used these data to derive the distance to this galaxy, which results in $(\mathrm{m}-\mathrm{M})_0 = 20.8 \pm 0.2$. The photometry results too shallow to derive an accurate SFH, hence I compared it with GGCs and a set of isochrones from the BaSTI library (Pietrinferni et al. 2004). From this comparison, it is found out that this UFD is composed of a very old population, whose age is larger that 12 Gyr, and which shows a low metal content, $\langle[\mathrm{Fe/H}]\rangle = -2.3$. These results are compatible with previous studies (e.g. Brown et al. 2012; Fabrizio et al. 2014).

This thesis allows to carry out a comparison between the different morphological types of dwarf galaxies in the LG. The dIrr studied shows a very complex SFH, and traces still ongoing SF activity. In addition, it exhibits multiple stellar populations, at odds with the others. The dSphs and UFDs appear, at the same time, very similar and simple. They are mainly dominated by a unique old metal-poor stellar population.

Appendix A

Subaru fields internal calibration

Draco

In Section 6.1 the calibration of Draco is discussed. In this section I present the plots obtained to perform the calibration both between short and long exposures and between the fields, using the common regions, as shown in Fig. 2.9.

I calibrated every long to its short exposure. No colour term was found in any of the cases. An exception is field 1 short-long in *I* band. In this case a mild colour term was found. Figures A.1, A.2, A.3, A.4, A.5, A.6, show the calibration for the six fields respectively. In every figure the resulting coefficients are indicated.

On the other hand, I calibrated the short exposures of every field to that of field 1. There are two exceptions to this. To calibrate field 5 I used the long exposure, due to the poor overlapping between the short exposures of fields 1 and 5. The second exception is field F, which overlaps only with field 4 (Fig. 2.9). Therefore, once I calibrated field 4, using the standards in field 1, I used field 4 as standard to calibrate field F. Figures A.7, A.8, A.9, A.10, A.11 show the calibration plots. No colour term is found in any case, but only a zero-point. The values are indicated in the figures itself, with the associated errors.

This calibrations are fundamental in order to create one final catalogue. The number of resulting objects is indicated in Table 3.1. In the matching field F was excluded. In fact, this field is only used to evaluate the contribution of field stars to the CMD of Draco. The details are discussed in Chapter 6.

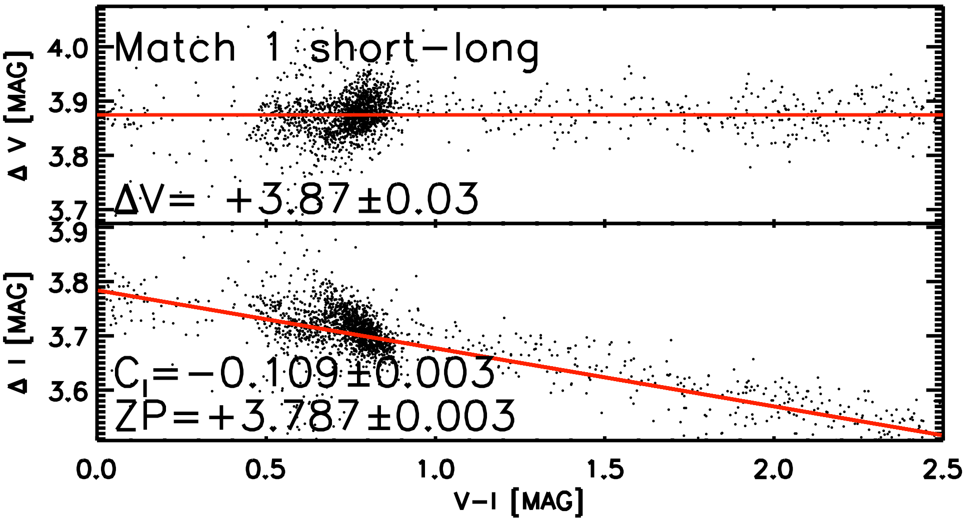

Figure A.1: Draco field 1 long-short calibration, for the V and I band (*top* and *bottom* panel, respectively). $\Delta M = M_{short} - m_{long}$, where m are the magnitudes in the two bands, V and I. A $3-\sigma$ clipping has been applied. The best fit to the data is shown in red. The resulting coefficient are indicated in the figure. No colour term is identified in the V calibration. Hence, only a zero point was found and it is indicated in the figure together with its uncertainty. In the case of the I band a mild colour term was found. In the figure the two coefficients C_I and ZP, of the linear equation $\Delta I = C_I\ (V-I) + ZP$, are indicated with the associated uncertainty.

UMi

The same process was repeated for UMi. Figures A.12 and A.13 show the short-long calibration of the two fields of this galaxy. As in the case of

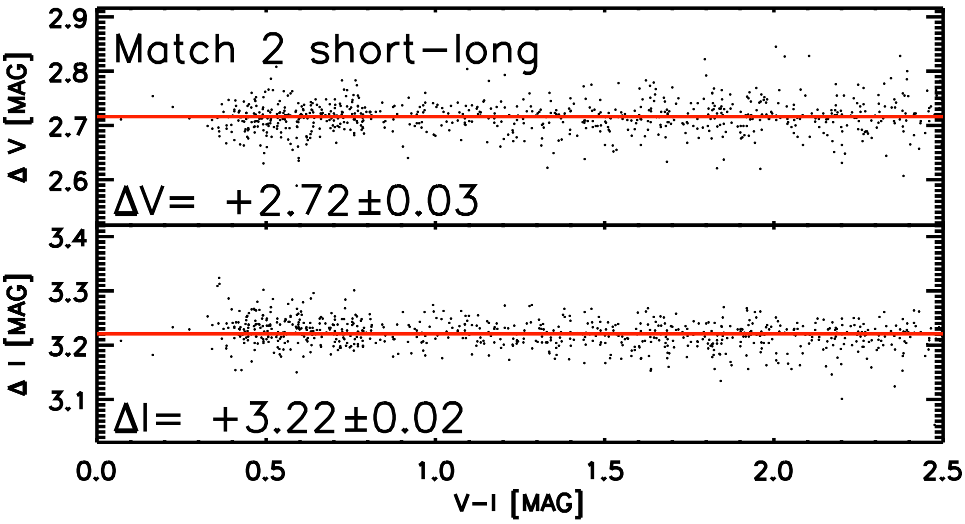

Figure A.2: Same as Fig. A.1, but in the case of field 2. For this field no colour term was found in any filter.

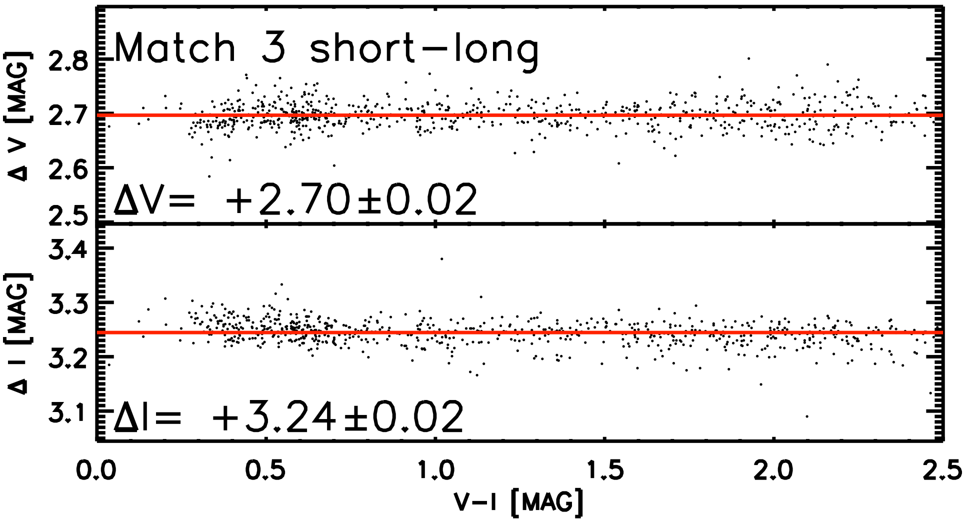

Figure A.3: Same as Fig. A.1, but in the case of field 3. For this field no colour term was found in any filter.

Draco, no colour term was found in any case, with the exception of the *I* calibration in field 1.

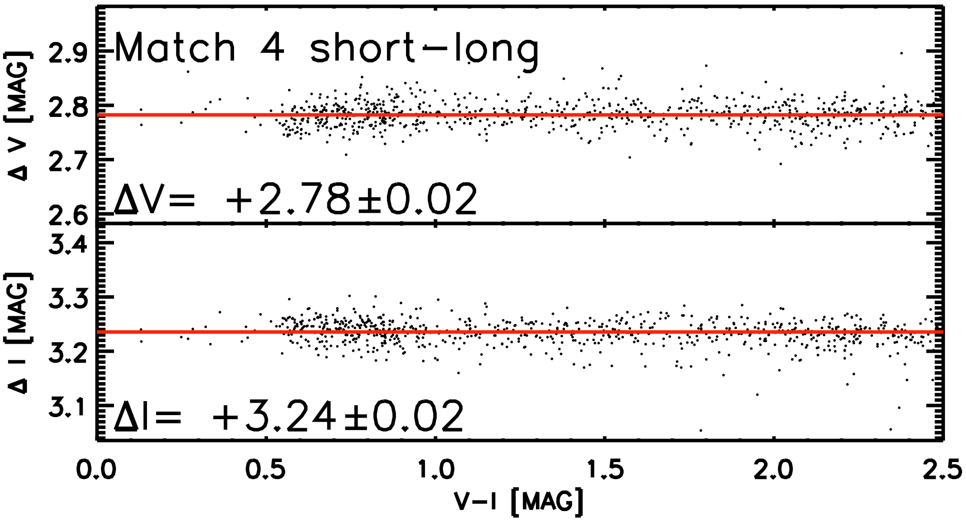

Figure A.4: Same as Fig. A.2, but in the case of fields 4 . For this field no colour term was found in any filter.

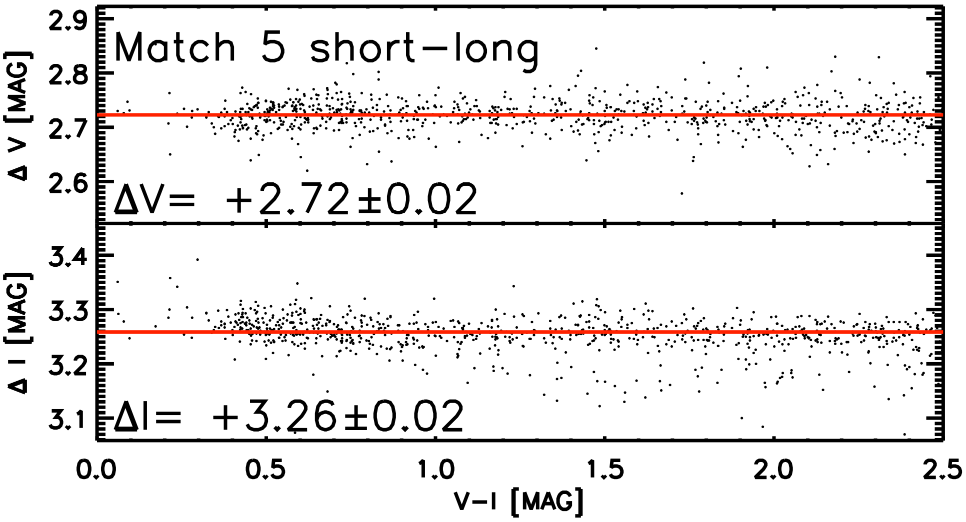

Figure A.5: Same as Fig. A.2, but in the case of fields 5.For this field no colour term was found in any filter.

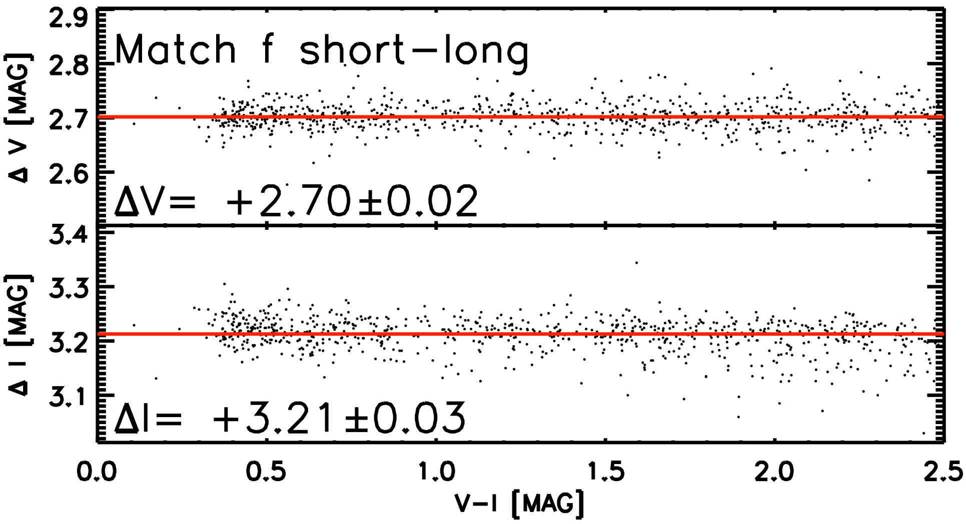

Figure A.6: Same as Fig. A.2, but in the case of fields F. In this case no color term was found in any case.

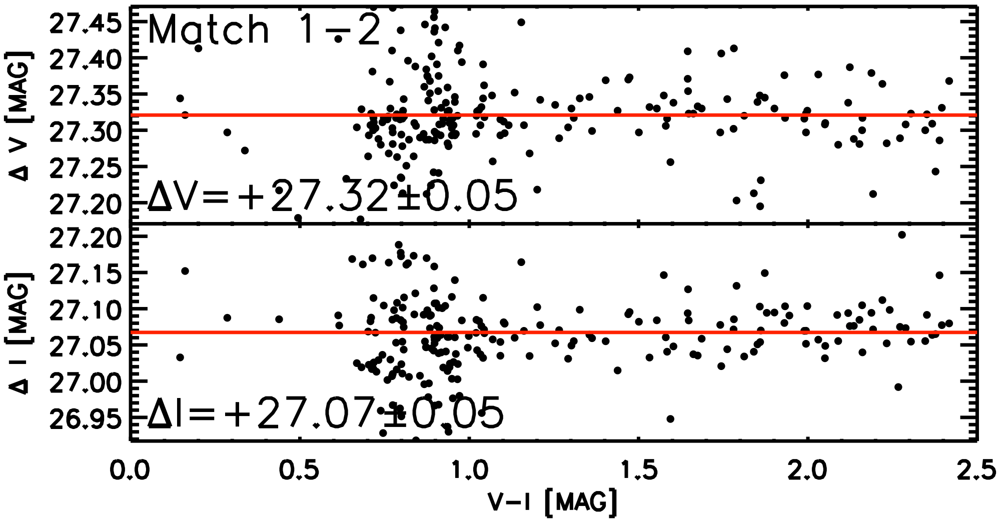

Figure A.7: Internal calibration between fields 1 and 2 of Draco, for the V and I band (*top* and *bottom* panel, respectively). $\Delta M = M_1 - m_2$, where m are the magnitudes in the two bands, V and I. The short exposures have been considered. The best fit of the data is shown in red. A $3-\sigma$ clipping has been applied. No colour term is identified. The resulting zero-point is indicated in the plots, with its error.

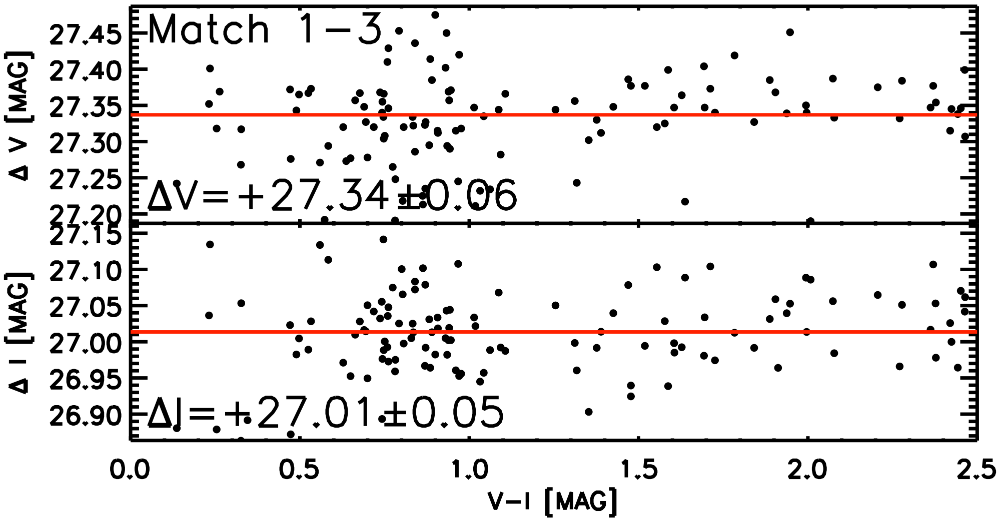

Figure A.8: Same as Fig. A.7, but in the case of fields 1 and 3.

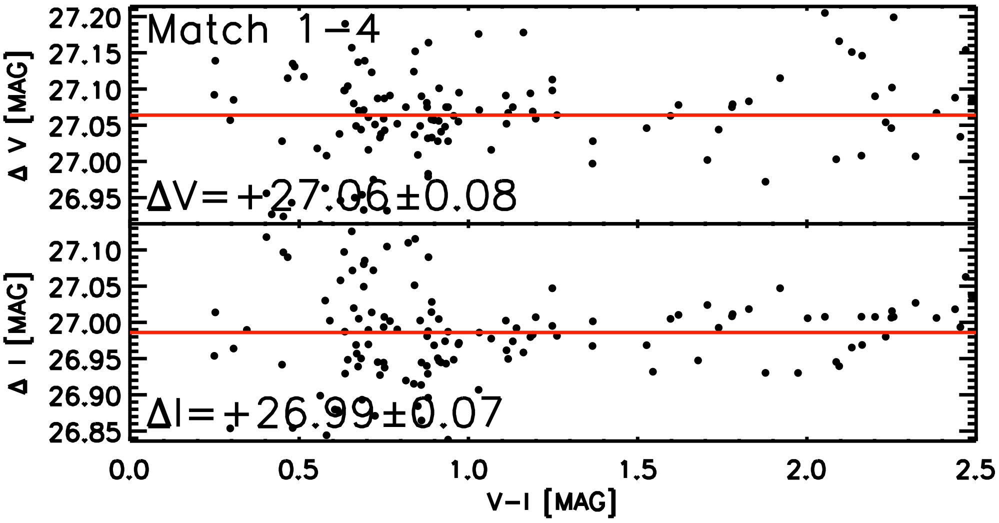

Figure A.9: Same as Fig. A.7, but in the case of fields 1 and 4.

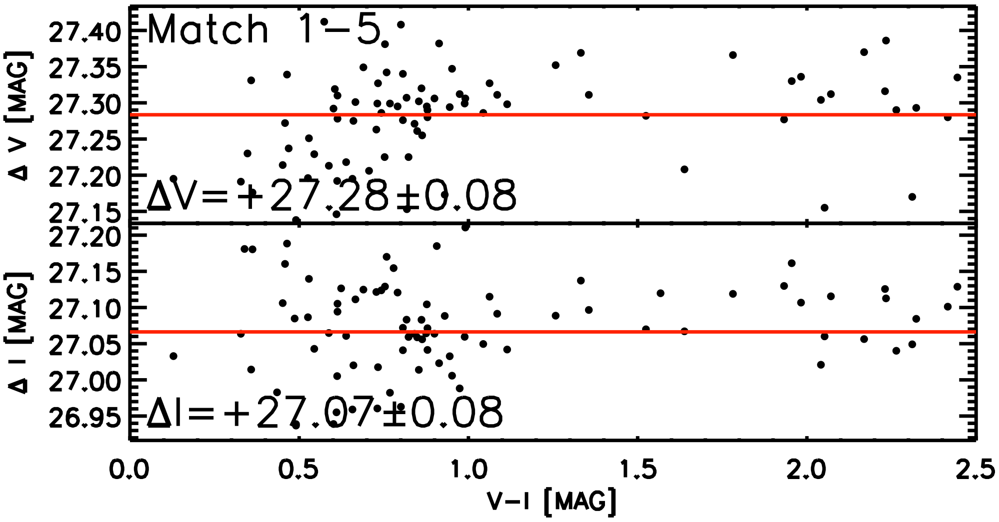

Figure A.10: Same as Fig. A.7, but in the case of fields 1 and 5. In this case the match was performed with the field 5 long exposure.

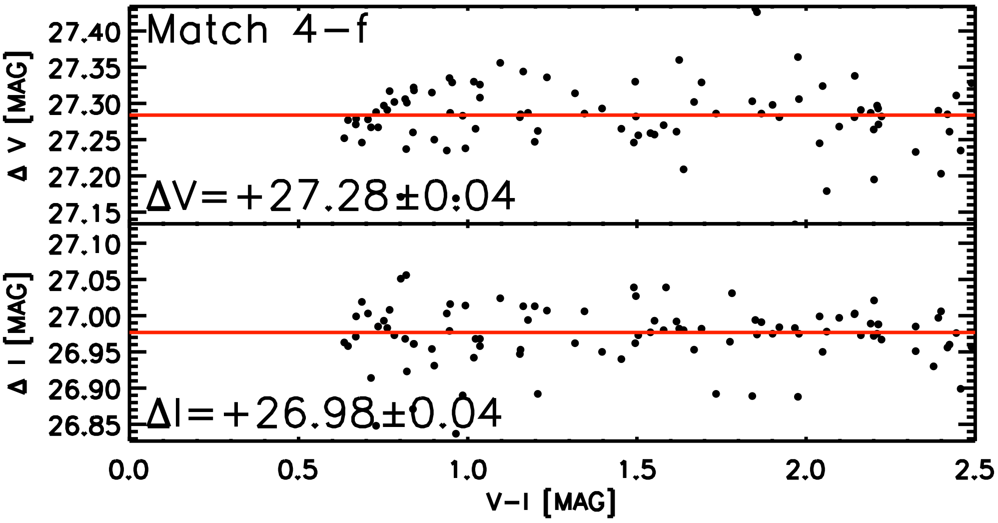

Figure A.11: Same as Fig. A.7, but in the case of fields 4 and F.

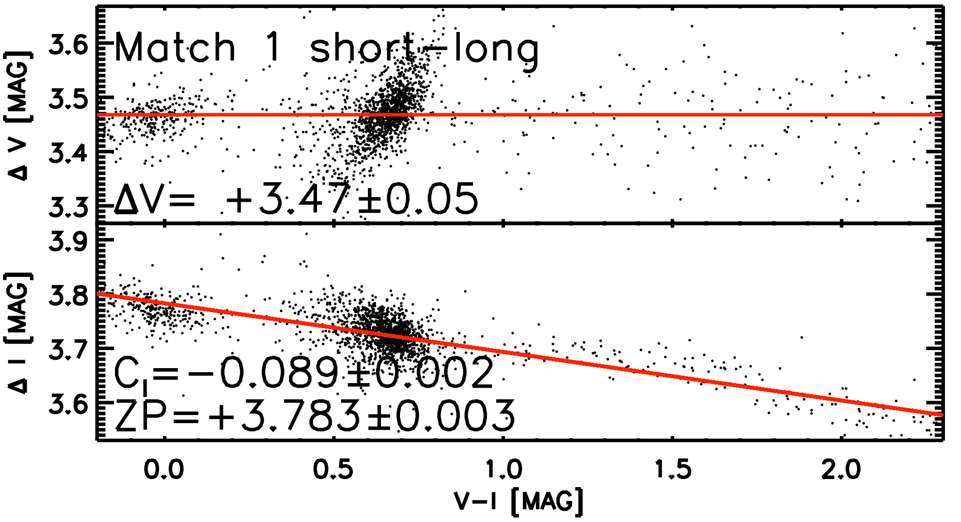

Figure A.12: UMi field 1 long-short calibration. Same as Draco Fig. A.1. Only in the case of the *I* band a mild colour term was found.

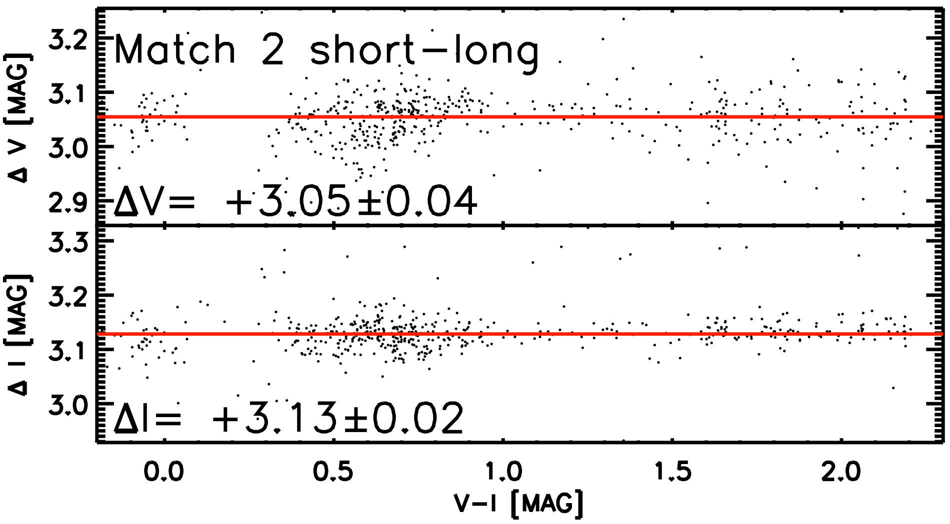

Figure A.13: UMi field 2 long-short calibration. Same as Draco Fig. A.1. Only in the case of the *I* band a mild colour term was found.

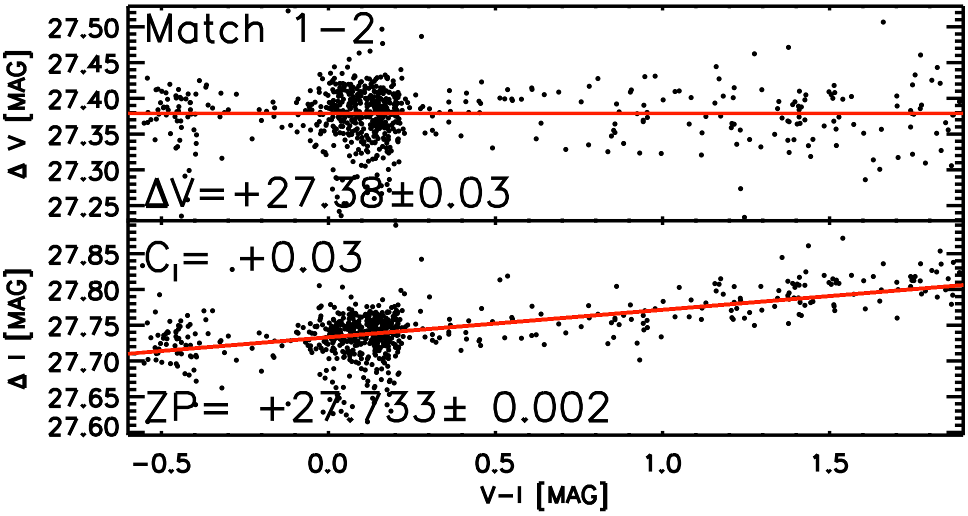

Figure A.14: Internal calibration between fields 1 and 2 of UMi, for the V and I band (*top* and *bottom* panel, respectively). $\Delta M = M_1 - m_2$, where m are the magnitudes in the two bands, V and I. The long exposures have been considered. The best fit of the data is shown in red. A $3-\sigma$ clipping has been applied. No colour term was found in the V band, whereas a small colour term is identified in the I band. The resulting coefficients are indicated in the plots, with the errors.

Her

The same process was repeated for Her. Figures A.15 and A.16 show the short-long calibration of the two fields of this galaxy. No colour term is found in any case. Figure A.16 shows the internal calibration between fields 1 and 2W. Only a zero point is found.

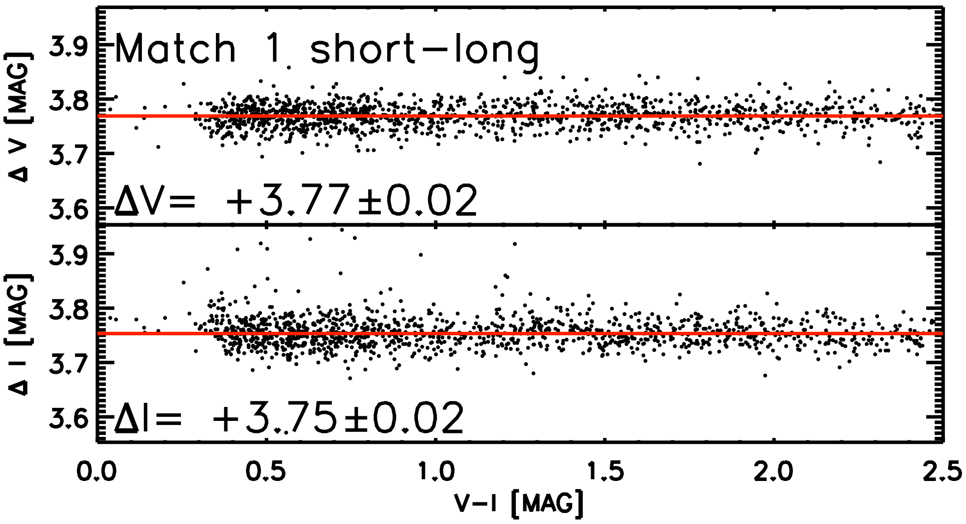

Figure A.15: Her field 1 long-short calibration. Same as Draco Fig. A.1.

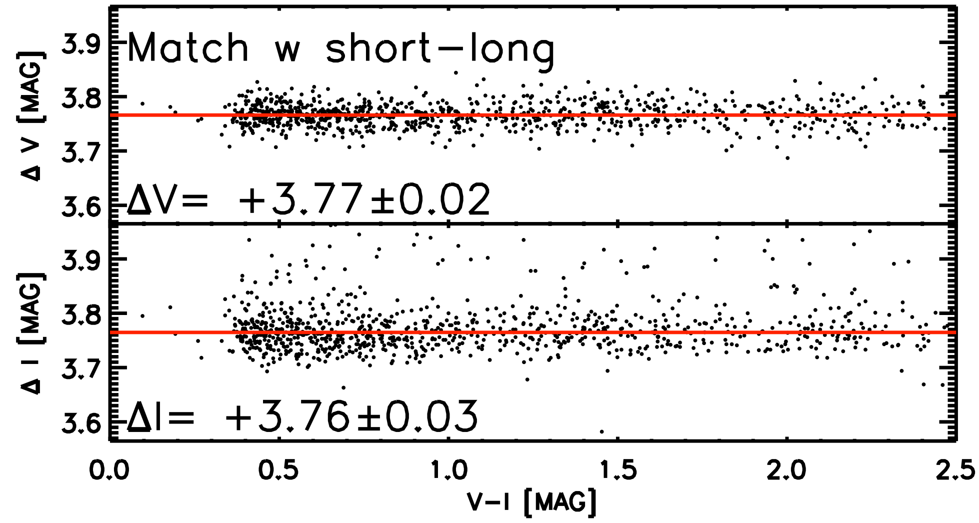

Figure A.16: Her field west long-short calibration. Same as Draco Fig. A.1.

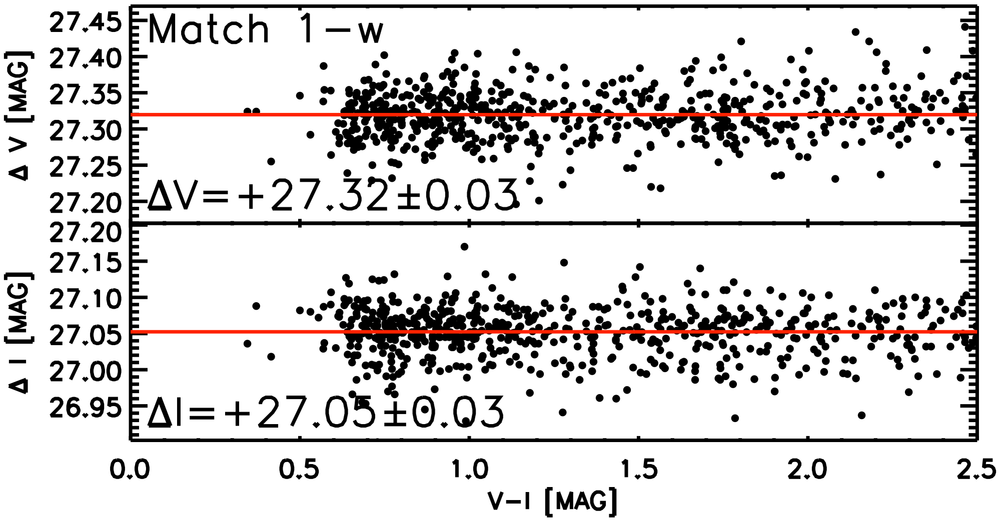

Figure A.17: Internal calibration between fields 1 and 2W of Her, for the V and I band (*top* and *bottom* panel, respectively). $\Delta M = M_1 - m_2$, where m are the magnitudes in the two bands, V and I. The long exposures have been considered. The best fit to the data is shown in red. A $3-\sigma$ clipping has been applied. No colour term was found in any case. The resulting coefficients are indicated in the plots, with the errors.

Appendix B

Subaru Standard Fields

Together with the galaxies, some standard fields were also observed with the Subaru telescope. To perform a good calibration, standard stars should span a wide range in colour and in airmass. In this way, it is possible to determine a reliable colour correction and extinction coefficients, respectively.

In the case of Subaru observations, for a number of reasons, I was not able to rely on the calibration obtained by the standard fields observed. First of all, the evaluation of the atmospheric extinction coefficient was impossible due to the poor air mass coverage. Thus, I adopted the values of the atmospheric extinction coefficient provided by the *Canada-France-Hawaii Telescope* (CFHT), which collects all the values since 2001[1]. Second, the same standard star was always observed with the same CCD of the Suprime-Cam. Thus, the flux scaling between the ten CCDs had to rely on the values obtained by the SDFRED pipeline. Third, the Δm, defined as the difference between the standard and the instrumental magnitude, was affected by a large dispersion. Hence, the high uncertainty on the coefficients did not allow to obtain a trustable calibration. This is shown in Fig. B.1, for one night as an example.

The calibrations of Draco, UMi, and Her are discussed in great detail in chapters 6, 7, and 8, respectively.

---

[1] The archive of the atmospheric attenuation is available at http://www.cfht.hawaii.edu/Instruments/Elixir/skyprobe/home.html. It collects atmospheric attenuation since early 2001.

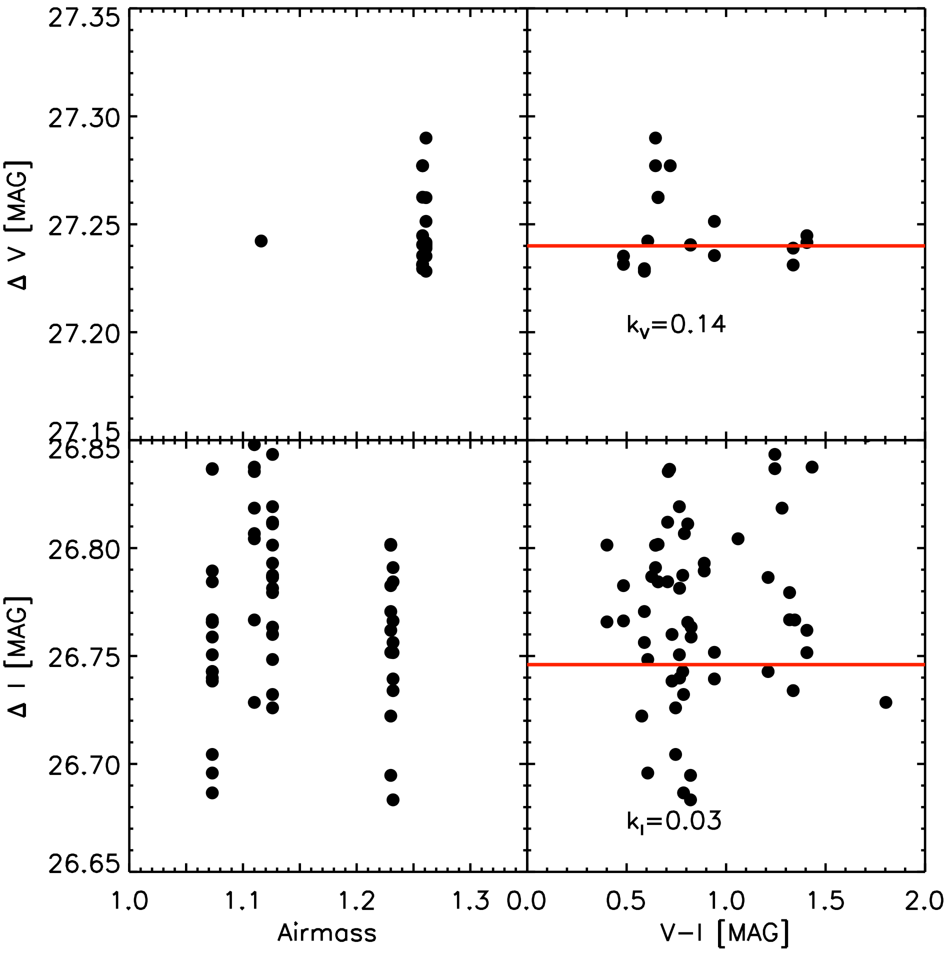

Figure B.1: Calibration attempt with the standard fields observed during the night of August 23rd, 2009. For all the other nights of observations I obtain similar results. *Left panel:* ΔV (*top panel*) and ΔI (*bottom panel*) are shown as a function of the air mass. *Right panel:* ΔV (*top panel*) and ΔI (*bottom panel*) are shown as a function of the standard colour $(V - I)$. The assumed extinction coefficients $k_{V,I}$ are indicated in the figure. These have been obtained using the CFHT archive of atmospheric attenuation. The red line indicates the mean value obtained. It is clear that these data do not allow to obtain neither an estimate of the atmospheric extinction coefficient nor that of the colour-term.

Appendix C

Publications

Refereed Publications

- **Fusco, F.**, Buonanno, R., Bono, G., Cassisi, S., Monelli, M., Pietrinferni, A. (2012) "Distance and reddening of the Local Group dwarf irregular galaxy NGC 6822", *A & A*, 548:A129
- **Fusco, F.**, Buonanno, R., Hidalgo, S. L., Aparicio, A., Pietrinferni, A., Bono, G., Monelli, M., Cassisi, S., (2014) "A state-of-the-art analysis of the dwarf irregular galaxy NGC 6822" , *A & A*, 572, A26

Non-Refereed Publications

- **Fusco, F.**, Buonanno, R., Bono, G., Cassisi, S., Monelli, M., Pietrinferni, A., Hidalgo, S. L., Aparicio, A. (2015) "The Local Group Dwarf Irregular Galaxy NGC 6822: new insight on its star formation history", *MmSAI*, 86:336-337

Acknowledgements

First of all, I would like to thank my supervisors Prof. Roberto Buonanno and Prof. Antonio Aparicio for helping me everyday in the development of this thesis. I also would like to thank all the people who helped me in completing this work Santino, Giuseppe, Matteo, and Adriano.

Pues... un agradecimiento especial va a Sebastian. Desde el primer dia que llegué a Tenerife nunca me ha dejado sola. Ha sido una de las personas que más ha luchado conmigo en estos años, me ha suportado y me ha ayudado con todas sus fuerzas para que esta tesis tuviera un sentido.

Otro agradecimiento va a TODOS los del IAC! Aqui conocí personas que espero me acompañen toda mi vida, que me han enseñado un nuevo idioma, que me han hecho descubrir esta isla magnifica, donde mi corazon se quedará siempre. Masca, el dia que necesitaré una peli cutre sabré a quien preguntar. Artemi, si te sobran pimientos y cebollas llamame! Riccardo, Спасиба por no comernos a todos. Sebas, recuerdate que yo soy la vaca, no el pollo. Clara, que buen español me enseñaste.

Irene, il tempo a Tenerife senza di te sarebbe stato molto più grigio e buio, per fortuna ora so che c'è una persona magnifica che ti sta accanto e me ne posso andare più tranquilla. Claudio, grazie per aver risolto il problema dei *missing satellites* e per preoccuparti di Irene!

Grazie a Sandra e Alessandro, compagni di dottorato e di vita, impagabilmente impagabili. Con voi qualunque discorso ha un senso, tutto prende vita e si muove.

Elisa, che dire... Un grazie non so se basterebbe, lasciamo che sia *tastefully offensive* a parlare per noi. E Carla, guardarti mi ha dato la forza di andare avanti in questi anni; il tuo essere povera mi ha sempre ricordato di come la mia vita non puó esser cosí male.

Grazie alle amiche che mi hanno accompagnato negli anni universitari, Rosi, Crist, e Giada, e alle persone che ho trovato lungo il mio cammmino, Michelino, Katia e Laura.

Un grazie particolare va anche ai miei genitori e Ale, che mi hanno sempre supportato in questi lunghi anni universitari.

Und... Danke Benny, mein gelber Prinz, dass es dich gibt. Du hast mir gezeigt, wie schön das Leben ist und dass die Welt fuer uns zusammen nicht gross genug ist. *I want to be your fool forever.*

References

Adén, D., Eriksson, K., Feltzing, S., et al. 2011, A&A, 525, A153

Adén, D., Wilkinson, M. I., Read, J. I., et al. 2009, ApJ, 706, L150

Aparicio, A., Carrera, R., & Martínez-Delgado, D. 2001, AJ, 122, 2524

Aparicio, A. & Gallart, C. 1995, AJ, 110, 2105

Aparicio, A. & Gallart, C. 2004, AJ, 128, 1465

Aparicio, A. & Hidalgo, S. L. 2009, AJ, 138, 558

Armandroff, T. E., Olszewski, E. W., & Pryor, C. 1995, AJ, 110, 2131

Baldacci, L., Rizzi, L., Clementini, G., et al. 2003, in Astronomical Society of the Pacific Conference Series, Vol. 296, New Horizons in Globular Cluster Astronomy, ed. G. Piotto, G. Meylan, S. G. Djorgovski, & M. Riello, 355

Barnard, E. E. 1884, Astronomische Nachrichten, 110, 125

Bellazzini, M., Ferraro, F. R., Origlia, L., et al. 2002, AJ, 124, 3222

Belokurov, V., Zucker, D. B., Evans, N. W., et al. 2007, ApJ, 654, 897

Bessell, M. S. 1990, PASP, 102, 1181

Binggeli, B. 1994, Panchromatic View of Galaxies - Their Evolutionary Puzzle, editions frontieres edn., ed. G. Hensler & C. Theis (Gif-sur-Yvette: Editions Frontieres)

Bonanos, A. Z., Stanek, K. Z., Szentgyorgyi, A. H., Sasselov, D. D., & Bakos, G. Á. 2004, AJ, 127, 861

Bovill, M. S. & Ricotti, M. 2011, ApJ, 741, 17

Brocato, E., Castellani, V., & Piersimoni, A. 1997, ApJ, 491, 789

Brown, T. M., Tumlinson, J., Geha, M., et al. 2012, ApJ, 753, L21

Cannon, J. M., O'Leary, E. M., Weisz, D. R., et al. 2012, ApJ, 747, 122

Carrera, R., Aparicio, A., Martínez-Delgado, D., & Alonso-García, J. 2002, AJ, 123, 3199

Cassisi, S. & Salaris, M. 2013, Old Stellar Populations: How to Study the Fossil Record of Galaxy Formation, Physics textbook (Wiley)

Castelli, F. & Kurucz, R. L. 2003, in IAU Symposium, Vol. 210, Modelling of Stellar Atmospheres, ed. N. Piskunov, W. W. Weiss, & D. F. Gray, 20P

Cioni, M.-R. L. & Habing, H. J. 2005, A&A, 429, 837

Clementini, G., Held, E. V., Baldacci, L., & Rizzi, L. 2003, ApJ, 588, L85

Coleman, M. G., de Jong, J. T. A., Martin, N. F., et al. 2007, ApJ, 668, L43

Cousins, A. W. J. 1978, Monthly Notes of the Astronomical Society of South Africa, 37, 8

Da Costa, G. S. 1998, in Stellar astrophysics for the local group: VIII Canary Islands Winter School of Astrophysics, ed. A. Aparicio, A. Herrero, & F. Sánchez, 351

de Blok, W. J. G. & Walter, F. 2000, ApJ, 537, L95

de Blok, W. J. G. & Walter, F. 2003, MNRAS, 341, L39

de Blok, W. J. G. & Walter, F. 2006, AJ, 131, 363

del Pino, A., Hidalgo, S. L., Aparicio, A., et al. 2013, MNRAS, 433, 1505

Dolphin, A. E. 2002, MNRAS, 332, 91

Donato, F., Gentile, G., Salucci, P., et al. 2009, MNRAS, 397, 1169

Faber, S. M. & Lin, D. N. C. 1983, ApJ, 266, L17

Fabrizio, M., Raimondo, G., Brocato, E., et al. 2014, A&A, 570, A61

Fattahi, A., Navarro, J. F., Starkenburg, E., Barber, C. R., & McConnachie, A. W. 2013, MNRAS, 431, L73

Feast, M. W., Whitelock, P. A., Menzies, J. W., & Matsunaga, N. 2012, MNRAS, 421, 2998

Forbes, D. A. & Bridges, T. 2010, MNRAS, 404, 1203

Fusco, F., Buonanno, R., Bono, G., et al. 2012, A&A, 548, A129

Gallagher, J. S., Madsen, G. J., Reynolds, R. J., Grebel, E. K., & Smecker-Hane, T. A. 2003, ApJ, 588, 326

Gallart, C., Aparicio, A., Bertelli, G., & Chiosi, C. 1996a, AJ, 112, 2596

Gallart, C., Aparicio, A., Bertelli, G., & Chiosi, C. 1996b, AJ, 112, 1950

Gallart, C., Aparicio, A., & Vilchez, J. M. 1996c, AJ, 112, 1928

Gieren, W., Pietrzyński, G., Nalewajko, K., et al. 2006, ApJ, 647, 1056

Girardi, L., Barbieri, M., Groenewegen, M. A. T., et al. 2012, TRILEGAL, a TRIdimensional modeL of thE GALaxy: Status and Future, ed. A. Miglio, J. Montalbán, & A. Noels, 165

Girardi, L., Bressan, A., Bertelli, G., & Chiosi, C. 2000, A&AS, 141, 371

Gnedin, N. Y. 2010, ApJ, 721, L79

Gnedin, O. Y. & Ostriker, J. P. 1997, ApJ, 474, 223

Gould, A. & Popowski, P. 1998, ApJ, 508, 844

Governato, F., Zolotov, A., Pontzen, A., et al. 2012, MNRAS, 422, 1231

Grebel, E. K. & Gallagher, III, J. S. 2004, ApJ, 610, L89

Grebel, E. K., Gallagher, III, J. S., & Harbeck, D. 2003, AJ, 125, 1926

Harris, W. E. 1996, AJ, 112, 1487

Hernández-Martínez, L., Peña, M., Carigi, L., & García-Rojas, J. 2009, A&A, 505, 1027

Hidalgo, S. L., Aparicio, A., Martínez-Delgado, D., & Gallart, C. 2009, ApJ, 705, 704

Hidalgo, S. L., Aparicio, A., Skillman, E., et al. 2011, ApJ, 730, 14

Hidalgo, S. L., Monelli, M., Aparicio, A., et al. 2013, ApJ, 778, 103

Holtzman, J. A., Afonso, C., & Dolphin, A. 2006, ApJS, 166, 534

Hubble, E. P. 1936, Realm of the Nebulae (Yale University Press)

Hutchings, J. B., Cavanagh, B., & Bianchi, L. 1999, PASP, 111, 559

Ikuta, C. & Arimoto, N. 2002, A&A, 391, 55

Irwin, M. & Hatzidimitriou, D. 1995, MNRAS, 277, 1354

Johnson, H. L. & Morgan, W. W. 1953, ApJ, 117, 313

Kacharov, N., Rejkuba, M., & Cioni, M.-R. L. 2012, A&A, 537, A108

Kirby, E. N., Cohen, J. G., Guhathakurta, P., et al. 2013a, ApJ, 779, 102

Kirby, E. N., Cohen, J. G., Guhathakurta, P., et al. 2013b, ApJ, 779, 102

Kleyna, J. T., Geller, M. J., Kenyon, S. J., Kurtz, M. J., & Thorstensen, J. R. 1998, AJ, 115, 2359

Kleyna, J. T., Wilkinson, M. I., Evans, N. W., & Gilmore, G. 2001, ApJ, 563, L115

Komiyama, Y., Okamura, S., Yagi, M., et al. 2003, ApJ, 590, L17

Koposov, S. E., Belokurov, V., Torrealba, G., & Wyn Evans, N. 2015, ArXiv e-prints

Kroupa, P. 2001, MNRAS, 322, 231

Landolt, A. U. 1992, AJ, 104, 340

Landolt, A. U. 2009, AJ, 137, 4186

Lee, M. G., Freedman, W. L., & Madore, B. F. 1993, ApJ, 417, 553

Letarte, B., Demers, S., Battinelli, P., & Kunkel, W. E. 2002, AJ, 123, 832

MacLachlan, J. M., Bonnell, I. A., Wood, K., & Dale, J. E. 2015, A&A, 573, A112

Mapelli, M., Ripamonti, E., Tolstoy, E., et al. 2007, MNRAS, 380, 1127

Mapelli, M., Sigurdsson, S., Ferraro, F. R., et al. 2006, MNRAS, 373, 361

Martin, N. F., de Jong, J. T. A., & Rix, H.-W. 2008, ApJ, 684, 1075

Martínez-Delgado, D., Alonso-García, J., Aparicio, A., & Gómez-Flechoso, M. A. 2001, ApJ, 549, L63

Massey, P., Armandroff, T. E., Pyke, R., Patel, K., & Wilson, C. D. 1995, AJ, 110, 2715

Mateo, M. L. 1998, ARA&A, 36, 435

McConnachie, A. W. 2012, AJ, 144, 4

McLean, I. S. 2008, Electronic Imaging in Astronomy - Detectors and Instrumentation, second edition edn., ed. P. Blondel & J. Mason (Chichester, UK: Springer-Praxis Publishing)

Mighell, K. J. & Burke, C. J. 1999, AJ, 118, 366

Miyazaki, S., Komiyama, Y., Sekiguchi, M., et al. 2002, PASJ, 54, 833

Moore, B., Ghigna, S., Governato, F., et al. 1999, ApJ, 524, L19

Musella, I., Ripepi, V., Marconi, M., et al. 2012, ApJ, 756, 121

Odenkirchen, M., Grebel, E. K., Harbeck, D., et al. 2001, AJ, 122, 2538

Orban, C., Gnedin, O. Y., Weisz, D. R., et al. 2008, ApJ, 686, 1030

Origlia, L. & Leitherer, C. 2000, AJ, 119, 2018

Pagel, B. 2009, Nucleosynthesis and Chemical Evolution of Galaxies (Cambridge University Press)

Pagel, B. E. J., Edmunds, M. G., & Smith, G. 1980, MNRAS, 193, 219

Peimbert, A., Peimbert, M., & Ruiz, M. T. 2005, ApJ, 634, 1056

Pietrinferni, A., Cassisi, S., Salaris, M., & Castelli, F. 2004, ApJ, 612, 168

Pietrinferni, A., Cassisi, S., Salaris, M., & Castelli, F. 2006, ApJ, 642, 797

Prieto, M., Joven, E., & Oscoz, A. 2004, CAMELOT: Detector Characterization, Instituto de Astrofísica de Canarias

Rich, J. A., Persson, S. E., Freedman, W. L., et al. 2014, ApJ, 794, 107

Riess, A. & Mack, J. 2004, Time Dependence of ACS WFC CTE Corrections for Photometry and Future Predictions, Tech. rep.

Robin, A. C., Reylé, C., Derrière, S., & Picaud, S. 2003, A&A, 409, 523

Roderick, T. A., Jerjen, H., Mackey, A. D., & Da Costa, G. S. 2015, ApJ, 804, 134

Salaris, M. & Cassisi, S. 2005, Evolution of Stars and Stellar Populations (Wiley)

Sand, D. J., Olszewski, E. W., Willman, B., et al. 2009, ApJ, 704, 898

Santana, F. A., Muñoz, R. R., Geha, M., et al. 2013, ApJ, 774, 106

Sawala, T., Frenk, C. S., Fattahi, A., et al. 2014, ArXiv e-prints

Schlafly, E. F. & Finkbeiner, D. P. 2011, ApJ, 737, 103

Schlegel, D. J., Finkbeiner, D. P., & Davis, M. 1998, ApJ, 500, 525

Schroyen, J., De Rijcke, S., Koleva, M., Cloet-Osselaer, A., & Vandenbroucke, B. 2013, MNRAS, 434, 888

Searle, L. & Zinn, R. 1978, ApJ, 225, 357

Shetrone, M. D., Côté, P., & Sargent, W. L. W. 2001, ApJ, 548, 592

Sibbons, L. F., Ryan, S. G., Cioni, M.-R. L., Irwin, M., & Napiwotzki, R. 2012, A&A, 540, A135

Simon, J. D. & Geha, M. 2007, ApJ, 670, 313

Sirianni, M., Jee, M. J., Benítez, N., et al. 2005, PASP, 117, 1049

Skillman, E. D. & Bender, R. 1995, in Revista Mexicana de Astronomia y Astrofisica Conference Series, Vol. 3, Revista Mexicana de Astronomia y Astrofisica Conference Series, ed. M. Pena & S. Kurtz, 25

Skillman, E. D., Terlevich, R., & Melnick, J. 1989, MNRAS, 240, 563

Stetson, P. B. 1987, PASP, 99, 191

Stetson, P. B. 1994, PASP, 106, 250

Stetson, P. B. 2000a, PASP, 112, 925

Stetson, P. B. 2000b, User's Manual for DAOPHOT II, Dominion Astrophysical Observatory

Stetson, P. B. 2005, PASP, 117, 563

Stetson, P. B. & Harris, W. E. 1988, AJ, 96, 909

Tammann, G. A. 1994, Dwarf Galaxies, ed. G. Meylan & P. Prugniel, Vol. 49 (European Southern Observatory Astrophysics Symposia)

Tolstoy, E. 2010, in IAU Symposium, Vol. 262, IAU Symposium, ed. G. R. Bruzual & S. Charlot, 119–126

Tolstoy, E., Hill, V., & Tosi, M. 2009, ARA&A, 47, 371

Tolstoy, E., Irwin, M. J., Cole, A. A., et al. 2001, MNRAS, 327, 918

Ubeda, L., Aloisi, A., Bostroem, A., et al. 2011, Hubble Space Telescope Primer for Cycle 20, Baltimore: STScI

Ubeda, L. & et al. 2011, "ACS Instrument Handbook", Version 11.0, Baltimore: STScI

van den Bergh, S. 1998, Galaxy Morphology and Classification

VandenBerg, D. A., Swenson, F. J., Rogers, F. J., Iglesias, C. A., & Alexander, D. R. 2000, ApJ, 532, 430

Vargas, L. C., Geha, M., Kirby, E. N., & Simon, J. D. 2013, ApJ, 767, 134

Venn, K. A., Lennon, D. J., Kaufer, A., et al. 2001, ApJ, 547, 765

Weisz, D. R., Dolphin, A. E., Skillman, E. D., et al. 2014, ApJ, 789, 147

Wright, E. L. 2006, PASP, 118, 1711

Wyder, T. K. 2001, AJ, 122, 2490

Yin, J., Matteucci, F., & Vladilo, G. 2011, A&A, 531, A136

Young, L. M. 2000, AJ, 119, 188

Zurita, C. 2011, CAMELOT: IAC80 TELESCOPE CCD - User Manual, Instituto de Astrofísica de Canarias